University of Naples Federico II

Department of Industrial Engineering

Ph.D. Dissertation

Doctoral Program in Industrial Engineering

XXXVI Cycle

Ph.D. Coordinator: Prof. Eng. Michele Grassi

MANAGEMENT STRATEGIES FOR AIRCRAFT HYBRID PROPULSION SYSTEM AND EXPERIMENTAL ASSESMENT

Ph.D. Candidate

Commissario Capo della Polizia di Stato

Dr. Enrico Fornaro

(DR995313)

Supervisor

Prof. Eng. Massimo Cardone
(University of Naples "Federico II")

Reviewers

Prof. Eng. Andrea Unich
(University of Campania "Luigi Vanvitelli")

Prof. Eng. Emiliano Pipitone
(University of Palermo)

“Il Cielo stellato sopra di me,

e la legge morale dentro di me”

I. Kant

(Critica della Ragion Pratica)

“Ai miei Genitori”

Acknowledgments

In queste righe vorrei ringraziare chi direttamente e indirettamente ha contribuito affinché potessi giungere al traguardo di questo percorso di Dottorato, arricchito di ulteriori conoscenze tecnico-scientifiche e soprattutto personali.

Mi è doveroso ringraziare il Ministero dell'Interno – Dipartimento della Pubblica Sicurezza che mi ha dato la possibilità di potenziare le mie conoscenze, certamente utili al settore Motorizzazione della Polizia di Stato in vista dell'attuale rivoluzione tecnologica nel settore dei trasporti, che vede sempre più presente la propulsione elettrica accoppiata, o in alcuni casi addirittura sostituire, il tradizionale motore termico.

Desidero esprimere la mia sincera gratitudine al mio supervisore, il Prof. Ing. Massimo Cardone, per la sua costante disponibilità e presenza durante il mio percorso di Dottorato. Ma soprattutto, desidero ringraziarlo per i quotidiani scambi di opinione che innescavano sempre proficue riflessioni.

Ringrazio il Prof. Ing. Marcello Manna per la sua preziosa influenza e sono grato per il tempo e l'attenzione che ha dedicato a me. Le sue parole e il suo contributo hanno avuto un impatto positivo sulla mia crescita accademica.

Ringrazio il Prof. Ing. Mariano Migliaccio per i suoi preziosi incontri e alla sua condivisione della teoria di progettazione degli ingranaggi ad alto scorrimento (HSG). Spero di poter onorare la sua eredità e contribuire positivamente a questo campo in futuro. La sua guida è stata un privilegio e un'ispirazione nella mia carriera accademica e professionale.

Ringrazio inoltre tutti i colleghi Ricercatori e Dottorandi del Dipartimento di Ingegneria Industriale, in particolar modo Ciro Tordela, per aver condiviso un pezzo di carriera e di vita insieme.

Enrico Fornaro

Contents

List of Figures

List of Tables

Nomenclature

AC	Alternate Current
BSFC	Brake Specific Fuel Consumption
BSG	Belt-driven Starter Generator
CAN	Controller Area Network
DAB	Dual Active Bridge
DAS	Data acquisition System
DC	Direct Current
DIO	digital input/output
DIPROVEL	DImostratore tecnologico di un sistema di PROpulsione ibrida aeronautico per applicazioni su VEivoli Leggeri
DoH	Degree-of-Hybridization
EASA	European Aviation Safety Agency
ECU	Electronic Control Unit
EM	Elelectric Machines
EMF	ElectroMotive Force
ESS	Energy Storage System
EV	Electric Vehicles
FC	Fuell Cell
FEV	Full Electric Vehicles
FPGA	Field Programmable Gate Array
GHG	GreenHouse Gas
GUI	Graphic User Interface
HEPS	Hybrid Electric Propulsion System
HEV	Hybrid Electric Vehicles
HHV	Higher Heating Value
ICAO	International Civil Aviation Organization
ICE	Internal Combustion Engine
IM	Induction Machines
ISG	Integrated Starter Generator
LHV	Lower Heating Value

Li-Air	Lithium-Air battery
Li-ion	Lithium-Ion battery
Li-S	Lithium-Sulfur battery
MOF	Metal Organic Frameworks
NI	National Instruments
Ni-Cd	nickel-cadmium
Ni-MH	nickel-metal-hydride
OCV	Open Circuit Voltage
ONU	United Nations Organization
OS	Operative System
OVC	Off-Vehicle Charging
PEMFC	Proton Exchange Membrane Fuel Cells
PHEV	Plug-in Hybrid Electric Vehicles
PMSM	Permanent Magnet Synchronous Machines
PWM	Pulse Width Modulation
RESS	Rechargeable Energy Storage System
RT	Real-Time
SAF	Sustainable Aviation Fuels
SOA	State of Art
SoC	State of Charge
SoE	State of Energy
SOFC	Solid Oxide Fuel Cells
SRM	Switched Reluctance Machine
SynRM	Synchronous Reluctance Machine
TRU	Transformer Rectifier Units
VRM	Variable Reluctance Machine
VSI	Voltage-Source Inverter

Abstract

The significant reduction of CO_2 and NO_x emissions, as well as aircraft noise, is becoming an increasingly urgent target for many aeronautical agencies to be achieved by 2050. Therefore, many changes will be needed in the aviation propulsion industry in the coming years. In this context, hybrid-electric propulsion systems (HEPS) could be a good compromise for reducing emissions and noise while having a lighter propulsive architecture than a fully electric system. In the present work, an experimental investigation has been carried out on a hybrid-electric propulsion system (HEPS) for aircraft application. The experimental data has been used to validate the HEPS model designed in Matlab/Simulink consisting of a point-mass aircraft dynamical model coupled with a map-based approach for the simulation of the powertrain components, i.e., propeller, internal combustion engine, electric machine, and battery.

The simulated results showed good matching to the experimental ones. Moreover, the proposed model demonstrates its capability and flexibility to predict the global HEPS dynamical behavior and performance. Moreover, an adaptive supervisor controller is integrated into the model to minimize the equivalent fuel consumption during the flight mission.

The proposed method has been applied to an eight-sit civil utility aircraft employed for repetitive short-range missions typical of air taxi applications. The analysis shows that thanks to the proper selection of the Degree of Hybridization and the optimal control strategy, a 6% CO_2 reduction is achieved compared to the conventional "Fully-Thermal" configuration. Moreover, the reduction reaches a significant amount of 31% when a plug-in architecture is adopted. Moreover, in this work, the adaptive supervisor, developed in Matlab/Simulink, is tested in real-time in the engine test laboratory on the real HEPS, evaluating the control capability and the real-time management of the engines. For this purpose, a short-duration mission has been chosen to represent the typical aviation maneuvers generally performed by a pilot (i.e., Take-off, climb, cruise, and landing).

Chapter 1

1. INTRODUCTION

Human emissions of carbon dioxide and other greenhouse gases are a primary driver of climate change and present one of the world's most pressing challenges [1]. This link between global temperatures and greenhouse gas (GHG) concentrations (in particular CO_2) has been true throughout Earth's history [2]. To slow down – with the eventual aim of halting – rising global temperatures, the world needs to reach net-zero emissions to stabilize and reduce the concentrations of CO_2 and other greenhouse gases in Earth's atmosphere. At a time when global emissions need to be falling, they are still rising, as Figure 1.1 shows.

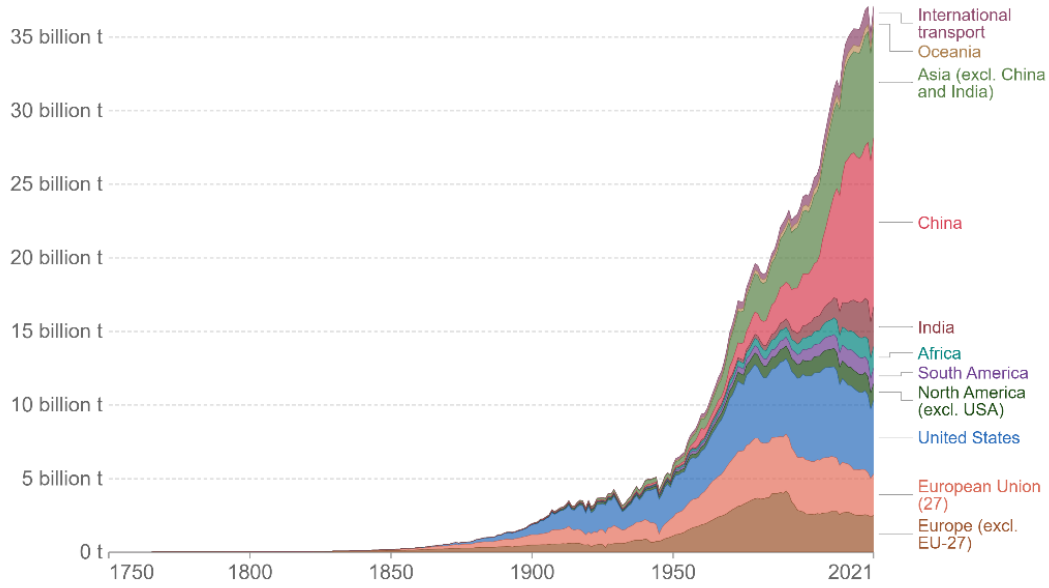

Figure 1.1. Annual CO_2 emissions by world region (this measures fossil fuel and industry emissions) [3].

To effectively reduce emissions it's important to know where they are coming, which sectors contribute the most. In Figure 1.2 are highlighted the main GHG emission sector, from this diagram is that the 73% of emissions come from energy use; 18,4% form agriculture and land use, and the remaining 8% from industry and waste.

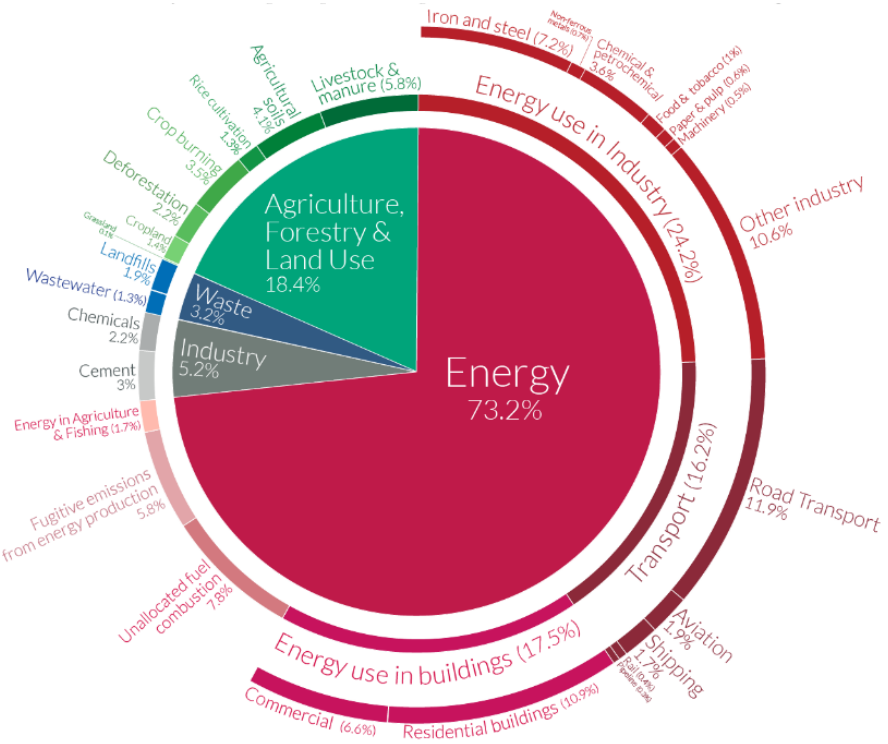

Figure 1.2. Global greenhouse gas emissions by sector (this is shown for the year 2016 – global GHG 50 billion tonnes CO_2,eq) [4].

Regarding the Paris Agreement (COP21) held at the 2015 United Nations Organization (ONU) during the Climate Change Conference, 195 countries, including Italy and numerous international organizations, committed to keeping temperature rise below 2°C above pre-industrial levels by 2050. The agreement provides financial support for climate change mitigation and actions that can facilitate a low-carbon transition in all sectors [5].

1.1. Motivation

The transport field, specifically the aviation sector, which currently impacts about 2 percent of global CO_2 emissions, it is the task of the International Civil Aviation Organization (ICAO) to implement the guidelines of the COP21 agreement and implement a series of measures to reduce the environmental impact of aircraft, concentrated in three main areas: climate change and aviation emissions, aircraft noise and local air quality.

These issues are being realized mainly through airframe innovation, the adoption of optimized air lanes, using more direct flight paths, the use of more precise satellite navigation, the adoption of more efficient engines that reduce CO_2 and NO_x emissions and noise, the introduction of optimized landing and take-off procedures, use of biofuels, and implementation of the carbon

offset system (CORSIA project) that is based on the purchase of emission credits from emission reduction projects in another sector [6].

Ambitious goals, unveiled by NASA [7] with its N+3 goals or the European Commission with the Strategic Research Innovation Agenda (SRIA) – Flightpath 2050 [8] challenges and goals, are confronting the aviation community with new challenges in aircraft design and operation due to new technologies implementation (Table 1.1). Those goals target significant power efficiency, emission, and noise reductions for future aircraft designs. Therefore, the aviation sector is likewise under governmental and international pressure to reduce the impact on the environment significantly.

Table 1.1. Environmental goals in policies of ICAO, EU and USA on Research and Development [9].

Environmental impact factor from aviation	**ICAO Policy Goals**	**EU ACARE Goals** (FP2050 till 2050)	**US FAA and NASA Goals** (NSTC2010 and CLEEN II till 2035)
Noise	Reduce the number of people affected by significant aircraft noise	Perceived noise emission of flying aircraft is reduced by 65%	52 dB reduction relative to cumulative margin of ICAO/FAA Stage 4 noise limit (a 25-year goal, by enabling N+3 aircraft and engines)
NO_x emissions	Reduce the impact of aviation emissions on local air quality	90% reduction in NO_x emissions	80% reduction in NOx emissions (for cruise relative to 2005 best in class and for LTO relative to ICAO CAEP/6 standard)
GHG emissions and fuel/energy consumption	Reduce the impact of aviation GHG emissions on the global climate: a reduction in net aviation CO_2 emissions of 50% by 2050, relative to 2005 levels	75% reduction in CO_2 emissions per passenger kilometre	60% reduction in Aircraft Fuel/Energy Consumption (CO_2 emissions per passenger kilometre) relative to 2000 best in class

Among the revolutionary expected changes in aircraft design are the full electric (FEV) and hybrid electric (HEV) aircraft vehicle concepts. These FEV and HEV concepts will compete with sustainable aviation fuels (SAFs) implementation in the aviation sector, including biofuels and hydrogen. Hydrogen and fuel cell technology has undergone significant development in the

last decade's industry technology outlook, and expert interviews consider an optimistic and achievable forecast of the performance of H_2 powerplant components for aircraft over the next decade.

Chapter 2

2. TECHNOLOGY SURVEY

Abstract

In this chapter, a technological survey has been carried out on the propulsion systems designed for the aeronautic field. The exploration encompasses an analysis of the primary configurations found in hybrid and electric propulsion systems while shedding light on the cutting-edge advancements proposed by leading international companies and esteemed research institutions. The aim is to provide valuable insights into the rapidly evolving landscape of aeronautic propulsion technologies. Furthermore, has been presented the latest developments in energy storage systems solutions. In particular, it focuses on the revolutionary potential of batteries and fuel cells within the aeronautic context. Moreover, an in-depth investigation into electric machines and power converters forms an integral part of the study, examining their key technical characteristics and exploring the untapped potential for growth in the aeronautic industry.

This chapter is a testament to the forefront of aeronautic propulsion technologies, paving the way for more efficient, sustainable, and groundbreaking advancements that will shape the future of flight.

2.1. Classification of Hybrid Electric Propulsion Architectures

2.1.1. History and State of Art

The first manned electric aircraft was the glider MB-E1 tested in 1973, almost 70 years after the Wright brothers successfully demonstrated the world's first fully controllable aircraft. The electrical drivetrain of the MB-E1 was revolutionary at that time. It utilized four Ni–Cd batteries as energy storage, which generated 100 V to drive a DC motor [10]. A few years later, the availability of solar cells and Ni–Cd batteries paved the way for the first manned solar-powered aircraft, which was demonstrated in 1979 [10]. Electrical drivetrains and aircraft structures in most of the early-stage demonstrations were not designed or optimized to integrate electrical

systems; rather, they were commercially available gliders converted simply by replacing the drivetrain. Although electric aircraft with small seat numbers are feasible in the near future (Table 2.1), drastic improvements in electrical drivetrains and energy storage are required to develop a full-electric passenger airplane.

Table 2.1. Principal planned full-electric aircraft in short term future.

Name	Year	Seats	MTOW	Endurance	Country	Notes
Pipistrel Alpha Electro	2015	2	600 kg	1h	Slovenia	Motor: E-811 57.6 kW Energy Storage: Lithium 22 kWh
Aviation Alice T-tail	2021	11	6350 kg	2h 45’	Israel	Motor: 2 x EM MagniX 650 (700 kW) Energy Storage: Kokam Lithium 820 kWh
NASA X-57 Maxwell IV	2020	2	1360 kg	1h	USA	Motor: 2 x EM (72 kW) 12 x EM (10.5 kW) Energy Storage: Lithium 69 kWh, 460Vdc. Aircraft Tecnam P2006T
Rolls Royce ACCEL	2020	1	1200 kg	30’	UK	Motor: 3 x EM YASA (200 kW) Energy Storage: Lithium 216kWh, 750Vdc.

The main advantages of full-electric technology for aircraft propulsion are highlighted below:

a) *Reduced emissions* – full-electric aircraft are powered solely by electric motors, which do not produce any direct emissions during flight. This significantly reduces the aircraft's carbon footprint and helps combat air pollution and climate change (only if electric energy is produced without carbon footprint);
b) *Lower operating costs* – electric propulsion systems can be more energy-efficient and have lower operating costs compared to traditional internal combustion engines. Electric motors have fewer moving parts, require less maintenance, and the cost of electricity is often lower than aviation fuels (thanks to the low cost of primary energy source (oil and gas);

c) *Quieter operations* – electric aircraft are considerably quieter than conventional aircraft with internal combustion engines. The absence of noisy jet engines enhances the flying experience for passengers and reduces noise pollution around airports and populated areas;
d) *Simplified design and aerodynamics* – electric propulsion systems offer more design flexibility, as they can be integrated into the aircraft structure more easily. This opens up possibilities for innovative aerodynamic designs that can improve fuel efficiency and overall performance.

Among the principal disadvantages of full-electric technology for aircraft propulsion includes:

a) *Limited range* – the biggest challenge for full-electric aircraft is the limited energy density of current battery technology. Batteries are heavy and have lower energy storage capacity compared to aviation fuels, resulting in limited range and payload capacity for electric aircraft;
b) *Long charging times* – recharging electric aircraft batteries can take a considerable amount of time, especially for large batteries required for commercial flights. This can lead to longer times on the ground and reduce aircraft utilization;
c) *Power and performance constraints* – electric motors may not provide the same level of power output as internal combustion engines, affecting the climb rate, speed, and payload capacity of electric aircraft;
d) *Charging infrastructure* – establishing a widespread charging infrastructure for electric aircraft is a significant challenge. Developing the necessary infrastructure at airports and other locations would require substantial investment and coordination.

Nowadays, regarding the actual technology, a reasonable compromise could be hybridization, where the integration of the electrification in the conventional propulsion system (piston or turbo engines). Based on the integration of the electrical motors in the propulsion system, they can have varying levels of hybridization. Some examples of hybrid aircraft prototypes have been summarized in the Table 2.2.

Table 2.2. Principal planned hybrid-electric aircraft in short term future.

Name	Year	Seats	MTOW (kg)	Endurance	Country	Notes
AMPIRE EEL	2019	6	2100	2h	USA	Parallel Hybrid Motor: 1 x Continental IO-360 (134 kW) 1 x EM (130 kW) Aircraft Cessna 337
XTI Tri Fan 600	2020	6	2857	2h	USA	Parallel Hybrid Motor: 1 x Honeywell HTS900 (745 kW) 4 x EM (260 kW)
VoltAero Cassio	2020	6	2500	3h 30’	France	Parallel Hybrid Motor: 1 x ICE (300 kW) 3 x EM Safran EngineUS (60 kW)

The main advantages of hybrid-electric technology for aircraft propulsion are highlighted below:

a) *Extended range and flexibility* – hybrid-electric aircraft combine the benefits of electric and internal combustion engines. They can use electric propulsion for efficient cruising and switch to internal combustion engines for take-off and climb phases, extending the aircraft's range and improving operational flexibility;
b) *Improved fuel efficiency* – by optimizing the use of electric and internal combustion engines, hybrid-electric aircraft can achieve better fuel efficiency compared to conventional aircraft;
c) *Transition to sustainable aviation* – hybrid-electric propulsion can serve as a transitional technology, allowing the aviation industry to gradually adopt more sustainable practices without a sudden and drastic change in infrastructure and operations.

Among the principal disadvantages of hybrid-electric technology for aircraft propulsion includes:

a) *Complexity and weight* – integrating multiple propulsion systems adds complexity to aircraft design and increases weight, which can impact overall efficiency and performance;

b) *Higher development and operational costs* – designing and producing hybrid-electric aircraft involves higher costs compared to conventional aircraft. Additionally, operating and maintaining the hybrid system can also be more expensive;
c) *Infrastructure requirements* – hybrid-electric aircraft still require charging infrastructure for their electric components, making it necessary to develop charging facilities at airports and other locations.

2.1.2. Electric Aircraft Hybridization

The success of HEV applications in the automobile industry is expected to be transferable to aviation. Indeed, hybrid automobiles benefit from increased range, noise reduction, low emissions, and minimal fuel burn, thereby spiking a significant interest in research into hybrid-electric propulsion technology for aviation applications. Nowadays, hybrid-electric vehicles are a widely discussed and well-known topic in literature, and numerous studies analyze this technology in terms of powertrain configuration, control strategies, and achievable benefits [11–14]. Generally, the hybrid-electric includes an electric rechargeable energy storage system (RESS), which is usually represented by a battery. The voltage and capacity of this component are chosen on the base of the desired power output, defining the degree of electrification of the vehicle. One or more electric motors (EM) are installed, as well, not only for traction purposes but even for transforming vehicle kinetic into electric energy for battery recharging during deceleration phases (braking). Therefore, the energy stored on board is chemical, flowing from the fuel tank to the internal combustion engine, and electrochemical, flowing from the battery to the electric machines and vice versa. The advantage of developing HEVs consists of combining the characteristics of pure-electric and conventional internal combustion engine (ICE) based vehicles to reduce the global energy consumption of the vehicle. The main benefits related to aircraft HEVs are:

a) *Regenerative braking* – the possibility to recover energy during deceleration phases instead of using mechanical brakes to dissipate it as heat. Recently, with the attention put on battery-powered cars, there has been considerable development in regenerative braking. Therefore, the kinetic energy of braking is changed into recharging the battery rather than heating the brake linings. Thus, technologies have become well-advanced for charging batteries with rapidly changing inputs, and the technologies are improving

rapidly. Therefore, it is reasonable to consider transferring this technology established in the automotive field to the aviation field to recharge the battery during the landing braking;

b) *Use the propeller as a generator* – use the propeller in "*windmill*" mode, extracting power as sink relative to the surrounding ascending air, turning the electric motor into a generator [15]. Charging is especially attractive on occasion when the airplane is in a strong up frontal current;
c) *Engine operating point can be optimized* – for a given speed, the operating point of the engine could be shifted to a higher efficiency area by increasing the requested torque, performing the so-called load point shift. This energy surplus can be used by the electric motor to recharge the battery. This functionality can be achieved with an energy management strategy of the power required to the engine;
d) *Downsizing* – to achieve better performance, the engine size could be reduced since electric machines can provide part of the torque requested for traction;
e) *Zero emission policy can be achieved* – in certain areas (for example, around the airports near population city centres) the use of the ICE engine could be prohibited to maintain air pollution levels below a certain threshold. This task can be achieved by a HEV by addressing the full amount of torque request to the electric motors.

2.1.3. Topologies and Classifications

Concerning HEVs, several categories can be defined on powertrain layout and thus energy flow [16], as shown in Figure 2.1. When referring to the hybrid-electric propulsion system (HEPS), there are:

a) *series topology* – it is similar to a pure electric drivetrain with the addition of the internal combustion engine as an auxiliary power unit. Generally, the latter isn't directly connected to the propeller, and no mechanical power summation occurs. Moreover, this configuration is also called range-extender, where the auxiliary power unit provides electrical energy as a generator set;
b) *parallel topology* – both the internal combustion engine and the electric motor(s) can directly propel the aircraft, so a mechanical power summation is possible;

c) *power split topology* – both series and parallel working modes are applied simultaneously. This layout allows higher degrees of freedom than the parallel one and higher efficiency than the series one;

d) *serial-parallel topology* – can act either as a series or as a parallel layout depending on the status of one or more clutches, and it is more flexible than the power split.

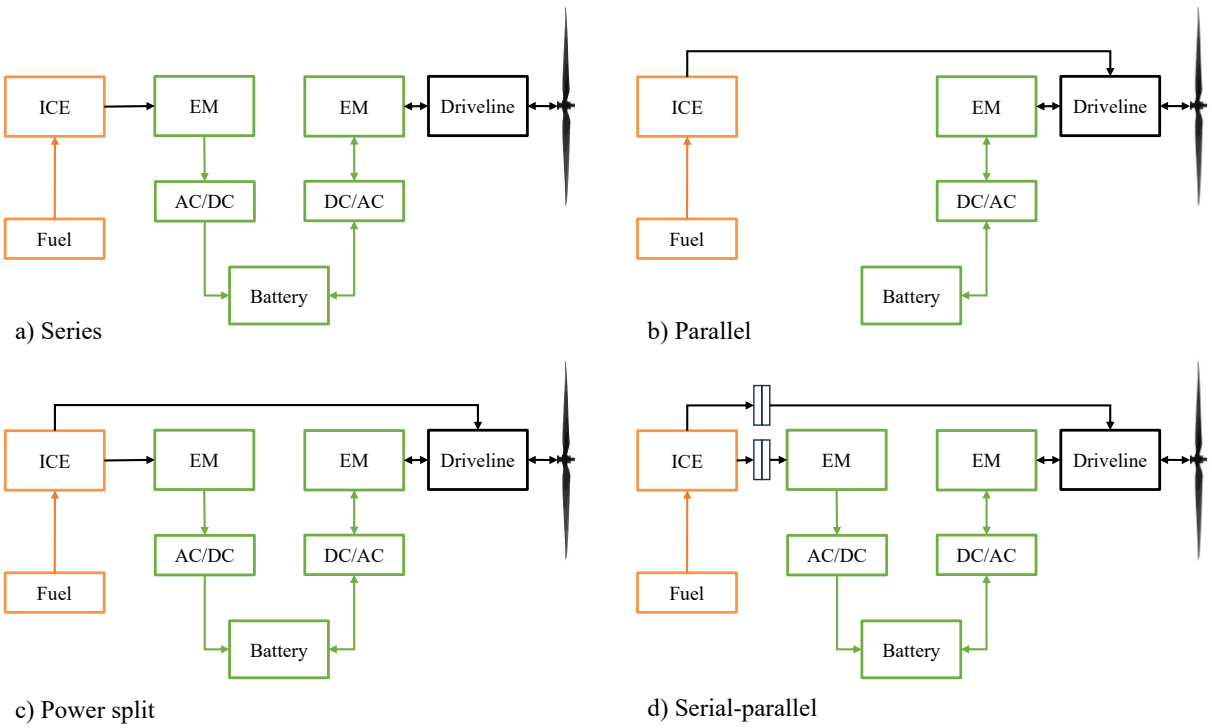

Figure 2.1. Hybrid electric propulsion system (HEPS) topologies for aircraft vehicle.

Referring to the HEPS parallel topology, several architectures based on electric machines' position within the driveline are possible. For this purpose, the nomenclature adopted for the automotive industry can be adopted. As shown in Figure 2.2, they are:

a) **P0** – the motor is coupled to the engine by mean of a belt. In this case, the electric machine is called Belt-driven Starter Generator (BSG);

b) **P1** – the motor/generator is directly mounted on the crankshaft upstream of the clutch. Here, the motor is an Integrated Starter Generator (ISG);

c) **P2** – the motor is still installed before the gearbox, but it is decoupled from the engine by a clutch and pure electric driving mode is available;

d) **P3** – the motor is mounted on the secondary shaft of the gearbox;

e) **P4** – regarding to the automotive application the motor is directly mounted on the front or rear axle. Generally, for aircraft application this configuration could be neglected.

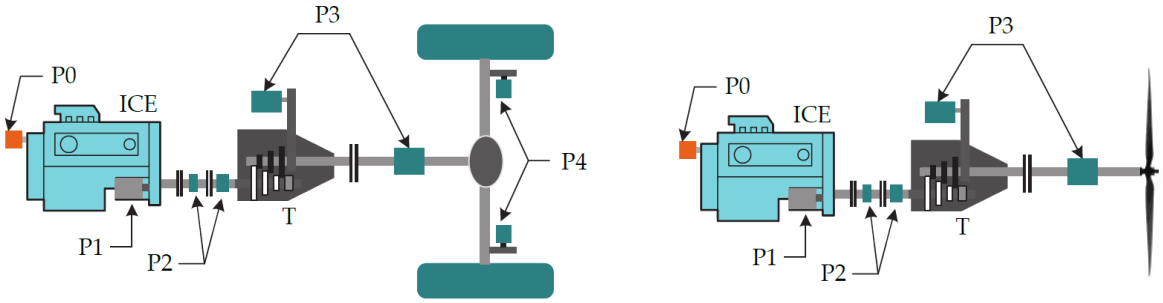

a) Automotive b) Aircraft

Figure 2.2. Parallel hybrid architectures depending on electric motor(s) position [16].

An additional classification of HEPSs can be made depending on their hybridization degree. The Degree of Hybridization (DoH) employed in such advanced systems cannot be suitably represented by a single parametric descriptor. Lorenz et al. [17] have argued a full description of any generic hybrid propulsion and power system requires two descriptors involving account of both the alternative energy source and that of the entire propulsion and power system: one ratio comparing each of the maximum installed powers (DoH_P); and, a second ratio comparing the extent of energy storage (DoH_E) of each, viz:

$$DoH_P = \frac{P_{INS,max,b}}{P_{INS,max,b} + P_{INS,max,a}} \tag{2.1}$$

$$DoH_E = \frac{E_b}{E_b + E_a} \tag{2.2}$$

where $P_{INS,max,b}$, $P_{INS,max,a}$ are, respectively, the maximum installed power deliverable by the secondary energy source (b – electrochemical energy) and the internal combustion engine (a – fuel energy); E_b, E_a are, respectively, the total stored electric energy "b" and fuel one "a" (for example Jet-A1, AVGAS).

In order to elucidate why such a dual set of parametric descriptors is necessary, must consider the limit conditions:

a) *conventional vehicle (no electrification)* – $DoH_P = 0$ and $DoH_E = 0$, the chemical energy of the fuel is the only on-board energy source. The driver torque request is fully provided by an internal combustion engine;

b) *Pure series* – $DoH_P = 1$ and $DoH_E = 0$, where only electrical power is provided at the propulsive device(s) but energy storage is solely fuel based;

c) *Full electric* – $DoH_P = 1$ and $DoH_E = 1$, where only electric power is provided at the propulsive device(s) but energy storage is solely electrochemically (battery based), called also electric vehicle (EV).

A broader, automotive-derived classification sowed in Figure 2.3, with ascending electrification degree, can be considered; it is clear that an appropriate consideration for the aviation field is necessary:

a) *Micro Hybrid* – the installed battery cannot be used for traction. The degree of electrification is so minimum that a micro HEV can be considered as a conventional vehicle with only the Start-Stop function available;
b) *Mild Hybrid* – the higher capacity of the battery allows not only the regenerative braking or windmill mode, but also motor assist, thus improving the driveability of the aircraft (lower torque oscillations), especially at low speed (turbo-lag reduction). Although power boosting is available, all-electric driving mode cannot be applied;
c) *Full Hybrid* – the capacity of the battery is high enough to perform pure electric driving and thus to completely fulfil the electric traction;
d) *Plug-in Hybrid* – it presents an off-vehicle charging (OVC) function which is justified by the higher capacity of the high-voltage battery. The reason is that this kind of vehicles has been conceived to operate in all-electric driving mode so as to cover the average daily travelled distance in a short range cycle. Thus, the standard operating mode of a plug-in hybrid electric vehicle (PHEV) is represented by an initial charge depleting phase, during which the usage of the electric energy is encouraged as much as possible, followed by a charge sustaining phase, aimed at maintaining the state of charge (SoC) of the battery almost constant and low, within a certain narrow range.

The electrical assistance related to *Micro Hybrid* and *Mild Hybrid* in aviation has little use. The mission cycle of an aircraft is distinctly different from the urban cycle performed by a car, where the level of assistance is necessarily different.

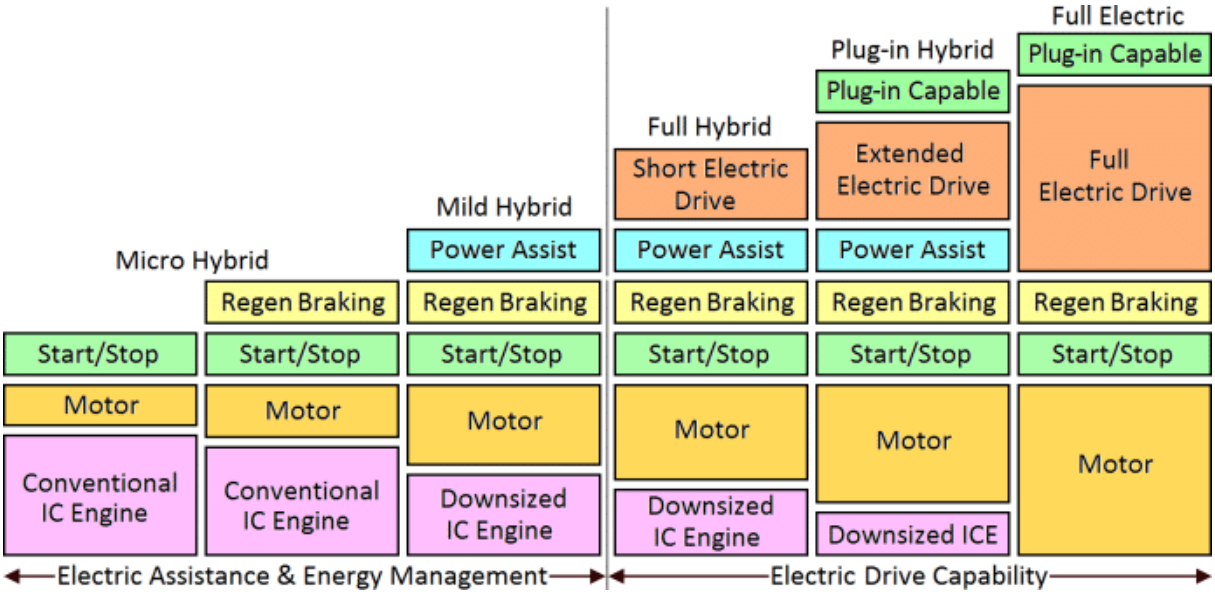

Figure 2.3. Classification and features of Hybrid EVs [18].

2.2. Energy Storage Systems

The energy storage system (ESS) is an important aspect to consider while analyzing the differences with conventional airplanes: as standard aviation fuel is characterized by very high energy density[1], around $12000 - 13000\ Wh\ kg^{-1}$, while the batteries are generally much less dense in terms of energy. Conventional thermal engines need a certain fuel flow rate to the combustion chamber, regardless of the kind of engine and thermal cycle: what is needed to produce mechanical power is derived from combustion; the flow rate is provided by a pumping system, whose design is conducted with high flexibility, since the size is not forced by tank size. Generally, this approach is not true for batteries, where the requirements in terms of energy and power are not decoupled as for conventional systems. Near and far-term technologies are compared using the Ragone plot [19], where the relationship between specific power and energy (at the cell level in the case of batteries) is shown in a log-log plot (Figure 2.4).

The principal ESS technology that ensure, in the short term, good capability in terms of energy storage, good performance in terms of power and density weight, low environmental impact of use are without doubt: batteries and fuel cells. The capacitors and supercapacitors are instantaneously storage device that ensure engine-driven protection against instantaneously load changes, able to remove critical voltage transient from DC bus. The latter have a lower

[1] Low Heat Value (LHV) of aviation Jet-A1 (kerosene) is around $43 - 44\ MJ\ kg^{-1}$; ($1\ Wh = 3.6 \cdot kJ$)

energy density, respect to batteries and fuel cell, therefore they are not applicable alone in aeronautical field.

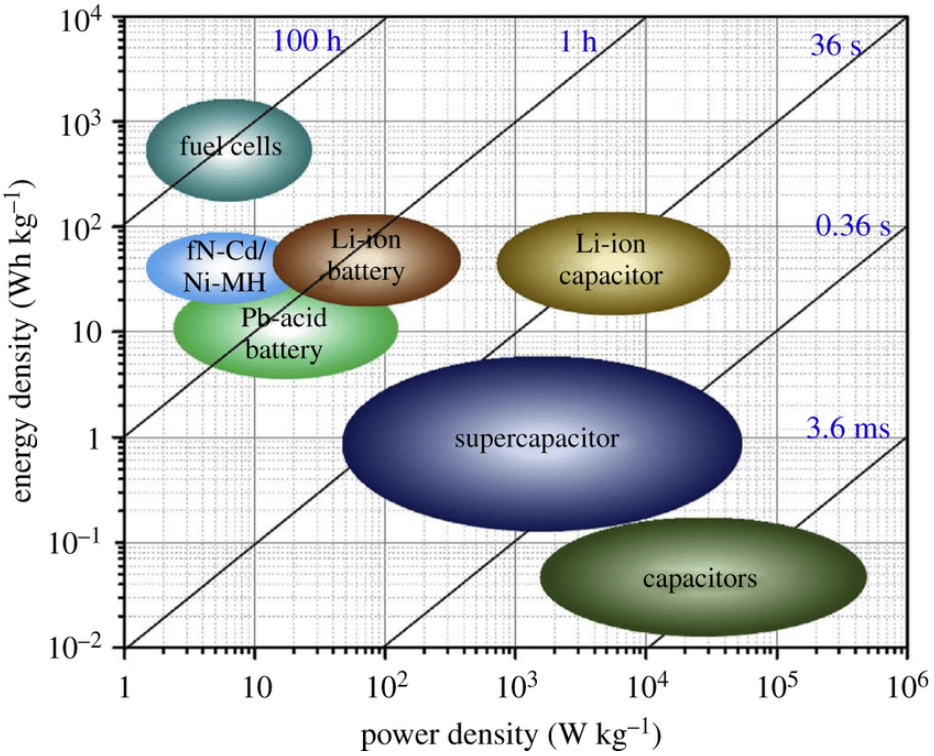

Figure 2.4. Ragone plot of different energy storage devices [19].

2.2.1. Batteries

Research in battery technology is advancing rapidly, mainly due to the growing popularity of electric vehicles [20]. The successful application of batteries in powering aviation has been demonstrated by the trainers Pipistrel's Electro (Table 2.1) with batteries with specific energy densities between 250 and 270 Wh/kg. However, as cited by Uber-Elevate in 2016 [21], energy densities of 400 Wh/kg and above are required for electric aviation to take off fully. Tesla and SpaceX founder Elon Musk also echoed that batteries with an energy density of 400 Wh/kg with a high cycle life could be realized within 3 to 4 years. Therefore, it is evident that significant improvement in battery technology will characterize the possible application and time-to-market of electric aircraft. Armand and Tarascon [22] specify that the ideal battery for use in airplanes should be light, rechargeable, safer, have long durability, and have the highest energy density possible. The batteries are electrochemical storage device, each one are composed of individual cells filled with a conducting medium (electrolyte) that, when

connected together, form a battery. Multiple batteries are connected in series to forma a battery bank or string or module. There are two main types of batteries: non-rechargeable and rechargeable. This last one are further divided into two categories based on the operating temperature of electrolyte. Ambient operating temperature batteries (molten electrodes) have either solid or molten (electrolytes).

Some definitions:

a) *Capacity* – usually rated in Ah (or in terms of energy Wh) is the current witch can be delivered by the battery under specified conditions. Capacity decreases as discharge current increases and temperature decreases

$$C_{nom} = \int P(t)\, dt\ (Ah) \tag{2.3}$$

$$P = V \cdot I\ (W) \tag{2.4}$$

$$E_{nom} = C_{nom} \cdot V\ (Wh) \tag{2.4}$$

where C_{nom} is the nominal battery capacity in (Ah), P battery power, V battery voltage, I battery current and E_{nom} is the nominal battery capacity in terms of energy (Wh);

b) *C-rate* – An expression describing the current (charge or discharge) in normalized form. The denominator number indicates the number of hours to completely discharge (or charge) the battery at constant current. So $\frac{C}{20} = 0.05C$ is the current draw at which the battery will last for 20h, $\frac{C}{1} = 1C$ is the current at which the battery will last 1h;

c) *State of charge (SoC)* – is a dimensionless value that describes the amount of usable charge that remains in the energy storage system compared to the total charge capacity (under nominal conditions). SoC can be expressed as a percent of total and will be measured by monitoring the Coulombic charge quantity IN and OUT of the battery pack

$$SoC(t) = SoC_0 - \frac{\int_0^t I(t)dt}{E_{nom}}\ ; \quad where\ \begin{cases} Discharge, & I \geq 0 \\ Charge, & I < 0 \end{cases} \tag{2.5}$$

d) *State of energy (SoE)* – is used in replacement of the SoC to indicate the effective battery capacity in terms of energy content.

$$SoE(t) = SoE_0 - \frac{\int_0^t V(t) \cdot I(t) dt}{E_{nom}} \tag{2.6}$$

In Figure 2.5 are compared the theoretical, expected, and state-of-the-art (SOA) energy densities of lithium-based battery chemistries, demonstrating their significant potential in aviation.

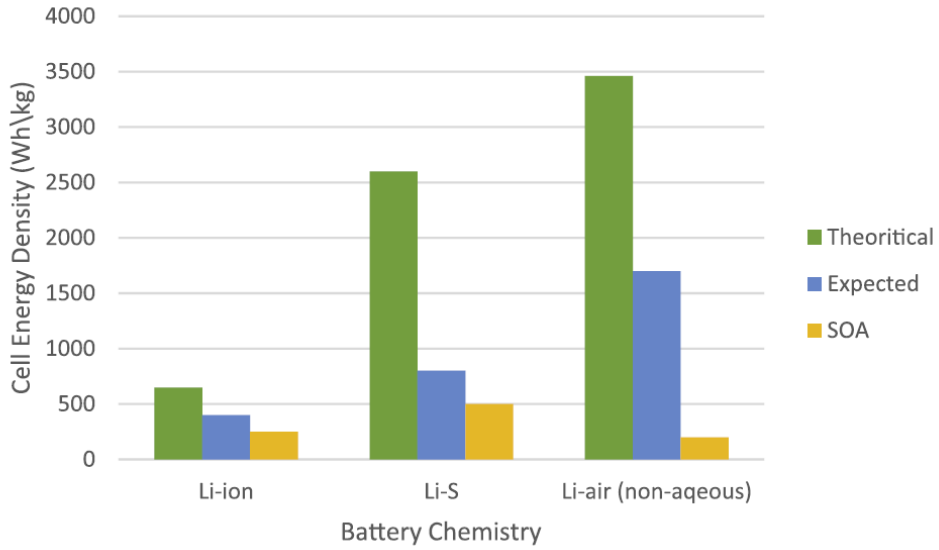

Figure 2.5. Comparison of cell-level energy densities of potential battery chemistries for aviation applications [23].

a) *Lithium-Ion* – Li-ion batteries are becoming increasingly popular in research and development for electric aviation due to their higher specific power and demonstrated success in portable electronic devices and the automobile industry [22]. Comparing Li-ion to other high-quality rechargeable battery technologies such as nickel-cadmium (Ni-Cd) or nickel-metal-hydride (Ni-MH), Li-ion cells have higher energy densities as well as higher cell voltage up to 3.6 V, which is three times greater than these battery technologies. This implies that they can produce a large amount of current for high-power applications. However, despite the technological success and promise of Li-ion technology, several challenges restrict their application and raise numerous concerns regarding safety and lower specific energy compared to jet fuels. Li-ion batteries can overheat at higher voltages, resulting in battery damage leading to thermal runaway and explosion [24], which led to the grounding of the Boeing 787 fleet when onboard battery

fires were reported. Li-ion battery technology has achieved specific energy densities over 250 Wh/kg and is currently the technology to which all other potential battery technologies for aviation and automobile applications are compared;

b) *Lithium-Sulfur* – Li-S batteries consist of a lithium metal anode and a sulfur-based cathode and possess a high theoretical energy density of 2600 Wh/kg (Figure 2.5), making it the most promising choice for energy storage for large-scale grids and aviation applications. Moreover, sulfur is abundant, cheap, nontoxic, and light in nature, making it suitable for weight-sensitive applications such as aviation. Unfortunately, there are many technical against: sulfur is non-conductive needed conductive additives, but the electron mitigation remain very slow 0.2C in discharge; short cycle life caused by the lithium polysulfides formed during the conversion reaction can dissolve in the electrolyte producing a shuttle effect which results in a low sulfur utilization. The application of Li-S in aviation was successfully demonstrated by the Airbus Zephyr aircraft, which made the longest endurance flight of 14 days [25];
c) *Lithium-Air* – Li-Air belong to the family of solid-state batteries and they are a type of rechargeable batteries that use oxygen from the air as a reactant to produce electricity. Oxygen reacts with lithium at the cathode to form lithium oxides during discharge. Li-air batteries promise a very high theoretical capacity, which means they can store a significant amount of energy for their weight around 3460 Wh/kg. However, these batteries still need to overcome some significant technical challenges, such as cathode stability and managing the generated electricity. At present, no practical application of a Li-air battery exists, but Airbus is considering a Li-air battery to power the Voltair aircraft they estimate to enter the market in 2035.

2.2.2. Fuel Cell

In aeronautical field the electric powertrains based on fuel cells (FCs), ensure different achievement, which, more energy conversion efficiency respect to traditional thermodynamical one and also the multifunctional integration of fuel cells into aircraft through the recovery of by-products (water, heat or oxygen-depleted exhaust air), allows fuel cells to be used for vital processes like de-icing, cabin air conditioning, water supply, and fire suppression of luggage compartment or fuel tanks. Moreover, the fuel cell-powered aircrafts also produce very low emissions during flight, and no C-based molecules [26-27].

A fuel cell (FCs) is an electrochemical device, which directly combines a fuel and oxidizer to generate electricity, with water, heat and possibly CO_2, ad by-products. Unlike batteries, fuel cells cannot store energy and require an external fuel source. By contrast with combustion-based energy converters (ICE, Turbofans, etc), where the efficiency is limited to the Carnot efficiency:

$$\eta_{Carnot} = \frac{T_H - T_L}{T_H} \tag{2.7}$$

Fuel efficiency is limited by the Gibbs free energy, Δg_f the thermodynamic potential in kJ/mol, which is the maximum amount of energy that can be extracted from a thermodynamically closed system, where $-\Delta h_f$ is the Heating Value (Lower LHV or Higher HHV), and also it is negative when energy is released.

$$\eta_{max} = \frac{\Delta g_f}{-\Delta h_f} \tag{2.8}$$

For the hydrogen fuel cell, two electrons pass round the external circuit for each water molecule produced and each molecule of hydrogen used. So, for a one mole of hydrogen used 2N electrons pass round the external circuit (where N is Avogadro's number $6.022 \cdot 10^{-23}\ mole$). If -e is the charge on one electron ($1.602 \cdot 10^{-19}\ Coulomb$) , then the charge that flows is

$$-2Ne = -2F\ (Coulomb) \tag{2.9}$$

F being the Faraday constant ($96.48\ Coulomb$), or the charge on one mole of electrons.
If E is the voltage of the fuel cell, then the electrical work done moving this charge round the circuits is

$$Electrical\ work\ done = charge\ x\ voltage = -2FE\ (Joule) \tag{2.10}$$

If the system is reversible (or has no losses), than this electrical work done be equal to the Gibbs free energy released Δg_f. So

$$\Delta g_f = -2FE \tag{2.11}$$

Thus

$$E = -\frac{\Delta g_f}{2F} \tag{2.12}$$

This fundamental equation gives the electromotive force (EMF) or reversible open circuit voltage (OCV) of the hydrogen fuel cell [28].

In order to implement an electrification strategy in the aviation sector, the first question is in what form the required energy can be stored/transported [29]. The principal fuel/carrier used in FCs are:

a) *Hydrogen* (H_2) – the hydrogen is the most common energy carrier used in Fcs. It is used in Proton Exchange Membrane Fuel Cells (PEMFCs), Solid Oxide Fuel Cells (SOFCs), and other types of Fcs. The primary reaction is the oxidation of hydrogen to produce water, heat and electrical energy. Production can be energy intensive: Electrolysis is 80% efficient, thermo-chemical splitting is 45-55% efficient. This energy carrier requires a storage methods such as:

- Compressed gas Hydrogen (C-H_2) typically compressed at 700 bar to increase its density up to 42 kg/m^3, while maintaining ambient temperature;
- Liquid Hydrogen (L-H_2) is liquefied by lowering its temperature to 20 K, resulting in a density of about 71 kg/m^3;
- Cryo-compressed gas Hydrogen (Cc-H_2) this is a hybrid method that combines the techniques of compressed and liquid storage. Cryo-compressed hydrogen is typically stored at pressures in the range of 50–700 bar and temperatures of 25–110 K;
- Metal organic frameworks (MOFs) are formed by the self-assembly of inorganic metal clusters or ions and organic linkers. The physisorption process occurs by exploiting the nanoporous structure of the MOF. The van der Walls interactions between the hydrogen molecules and the sorbent are formed by an exothermic reaction; hydrogen is then released by supplying heat (endothermic reaction);
- Metal hydrides (MH) consists of a tank filled with metal alloys capable of forming weak bonds with hydrogen at not very high pressure (usually 10–40 bar) to achieve solid hydrogen storage.

b) *Alcohols and gaseous hydrocarbons* – usually are adopted Methanol (CH_3OH), Ethanol (C_2H_5OH), and Natural gas (CH_4). Depending on type of fuel cell, may require reforming to produce pure hydrogen, i.e., extracting hydrogen from fuels which have hydrogen in their chemical composition. These fuels are increasingly available and infrastructure to handle them is expanding;

c) *Liquid hydrocarbons* – usually are adopted (Gasoline, Oil, Kerosene, Naphtha, biomass, etc). Requires reformation depending on fuel cell type.

2.3. Electric Machines

The electric machines (EMs) can be broadly organized into two main categories: alternate current (AC) and direct current (DC). The DC, synchronous and induction EMs all find potential uses in vehicles as starters, alternators, and for various forms of actuation. In most recent HEV and EV vehicles, three classes of AC machines have been applied including induction machines, synchronous machines, permanent magnet machines and variable reluctance machines (Figure 2.6). Various configurations of machines have been used or are potential motors to be used, including radial flux and axial flux permanent magnet synchronous machines, induction machines, switched reluctance machines and flux switching machines [30].

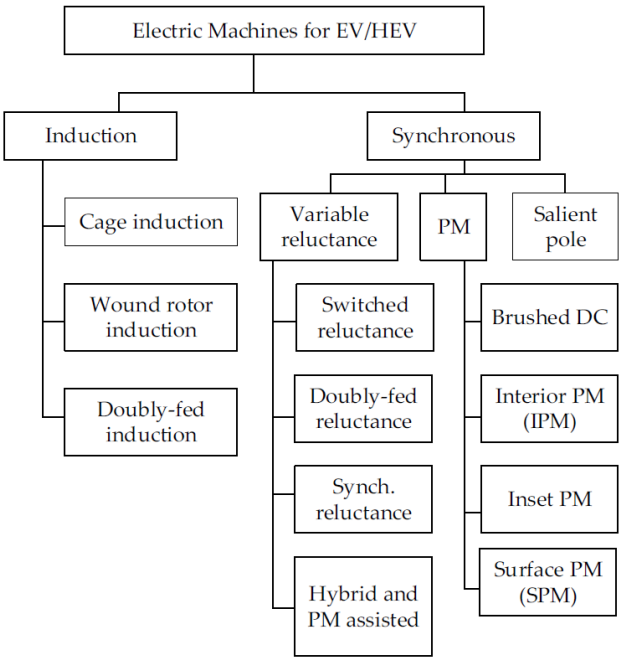

Figure 2.6. AC Motor types available for electric vehicles/hybrid electric vehicles (EV/HEVs) [30].

a) *Induction Machines* (IM) – Squirrel cage induction machines have a rich history as the most widely used machines in industry. The most important advantages of this machines include high peak torque, good dynamic response, and very low maintenance requirement in all aspects of operation. Notable automotive applications include the GM EV-1 vehicle, and earlier models from the Tesla Motor Corporation. Nowadays, the die-cast copper rotor technology is considered a mature technology that can provide a path to high efficiency machines due to reduced losses in the rotor, and these reduced losses in the rotor can further result in reduced need for cooling. The electromagnetic torque of the induction machine can be written as:

$$T = \frac{mpV_s^2(R_r'/s)}{2\pi f_s\left[\left(R_s + \frac{R_r'}{s}\right)^2 + X_k^2\right]} \tag{2.13}$$

where T is the machine torque, m is the number of phases, p is the number of pole pairs, V_s. is phase voltage, f_s is supply frequency, s is the slip, R_r' is rotor resistance, R_s is stator resistance, and X_k is the equivalent short circuit reactance of the rotor and stator. From a magnetic perspective that emphasizes the importance of the slot area and flux densities, the torque can be approximated as:

$$T \propto \left(1 - \frac{B_g}{K_{iron} \cdot B_t}\right) \cdot B_g \cdot \sigma \cdot h_s \cdot R_g^2 \cdot L \tag{2.14}$$

where B_t is tooth flux density, B_g is air gap flux density, L is active length, and R_g is the mean radius of the machine airgap, h_s is tooth height, σ is current density, K_{iron} is the lamination stacking factor [30-32]. Equation (2.14) emphasizes the fact that a high flux density in the airgap, and high rotor current density are both important for high electromagnetic torque. The maximum torque is directly proportional to the square of the voltage (or square of the flux) and inversely proportional to the supply frequency. For traction applications these machines are normally coupled with an inverter;

b) *Permanent Magnet Synchronous Machines* (PMSM) – The majority of the machines currently used in vehicles are permanent magnet machines. The increasing requirements of high efficiency, high specific power, and high power density caused a shift toward permanent magnet machines, such as the departure from the traditional induction

machines previously used in the Tesla Model S toward permanent magnet-based technologies in the Tesla Model 3. There are various topologies and classifications of permanent magnet machines, but the rotor design serves as a basic feature of classification of permanent magnet machines into two broad categories: surface permanent magnet (SPM) and interior permanent magnet machines (IPM). The rotor design influences several important features of the machine, including the constant power speed range. The electromagnetic torque equation of the permanent magnet synchronous machine in the d-q reference frame can be expressed as:

$$T = \frac{3}{2} p \cdot \left[\lambda_{pm} i_q - \left(L_q - L_d \right) \cdot i_d i_q \right] \tag{2.15}$$

where p is the number of pole pairs, λ_{pm} is the permanent magnet flux, i_d and i_q are the d-axis and q-axis currents, and L_d and L_q are inductances. The trend has been focused on measures to increase the flux linkage due to the magnets and thereby the magnet torque component (first term in bracket) as well as increasing the saliency between the d- and q- axes in order to increase the reluctance component of the torque, which is the second term of the bracket. The reluctance torque can mathematically be maximized by increasing L_q (through increased q-axis permeance) and reducing L_d (permeance along d-axis) to a level that is consistent with the desired flux weakening capability as L_d directly affects the machine's characteristic current. In order to increase the flux linkage, it is important to reduce flux leakage and measures must be adopted in that regard as well, with innovative design of flux barriers. For this purposes the rotor design of these machines has progressed from basic flat magnets through various configurations of U-, V-, W-shaped magnets and double V-shaped and several others, including variations in magnet sizes from pole to pole. Regarding to the stator, a concentrated windings design respect to distributed one, have shorter end windings leading to lower copper loss than the distributed windings, with the latter typically having longer end turns and consequent higher Joule losses. Finally, a type of permanent magnet machine that is increasingly being touted is the axial flux machine (AxFM). The AxFMs have desirable characteristics for traction applications such as high power density, high efficiency, compact and modular structure, low weight and high fault tolerance. These characteristics are possible because their structure trades length for diameter and allows

to take advantage of torque production on multiple surfaces, with shorter current paths in the machine [30-32];

c) *Variable Reluctance Machines* (VRM) – two important machine topologies that operate on the reluctance principle to produce torque are the synchronous reluctance (SynRM) machine and switched reluctance machine (SRM). Both machines have simple construction of a rotor composed of only thin steel laminations with no windings or magnets, the difference between the rotors being that SRM has salient pole construction while the SynRM is typically non-salient, even though it can be designed with saliency. Another difference between the construction of the machines is that the stator of the SRM is salient and wound with concentrated coils around each pole, while that of the SynRM typically has a distributed winding. SynRMs are appealing in terms of their robustness, high efficiency, low torque ripple and simplicity (low cost) of control. These machines have only recently been commercially available for industrial applications as they are seen as a great alternative to variable speed-controlled induction machines. However, SynRMs have a disadvantage with low power factor which affects their operational performance and the power converter sizing. The torque T, and power factor, $cos\varphi$, of the SynRM is given by Equations (2.16) and (2.17), where L_d and L_q are d- and q-axis inductances respectively, i_d and i_q are d- and q-axis currents respectively and ξ is the saliency ratio, defined here as L_d/L_q. As shown, both the electromagnetic torque and power factor are dependent on the saliency ratio and in order to improve machine performance, they must be designed with a high saliency ratio, ξ, which is a ratio of maximum inductance to minimum inductance as a result of the differences in the permeance along the d-axis and the q-axis.

$$T = \frac{3}{2}\frac{p}{2} \cdot \left[\left(L_d - L_q\right) \cdot i_d i_q\right] \tag{2.16}$$

$$cos\varphi = \frac{\xi - 1}{\xi + 1} \tag{2.17}$$

The SRM machines can achieve high constant power speed range and high efficiency but it seems that the noise and torque ripple continue to be a major barrier to application. During the last several years, there has been significant research toward low torque ripple designs including elimination through the design of the power electronic controls. However, there is currently a

growing need for machines without magnet content and SRM may be a strong contender for candidate motors [30-32].

2.4. Electric Drivers and Power Converters

A drive is the power electronics used to control an electric machine. Drives may use various techniques to control the speed, torque, voltage and current of electric machines. Generally, an electrical vehicles networks of HEV, and EV feature diverse AC and DC buses rated at a distinct voltage level and frequency range (Figure 2.7).

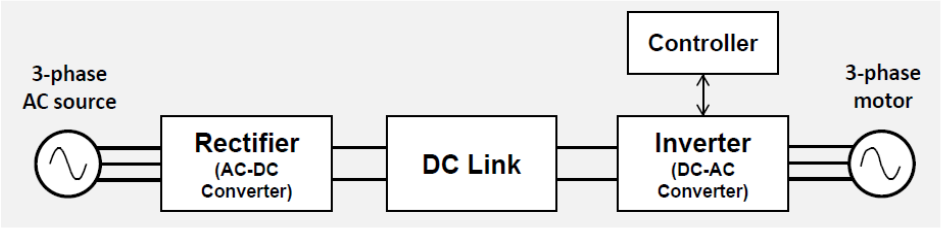

(a)

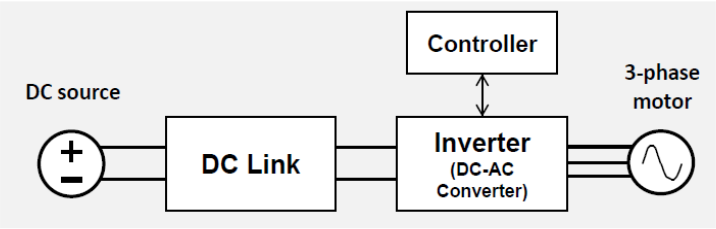

(b)

Figure 2.7. Electric chain: (a) Series Hybrid or regenerative HEV; (b) used for battery EV [32].

In Table 2.3 are compared several powertrains and propulsion DC/AC converter power ratings in electric propulsion for different aircraft categories.

Table 2.3. Comparison of Power Ratings in Powertrain and Propulsion DC/AC Converters for Different HEV and EV Aircraft Categories [33].

Aircraft categories	**Powertrain propulsion power**	**DC-Link Voltage**	**Examples of propulsion DC/AC converters**
General Aviation or recreational	<300 kW	<600 V	100 kW in Hypstair 60kW in X-57 Maxwell
Urban mobility	500-800 kW	<800 V	100 kW in CityAirbus 100 kW in Bell Nexus
Regional and business	500kW – 3MW	Unknown	No prototypes
Large commercial	>2MW	1000-3000 V	1MW in STARC-ABL N3X

Regardless of the electrification degree, each airplane architecture is composed of both AC and DC electrical systems, if used for aircraft propulsion are also called primary system, while secondary system, if used as supplier of the avionic ed electronic on board. In Table 2.4 are summarizes the popular topologies used in the industry and the applications of the converters in each aircraft architecture.

Table 2.4. Summary of Power Converters Topologies and Applications in Aircraft Architectures [33].

Converters	**Popular Industrial topologies**	**Application in aircraft architectures**
AC/DC	TRU passive three-phase rectifier	Secondary and/or propulsion system in turbo and hybrid electric aircraft
DC/AC	VSI	Secondary and/or propulsion system in turbo and hybrid electric aircraft
AC/AC	Two-level back-to-back converter	Secondary system
DC/DC	DAB topology	Secondary system

a) *AC/DC* – also called Rectifier are connected to the main AC bus and convert the AC power to the DC network. In all-electric aircraft do not need AC/DC converters in their powertrain as energy storage systems are DC components Figure 2.7 (b) . Due to the lack of AC energy storing solutions, regenerative power is not allowed in aircraft, and only unidirectional topologies are considered to protect the main AC network. When a large voltage ratio conversion is required, transformer rectifier units (TRUs), composed

of a transformer in series with a rectifier, are used to provide galvanic isolation between the 115 VAC (or 230 VAC) and 28 VDC buses [32, 34];

b) *DC/AC* – also called Inverter or Voltage-Source Inverter (VSI) is the most common topologies have been proposed for aerospace applications. Generally, the VSI are used to drive the permanent magnet synchronous machines. Next-generation of DC/AC is based on silicon carbide (SiC) an higher performance material [32, 34];

c) *AC/AC* – two principal configuration topologies are know: back-to-back converters and matrix converters. The latter directly converts the AC power, while back-to-back converters, or AC/DC/AC converters, are two-stage configurations separated by a DC-link capacitor. The matrix converters application is limited to a few areas that feature low dynamic behavior [32, 34];

d) *DC/DC* – also called step-Up or step-Down. The latter are useful in aerospace industry to step down the high voltage DC 135Vdc to 28Vdc. The dual active bridge (DAB) is one of the most popular soft-switching topologies to achieve power conversion at high efficiency and power density [32, 34].

Chapter 3

3. EXPERIMENTAL SETUP AND TESTING ACTIVITIES

Abstract

This chapter describes the experimental setup of the hybrid-electric propulsion system (HEPS) prototype and the testing activities. The HEPS prototype consists of a parallel hybrid configuration where an internal combustion engine and an electric machine are directly engaged to the propeller. The first paragraph will be discussed, in detail, the mechanical coupling between the two engines.

Furthermore, the experimental HW and SW setup consisting of data acquisition and remote control systems have been described. The data acquisition system has been developed in-house using National Instruments modules and programmed in LabView.

Preliminary tests have been performed on the hybrid powertrain in steady-state conditions to verify the operating range of the prototype under examination and evaluate its performance under different test conditions.

Finally, an experimental transient investigation has been made considering a short mission where the HEPS has been tested in hybrid and charging operating modes.

3.1. Experimental Setup

The main aim regarding the design of a new aeronautical hybrid-electric propulsion system start the European-founded project named DIPROVEL, which was born to equip general and light aviation aircraft with a propulsion system that is more efficient, safer, and less noisy, therefore in line with the goals set by the Flightpath 2050 by the European Union.

The HEPS design requirements find justification around the following points:

- *Performances and efficiency* – the performances are referred to the benchmark Continental IO-360 engine, with the aim to increase the efficiency by at least 5%;
- *Airworthiness* – a least invasive mechanical coupling between the two systems produces a reasonable reduction of the effort during the aviation certification process;

- *Operability and flexibility* – lithium-ion batteries must be adopted, combined with the propulsion system's ability to recharge the batteries in flight;
- *Safety and reliability* – take reliability and safety aspects into account at the design stage.

An experimental testing activity necessary for evaluating the functionality of the HEPS has been conducted on the prototype under consideration. The tests were conducted at the Hybrid engine test bed of the Department of Industrial Engineering of the University of Naples Federico II, located at Via Claudio 21, Building 4.

The internal combustion engine adopted in the first HEPS prototype is the CMD22 and its maximum flight performances declared by the manufacturer are shown in Table 3.1. This engine has been certificated for airworthiness by the European Aviation Safety Agency (EASA) with the issuance of a Type-Certificate (No.E.120). The choice of this engine is mainly related to the presence of aero engine manufacturer CMD S.p.a. (a Loncin Company) as the lead partner in the DIPROVEL project. The HEPS performances have been referred to the benchmark Continental IO-360 engine, where the flight point performances are highlighted in Table 3.1.

In order to ensure the same performance between the HEPS prototype and the benchmark one, a commercial survey has been conducted to identify all the components necessary to build the new hybrid propulsion system. For this purpose, an electric machine (EM) EMRAX 268 LV has been selected. In particular, this EM is able to provide around 60 kW at (2750÷2800 rpm). Moreover, the EM has been electrically connected to an inverter GVI produced by Parker Company.

The mechanical and electrical coupling between ICE and EM motors was designed during the Ph.D. period. In addition, a data acquisition system (DaQ) has been developed starting from National Instruments Hardware and LabView Software.

Table 3.1. Engine flight ratings.

Mission operating points	UoM	CONTINENTAL IO-360	CMD 22
Max. Take-off Power (5-min)	Hp	210	130
Max. Take-off Power (5-min)	kW	157	95
Max. Take-off Speed (5-min)	RPM	2800	2750
Max. Cont. Power	Hp	195	118
Max. Cont. Power	kW	145	87
Max. Cont. Speed	RPM	2800	2500
Cruise 75% Max. Cont. Power	Hp	146	88
Cruise 75% Max. Cont. Power	kW	109	65
Cruise 75% Max. Cont. Speed	RPM	2600	2400
Cons. Max. Cont. Power	kg/h	46,2	25,6
Cons. Cruise 75% Max. Cont. Power	kg/h	30,8	19,6

3.1.1. Mechanical design: prototype layout

The proposed hybrid electric powertrain architecture consists of a parallel layout, where both the internal combustion engine ICE and electrical machines EM provide power P_{ICE} and P_{EM} to the propeller (Figure 3.1). The propeller power P_{prop} is obtained by the sum of the two power sources through this equation:

$$P_{prop} = P_{ICE} + P_{EM} \tag{3.1}$$

Where P_{EM} could be positive or negative depending on the flight phase. Generally, in take-off or climb phases, the EM works as a motor, while the EM works as a generator in descending or landing phases. In fact, during the descending and landing phases, the ICE over-power could be employed to generate electrical energy to recharge the battery.

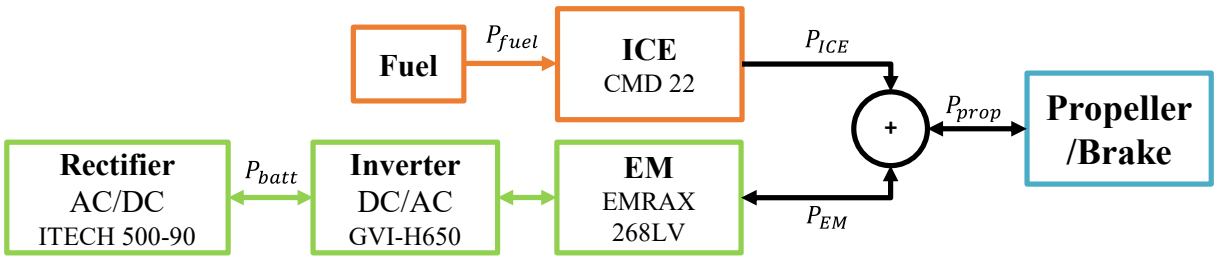

Figure 3.1. Scheme of the hybrid-electric propulsion system.

The hybrid-electric propulsion system must be compliance with the design requirements in terms of performance and efficiency, able to replace the Continental IO360 engine propulsion of a Cessna 337 equipped with a conventional propeller, with a maximum take-off power of 157 kW (210 Hp) at 2750 rpm of propeller speed. The net propeller power $Pprop$ is produced by combining these two power sources through Equation 3.1. The decision to connect the electric motor to the propeller shaft finds justification in a design requirement, able to reduce the certification impact. In fact, the application of the electric machine on the crankshaft, rather than the propeller shaft, is considered an invasive modification by the certificate institute European Aviation Safety Agency (EASA) and therefore requires significant additions to issue a new airworthiness certification (i.e., CS 22.1819 Durability, CS 22.1833 Vibration, CS 22.1749 Endurance test, etc.). The additional power rate on the crankshaft involves a necessary structural verification of the powertrain. Moreover, if the obtained results are not compliant, a new powertrain redesign is required. In addition, the connection of the electric motor downstream of the transmission chain is an inherent reliability form. A reasonable ICE failure and subsequent shutdown allow the propeller to run by electric propulsion alone if a non-rigid coupling between the two engines is considered. In addition, a non-rigid coupling ensured to work in four different modes:

- *fuel-only*, in this case, ICE and EM are running, but only ICE transferred power to the propeller, while the EM running as a flywheel;
- *battery-only*, in this case, only the EM is running as a motor, and the propeller power is equal to the EM power;
- *hybrid*, in this case, both ICE and EM are running, and the propeller power is a sum of ICE and EM power;
- *charging*, in this case, ICE and EM are running, but the last one works as a generator to charge the battery, while the ICE provides power both to the propeller shaft and EM.

For this purpose, a high power density permanent magnet synchronous machine (PMSM) has been chosen that ensures at 2750 rpm a continuous power of 62 kW and good efficiency around 95-96%.

Moreover, applying the following equation can calculate the degree of hybridization (DoH) of the current HEPS prototype:

$$DoH_P = \frac{P_{EM}}{P_{EM} + P_{ICE}} = \frac{62}{62 + 95} \sim 0.4 \tag{3.2}$$

The concept of the parallel hybrid-electric propulsion system for aeronautical application has been designed in Catia V5, as shown in Figure 3.2

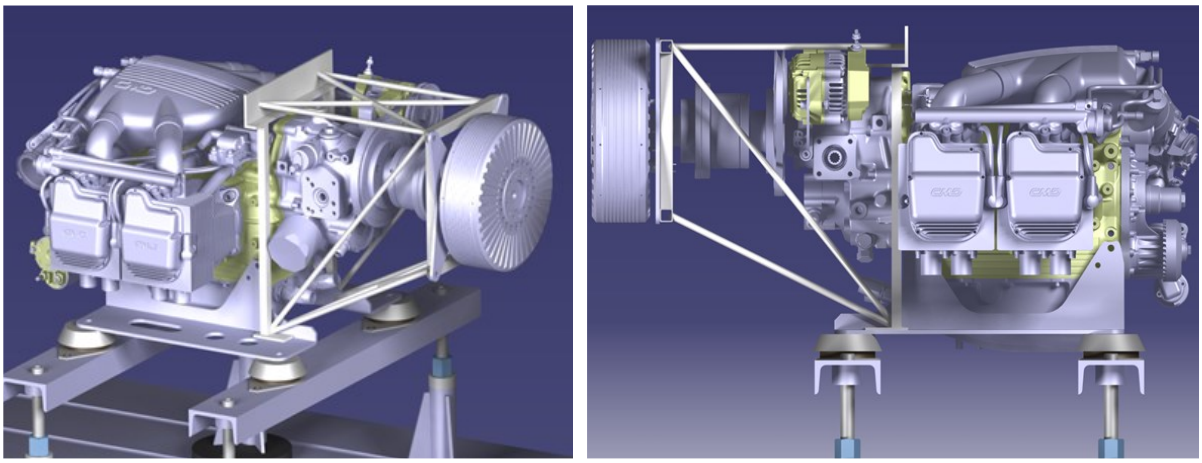

(a) (b)

Figure 3.2. HEPS prototype: (A) axonometric projection; (b) side projection.

The drawing in Figure 3.3 (b) shows the mechanical powertrain assembly. Starting from left the CMD 22 propeller shaft (in cyan) is connected to part number 1, consisting of a shaft inserted into a one-way clutch bearing (in green), subsequently connected to part number 2 consisting of adaptative coupling flange between the one-way clutch bearing to the flanged shaft with inner splines (FSI) and finally coupled to the EMRAX 268 through an extended shaft with outer splines (ESO) adopting six splines keys.

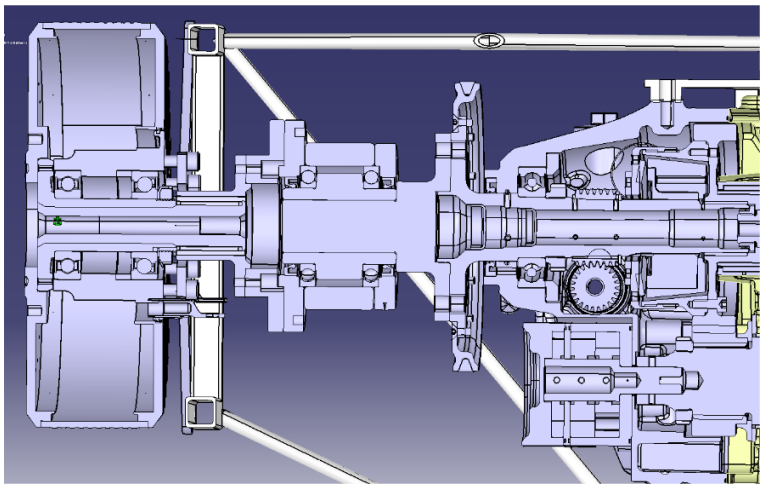

(a)

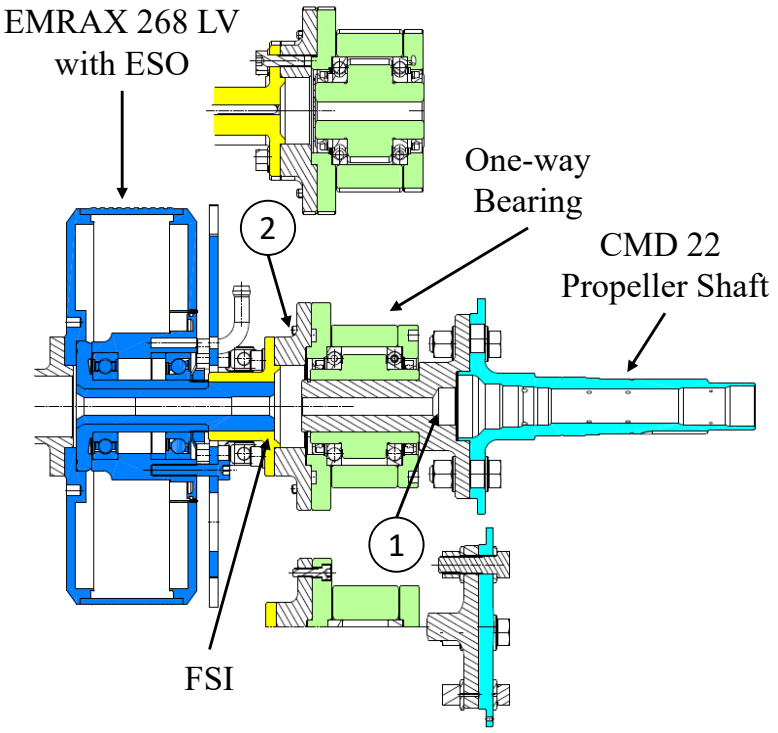

(b)

Figure 3.3. Mechanical assembly: (a) side section;(b) drawing 2D.

In addition, a piping structure has been designed to support the propeller shaft centreline and to fix the EMRAX 268 LV stator. The structure has three supports, two near the engine mounting in the front sides position and one support on top of the propeller case. A detail regarding the sizing and structural verification of some mechanical parts of the powertrain has been analyzed in Appendix A. Next, a brief description of the main components made of the studied HEPS prototype will be exposed.

Internal Combustion Engine – ICE

The ICE used in this work is a Spark Ignition (SI) naturally aspirated unit manufactured by the CMD Engine S.p.a. (a Loncin Company), developed for light and general aviation aircraft (specification in Figure 3.4) named CMD 22. The CMD 22 is an air-cooled, four-cylinder boxer engine with an integrated gearbox reduction of 2:1 for the propeller shaft. Its displacement is 2200 cm^3 [35]. This engine has an ignition system composed of two spark plugs for the cylinder and an indirect injection system with two injectors for each cylinder. All the operations are managed by an Electronic Control Unit (ECU). The engine control system is a standard speed-density with a nonlinear transient fuel film and barometric compensator. The power exerted by

the engine is about 95 kW (127 HP) @5500 rpm crankshaft speed (@2750 rpm propeller shaft) shown in Figure 3.5.

Technical specification	UoM	CMD 22
Bore	mm	100
Stroke	mm	70
Displacement	cm^3	2198
Compression ratio	-	9,7:1
Cylinder N°	-	4
Prop. drive ratio	-	1:2
Dry Weight m_{ICE}	kg	77,6
Weight/Power	kg/Hp	0,657
Max.Power (@5500rpm)	kW	95
Max.Torque(@5500rpm)	Nm	175

Figure 3.4. Internal combustion engine CMD 22: technical specifications [35].

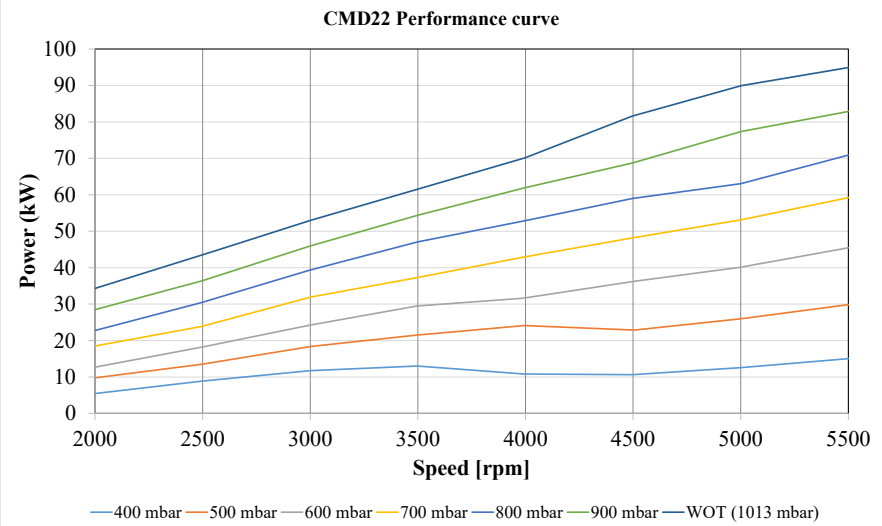

Figure 3.5.CMD 22 iso-power at different manifold air pressure load referred to the Crankshaft Speed[35].

Elelectric Machines – EM

The EM used in this work is the EMRAX 268 Low Voltage. This Motor is manufactured by the Electric Motor Roman AXial EMRAX d.o.o., developed and produced for the aerospace industry (all specifications are highlighted in Figure 3.6). The EMRAX 268 LV series is a permanent magnet synchronous machine (PMSM) with Axial flux, brushless, where the outer part is rotating. The best characteristics of EMRAX motors are respectively lightweight best-in-class power density (up to 10 kW/kg), high efficiency (up to 98%), high torque at low speed,

and reliability (developed and produced for the aerospace industry). Moreover, the EMRAX 268 LV is able to provide 107 kW of continuous power at 4500 rpm, with a maximum continuous torque of 250 Nm (green curve in Figure 3.7). Only for a few seconds, the EM can achieve a peak power of 200 kW and peak torque of 500 Nm (red curve in Figure 3.7) [36].

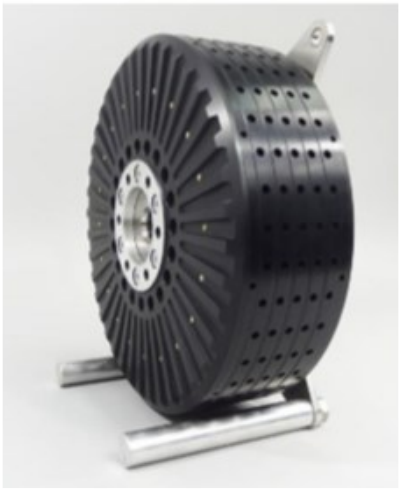

Technical specification	UoM	EMRAX 268 LV
Weight	kg	20
Diameter/Width	mm	268/91
Max. battery voltage	Vdc	250
Continuous Power	kW	107 CC
Peak Power	kW	200
Continuous Torque	Nm	250 CC
Peak Tower	Nm	500
Max. Speed	rpm	4500
Continuous Current	Arms	500
Peak Current	Arms	1000
Motor efficiency	%	92-98
N° pole pairs	-	10
Rotor Inertia	Kgm^2	0.0922
Wire connection	-	star
Induction Lq/Ld	µH	17/15.9
Magnetic flux - axial	Vs	0.0245
Specific load speed	rpm/1Vdc	18

Figure 3.6. PMSM EMRAX 268 LV: technical specifications [36].

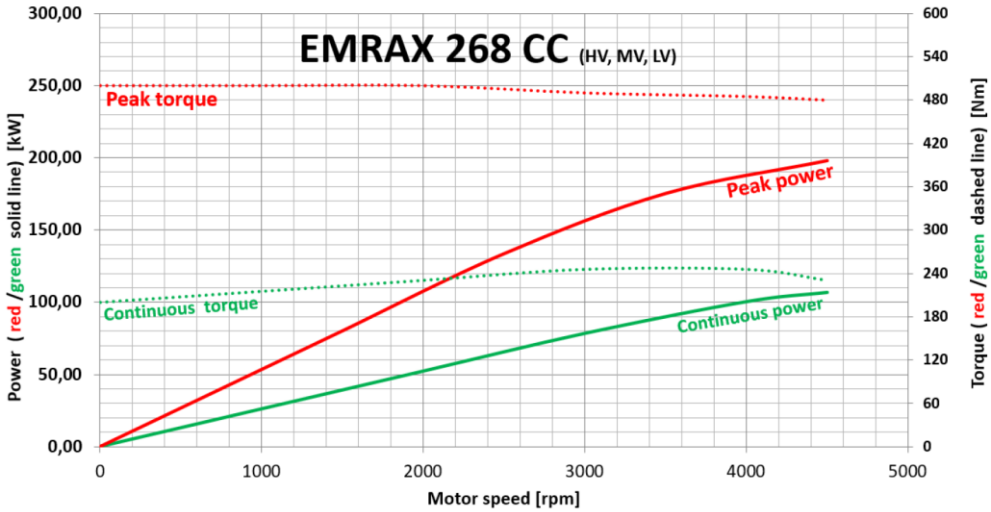

Figure 3.7. EMRAX 268 LV power and torque curves [36].

Power Converter & Control Display – DC/AC Inverter

The power converter DC/AC used in this work to drive the EM is a Global Vehicle Inverter (GVI-H650-0500S1-R00-G0000) HV series. This electric driver is a Voltage Source Inverter (VSI) manufactured by Parker, developed and produced for mobility and traction (all

specifications are highlighted in Figure 3.8). This GVI is also connected through CANbus J1939 to the control module IQAN-MD4-7-T1E2. The MD4 is a master control unit reprogrammable through IQAN Design Software, where the driver can easily control the GVI (and then the motors) and visualize the most important parameters (all specifications are highlighted in Figure 3.9) [37].

Technical specification	UoM	GVI-H650-0500S1
Nominal voltage	Vdc	650
Peak current	Arms	500
Peak Power	kVA	300
Operating temp. range	°C	-40 to 85
Communication	-	CAN J1939/OPEN
Feedback	-	Resolver
Control Type	-	Speed,Current,Torque
Output Current, 1 h	Arms	375
Battery Voltage Range	Vdc	100-750
Weight	kg	25

Figure 3.8. DC/AC Voltage source Inverter GVI-H650: technical specifications [37].

Technical specification	UoM	IQAN-MD4-T1E2
Power supply	Vdc	9-32
Temperature range	°C	-30 to 60
Communication	-	4xCAN
Communication	-	2xEthernet
Dicital Output	-	4
Display	-	7” touchscreen

Figure 3.9. IQAN-MD4-T1E2: technical specifications [37].

Resolver

The EM rpm signal is strictly necessary to control and monitor the electric machine. The GVI requires a revolution ω and position θ signals as input. The resolver sin/cos sensor type TS2620N1095E161 manufactured by the Tamagawa company has been chosen, and all the characteristics are shown in Figure 3.10 [38].

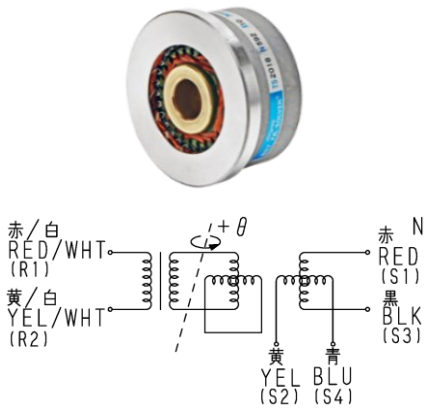

Technical specification	UoM	TS2620N1095E161
Input Voltage (V_{ex}),(ω_e)	Vrms	7 AC 10kHz
Input Current	mA	65
Phase shift	deg	+12° ±10%
Trasformation ratio (k)	-	0.4 ±10%
Input Impedance	Ω	120 ±10%
Output Impedance	Ω	480 ±10%
Rotor Inertia	Kgm^2	3x10^{-6}
Pole pair	-	5
Max. operating speed	rpm	10000

Figure 3.10. Resolver Tamagawa TS2620N1095E161: technical specifications and wiring [38].

As shown in Figure 3.11, in a software-based resolver-to-digital (RDC), when the rotor winding of resolver is excited with a high frequency voltage $V_{ex}^{R_1-R_2}$, the two spatially orthogonal windings on the stator will produce amplitude modulation signals which have sinusoidal $y_{sin}^{S_2-S_4}$ and cosinusoidal $y_{cos}^{S_1-S_3}$ envelopes with respect to shaft angle θ.

$$V_{ex}^{R_1-R_2} = V_{ex}\sin(\omega_e \cdot t) \tag{3.3}$$

$$y_{sin}^{S_2-S_4} = k \cdot V_{ex}^{R_1-R_2}\sin(5 \cdot \theta) \tag{3.4}$$

$$y_{cos}^{S_1-S_3} = k \cdot V_{ex}^{R_1-R_2}\cos(5 \cdot \theta) \tag{3.5}$$

where k is the transformation ratio of the resolver; V_{ex} and ω_e denote the amplitude and frequency of the excitation signal, respectively. Then the envelopes are obtained from detection. Finally, owing to the mathematical properties of trigonometric function, the angular position θ and velocity ω are calculated from envelopes by phase-locked loop, arctangent or other demodulation algorithms [39-40].

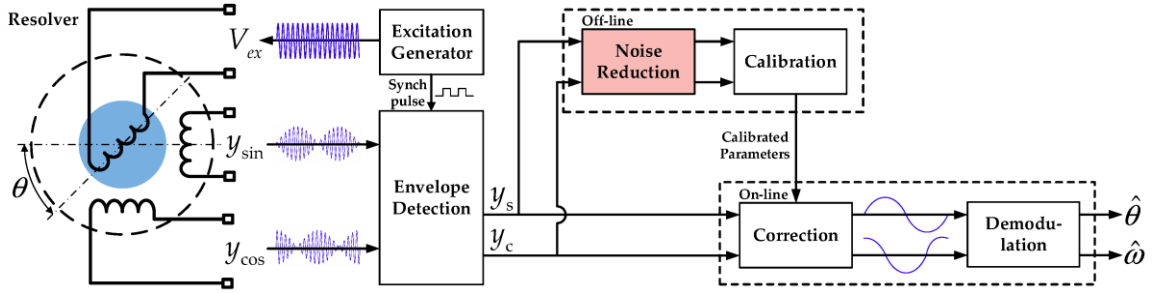

Figure 3.11. Schematic diagram of resolver and software-based RDC [36].

Bi-directional Power Converter – AC/DC Rectifier

The IT6018C-500-90 is a bi-directional programmable AC/DC power supply (Rectifier), which adopts the SiC-base technology, manufactured by the ITECH, developed and produced for automotive, renewable energy and testing (all specifications are highlighted in Figure 3.12) This module offers the functionality of two-quadrant operation shown in Figure 3.13. The regenerative capability ensures to put back of the energy onto the grid [41].

Technical specification	UoM	IT6018C-500-90
AC Input Voltage	Vac	198 to 264
AC Input Frequency	Hz	47 to 63
DC Output Voltage	Vdc	0 to 500
DC Output Current	A	-90 to 90
DC Output Power	kW	-18 to 18
Efficiency	%	92
Operating Temperature	°C	0 - 50
Weight	kg	40
Communication	-	USB, CAN, LAN
Internal resistance	Ω	~1

Figure 312. Bidirectional programmable AC/DC power supply IT6018C-500-90: technical specifications [31].

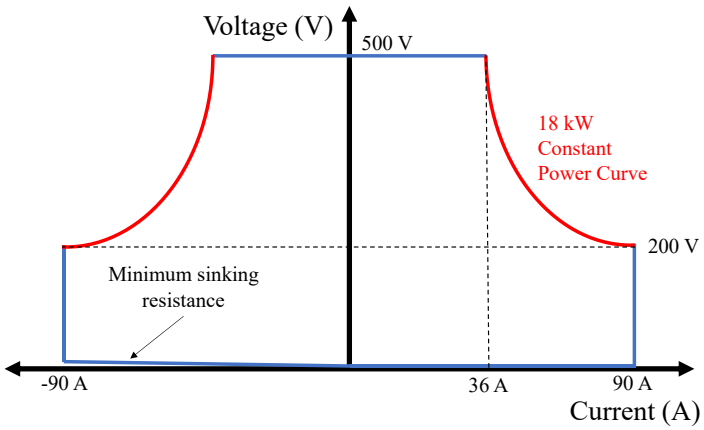

Figure 3.13. Auto ranging output of a 18 kW bi-directional power supply. Maximum voltage is 500 V and maximum current is ±90 A [41].

One-way bearing

An essential component of a parallel hybrid-electric propulsion system is the mechanical clutch. This component is able to combine the power of the ICE and EM. The one-way bearings are a cheaper, simpler, reliable, and lighter solution regarding the electromagnetic clutch or planetary

gearing. Furthermore, the one-way bearing is a good compromise choice for this prototype concept HEPS, guaranteeing compliance with the requirements. The one-way bearing used in this work is the GL 35 F2-D2. This component is manufactured by the C.T.S. (all specifications are highlighted in Figure 3.14) [42]. Regarding the structural check, only the ICE torque has been considered, while the EM torque is added downstream of the one-way bearing. Therefore, the permitted continuous transferable torque of 735 Nm is far from the ICE one 350 Nm. Moreover, another check is required about the outer and inner race limits (3000 and 1500 rpm respectively). For this purpose, the following considerations have been taken into account for each operational mode:

- *fuel-only*, in this case, ICE and EM are running at the same speed and the one-way bearing is clutched. The relative speed between the inner and outer ring race is equal to zero;
- *battery-only*, in this case, only the EM is running, and the ICE is off or idle speed. The maximum relative speed between the inner and outer ring race is equal to 2750 rpm ;
- *hybrid*, in this case, ICE and EM are running at the same speed the one-way bearing is clutched. The relative speed between the inner and outer ring race is equal to zero;
- *charging*, in this case, ICE and EM are running at the same speed, the one-way bearing is clutched. In particular, the EM would be running in reverse mode but it is constrained to the ICE rotational speed verse. The relative speed between the inner and outer ring race is equal to zero.

In conclusion, the most critical condition regards the *battery-only* mode, where the outer and inner ring relative velocity is near the structural limit.

Technical specification	UoM	GL 35 F2-D2
Internal shaft diameter	mm	35
External shaft diameter	mm	110
Axial thickness	mm	74
Inner race limit	rpm	1500
Outer race limit	rpm	3000
Cont. transferable torque	Nm	735
Max. transferable torque	Nm	1470
Weight	kg	4.5

Figure 3.14.One-way bearing GL 35 F2-D2: technical specifications [42].

Eddy-current brake & control

The eddy-current brake is the Schenck WS 260 with a maximum power of 260 kW at 10000 rpm shown in Figure 3.15 (a). The brake torque is measured through a load cell fixed at an

oscillating arm linked to the brake stator. All mechanical power is converted into thermal one (joule effect) subtracted through a closed-loop cooling circuit employing water as a heat carrier. By means of the MP2030 control unit, as shown in Figure 3.15 (b), the eddy-current brake can be controlled, where the motor RPM and torque signals are inputs to the system and used for feedback control. There are three possible "*brake control modes*" respectively:

- $N = k$ the brake speed is fixed.
- $M = k$ the brake torque is fixed.
- Mn^2 is typical square load seams to the marine and aeronautical propellers where the braking torque is proportional to the current. The following equation link the eddy-current to the torque shape.

$$I = k_v \cdot n + k_{Mn^2} \cdot n^2 \tag{3.6}$$

Where I is the brake current, n is the speed in revolution per minute, k_v and k_{Mn^2} are two setting coefficients.

(a) (b)

Figure 3.15. (a) Eddy current brake Schenck WS 260; (b) MP2030 Eddy current control.

3.1.2. HW&SW design: data acquisition and remote control systems

An experimental activity has been carried out on the HEPS prototype to evaluate its functionality and performance. The tests have been conducted at the Hybrid engine test room of the Department of Industrial Engineering of the University of Naples Federico II.
For this purpose, a dedicated data acquisition system (DaQ) has been designed starting from National Instruments Hardware (C-Rio and Field Point) modules and LabView development Software. Linked to the principal DAS, other subsystems based on proprietaries Hardware/Software are connected, i.e., the Parker Inverter control (through SW IQAN Design ah HW MD4), the CMD 22's Electronic Control Unit (ECU) parameters (through SW Tuner Studio), and bi-directional ITECH power supply control (through SW IT900). Figure 3.16 highlights the communication connection between boards and the spatial installation in the Test Room and Control Room..

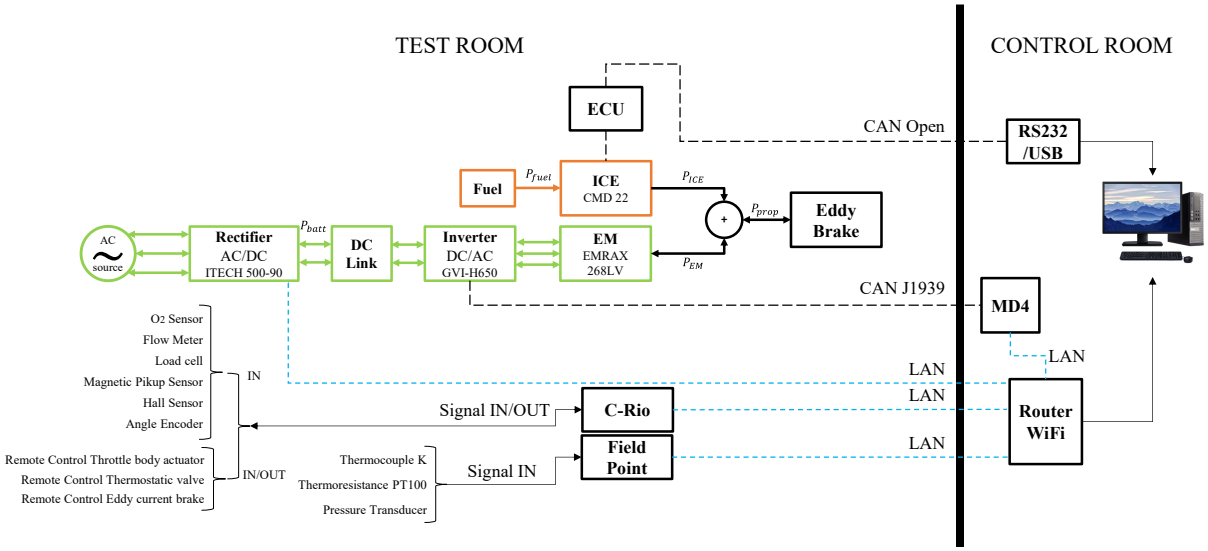

Figure 3.16. The data acquisition and control systems connection.

The data acquisition and control systems consist of two National Instruments boards, one NI Field Point 1808 and one NI Compact Rio 9024, used as analog to digital converters managing sensors and actuators. Moreover, the LabView software has been used to handle, save, and control, adopting a friendly user guide interface, all data sent to the NI boards. The NI Field Point 1808 handles slow signals through different acquisition modules, such as the current signals cFP-AI-111, thermocouple cFP-TC-120, and thermoresistance cFP-RTD-122 signals. Differently, the NI C-Rio 9024 is able to acquire and control signals at high frequencies. In fact,

the NI C-Rio can be programmable in three layers based on a Field Programmable Gate Array (FPGA), Real-Time (RT), and PC running. Therefore, the C-Rio board has a dedicated microprocessor and an Operative System (OS). These characteristics make the C-Rio board work in a stand-alone, where uploading a program to the flash memory can be managed without the PC connection. The FPGA handles the high-frequency signals and transmits the processed data to the RT layer. The RT programmable layer directly handles the low-frequency signals (< 100 Hz). Moreover, the RT sends all the processed data to the computer through the LAN Ethernet protocol. Figure 3.17 illustrates a scheme of the acquisition system [43].

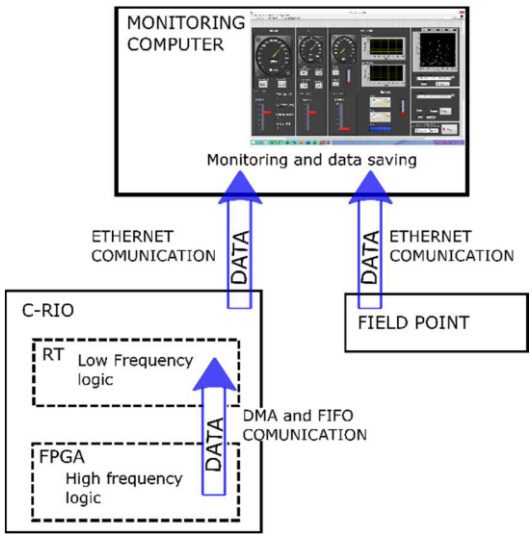

Figure 3.17. Scheme of the data acquisition system (DAS): data flow.

The main modules used in the C-Rio board are the analog input (AI) NI 9207 and analog output (AO) NI 9264 voltage signals module, the variable reluctance sensor signal NI 9752, the O_2 probe sensor using NI 9757 module, the Controller Area Network (CAN) bus protocol signal NI 9862 and a digital input/output (DIO) NI 9201. Both boards communicate to the PC through a LAN Ethernet protocol network. The acquisition and control software for monitoring the engine test rig running on the monitoring computer provides the Graphic User Interface (GUI) and the data-saving functionality on the ASCII file Figure. The automatic data acquisition is controlled and executed by a LabView-based graphical interface (GUI) Figure 3.18.

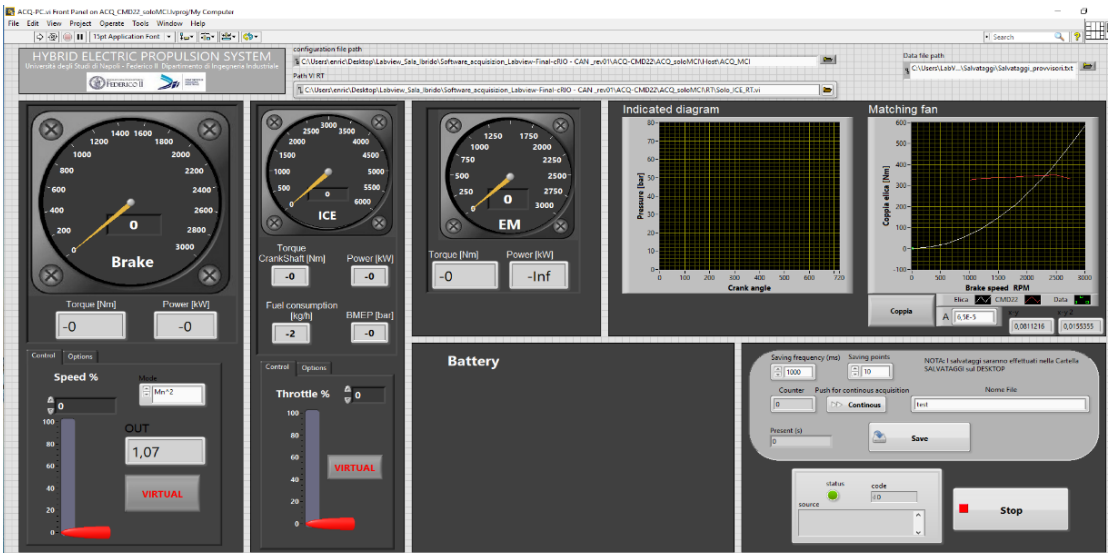

(a)

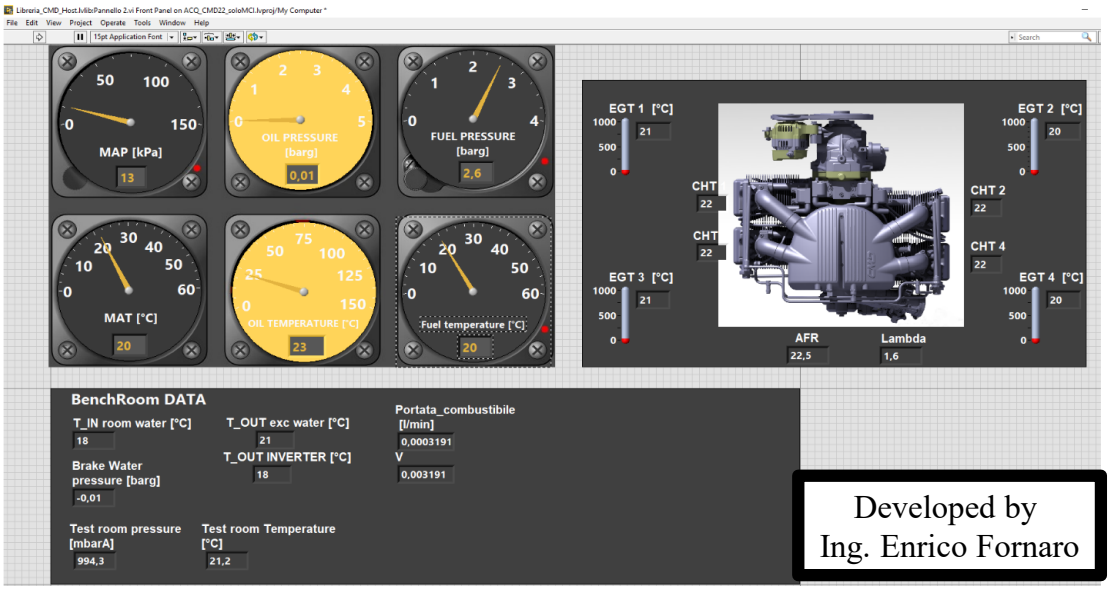

(b)

Figure 3.18. LabView-based graphical interface GUI.

The LabView code (Figure 3.18) has been designed as a state machine. The state machine manages the initialization process, the GUI interface, and the data saving. The state machine monitoring frequency is about 10 Hz, but the saving process frequency can be lower (i.e., one set of samples per second) without affecting the overall speed of the state machine loop.

Also, LabView software provides some data processing functionalities (such as unit scaling and alarms) and calibration utilities (for the linear actuator and the brake remote controls). The calibration constants are saved on request in an external initialization file.

Moreover, there are two different options for the saving process: continuous and fixed samples. In the first case, the program saves the data continuously until the operator stops it. In the second one, the number of samples is set beforehand, and the program complete the saving process automatically. The program consists also of other parallel loops. These loops manage the processing of time-critical data (i.e., indicated diagrams) and their saving, while buffered queues provide lossless communication through different cycles. Figure 3.18 (a) and Figure 3.18 (b) shows the software GUI [44]. More details about the employed sensors are reported in Table 3.2.

Table 3.2. Main features of sensors and instruments of the monitoring and control systems.

Quantity	Sensor/Instrument	Range	Accuracy
Intake manifold air temperature (MAT)	PT100	-80 ÷ 250 [°C]	± 0.5 °C
Exhaust gas temperature (EGT)	K-type thermocouples	-270 ÷ 1260 [°C]	± 1.1 °C or 0.4 %
Cylinder head temperature (CHT)	T-type thermocouples	-184 ÷ 370 [°C]	± 1.1 °C or 0.4 %
Oil temperature	T-type thermocouples	-184 ÷ 370 [°C]	± 1.1 °C or 0.4 %
Manifold air pressure (MAP)	Piezoresistive absolute	0 ÷ 15 [PSI]	< 1% FS
Fuel pressure	PTX 1000	0 ÷ 5 [barg]	± 0.25% FS
Fuel temperature	T-type thermocouples	-184 ÷ 370 [°C]	± 1.1 °C or 0.4 %
Fuel flow meter	Fuel balance	0 ÷ 125 [kg/h]	< 0.12% FS
Intake air flow	Flow meter	15 ÷ 400 [m^3/h]	± 1.0% of Rate
O_2 Sensor	Wide-band UEGO	0.65 ÷ 15.99	± 0.1% FS
Torque	Load cell	-5000 ÷ 5000 [N]	± 0.05% FS
Angular velocity rpm	Magnetic Pickup	Threshold 50 rpm	

The throttle valve is controlled through a linear actuator with position feedback control. The actuator pulls or releases the throttle wire allowing a repeatable and automatic throttle management. The needed actuator stroke is 30 millimetres, so the time to completely open the throttle is about 2 seconds. A dedicated microcontroller Pololu Jrk 21v3 handles the position control, PID logic and Pulse Width Modulation (PWM) signal generation. The desired setpoint is remotely given to the microcontroller as a [0, 5] V signal [44] [45]. The Figure 3.19 shows the throttle valve control system.

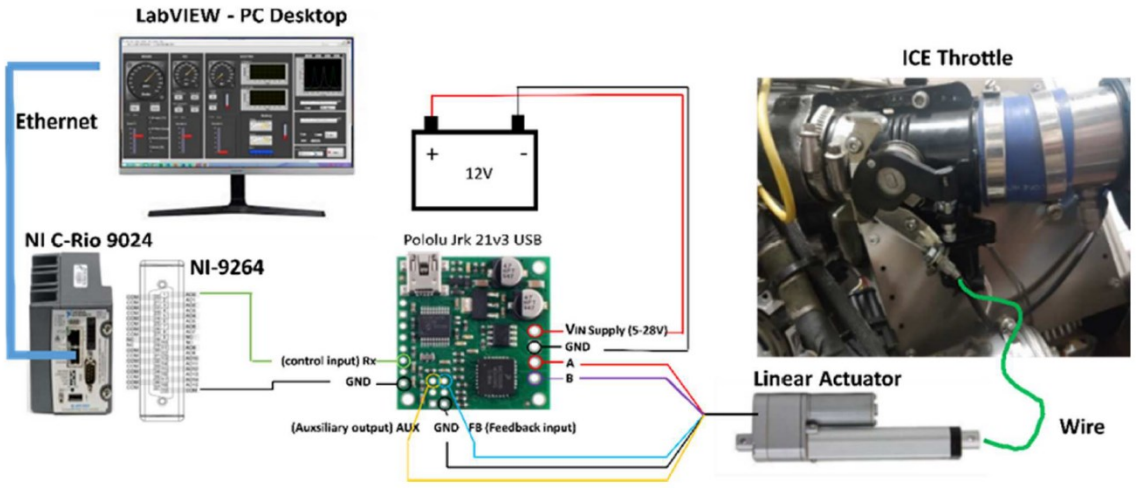

Figure 3.19. Remote Throttle Body control system [44].

The reprogrammable ECU is connected to the PC through Serial Converter DB-9 (RS-232) to USB whit chipset Prolifico shows in Figure 3.20. The communication protocol is based on CAN Open standard.

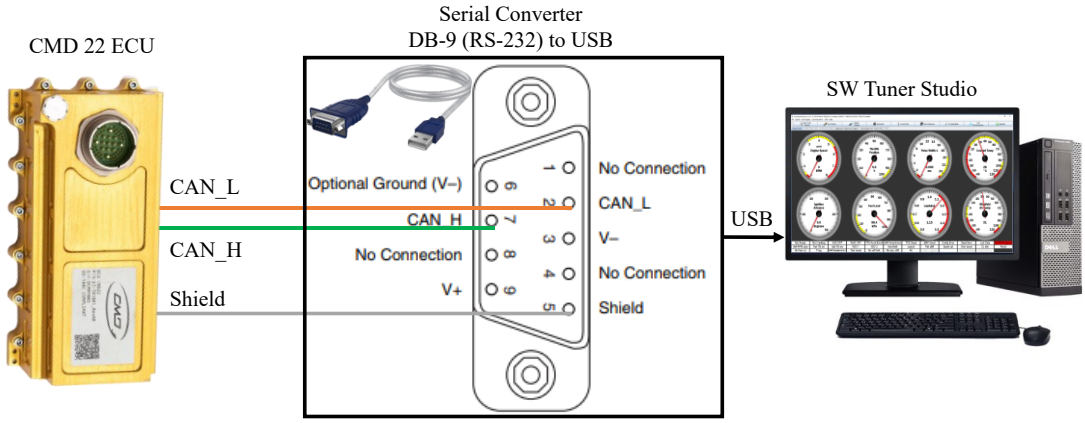

Figure 3.20. ECU to PC CAN Open communication through a serial converter.

The ICE can be calibrated through Tuner Studio software, and this tool can also save all ECU data in ASCII format with 50 Hz frequencies [46].

The electronic driver of the GVI-H650 is connected, through a C1 connector, to different devices, as shown in Figure 3.20 [47], such as:

- Temperature sensor (thermoresistance) inside the EMRAX 268 LV connected to C1:2 (sensor 1 GND) and C1:3 (sensor signal);

- Resolver SIN/COS feedback speed and angular position sensor connected to excitation input voltage C1:6 (+), C1:9 (-) outputs signal COSINE C1:7 (+) and C1:8 (-) and outputs signal SINE C1:10 (+) and C1:11 (-);
- MD4 touchscreen display thought the supply connection C1:38 (GND), C1:39 (24Vdc) and C1:35 (Key-On) and also the communication connection adopting CAN J1939 standard C1:22 (High) and C1:25 (Low). The MD4 touchscreen can be configured through Parker property SW named IQAN Design, connected to the PC using a property C3 LAN cable. Moreover, IQAN Design is able to datalogger useful during the test activities;
- The GVI inverter driver must be configurated only through CAN Open, a connection using pins C1:29 (Low) and C1:30 (High) using the Parker property SW named ConfigTool. This tool can configure all parameters of the coupled electric machine. Moreover, the CAN bus is connected to the Kvaser Hs v2 device to convert the CAN Open signal input to a serial USB signal.

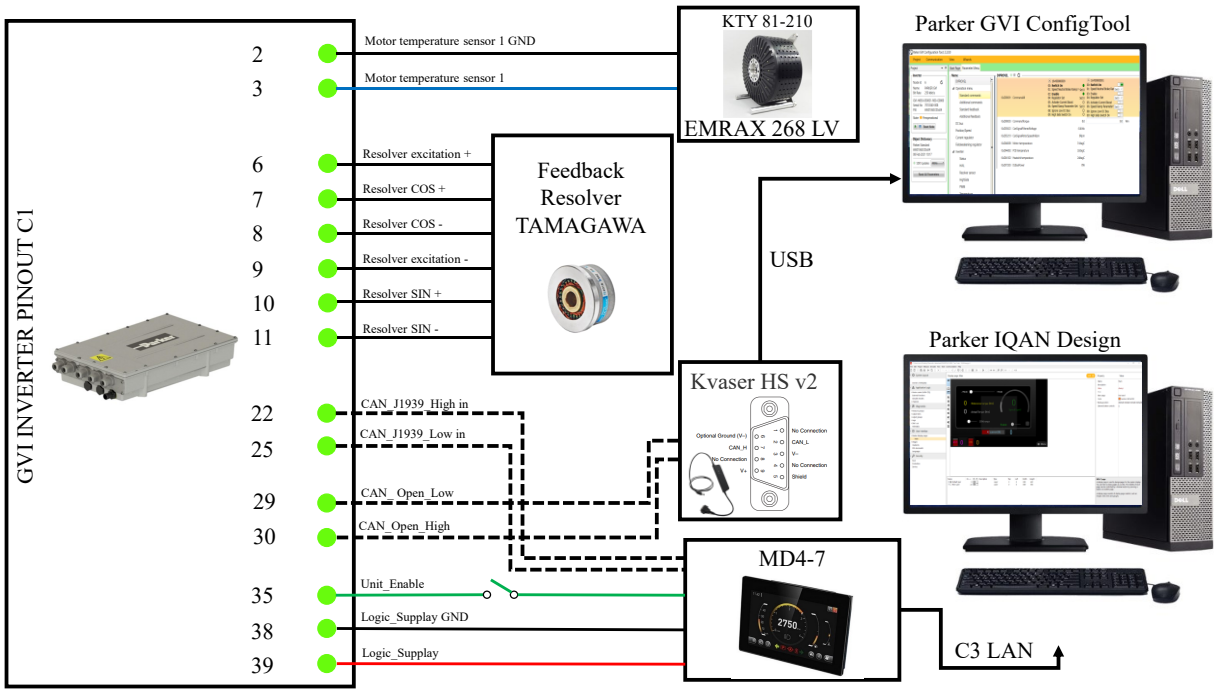

Figure 3.21. GVI-H650 connection to devices and Software.

Finally, the bi-directional AC/DC power supply (ITECH IT6018C-500-90) can be remotely controlled using a property SW IT900. The AC/DC rectifier is connected to the PC using an Ethernet LAN cable, shown in Figure 3.22. Through the SW IT900, the AC/DC can be

configured, such as a pure power supply or battery emulator (in this case, the battery capacity must be set). Moreover, IT900 is able to datalogger useful during the test activities [48].

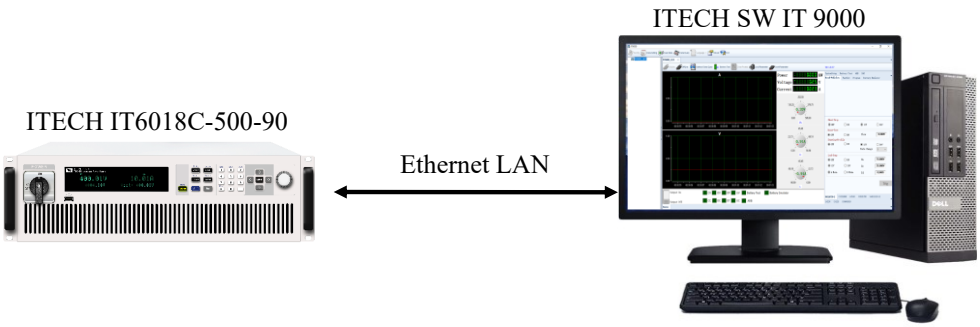

Figure 3.22. ITECH remote control connection.

In conclusion, the HEPS prototype is assembled in the Test Room for experimental activities (Figure 3.23), and Figure 3.24 shows the Data Acquisition setup in the Control Room.

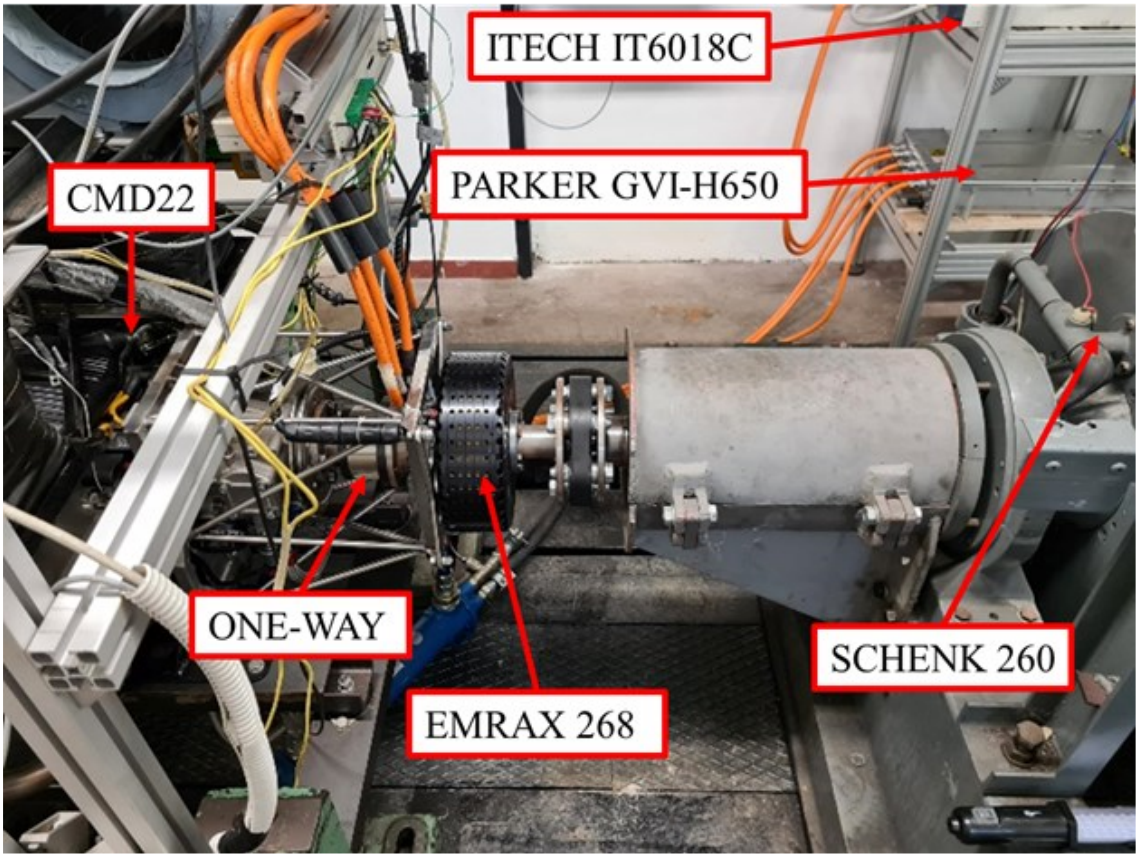

Figure 3.23. Experimental setup of HEPS - Test Room.

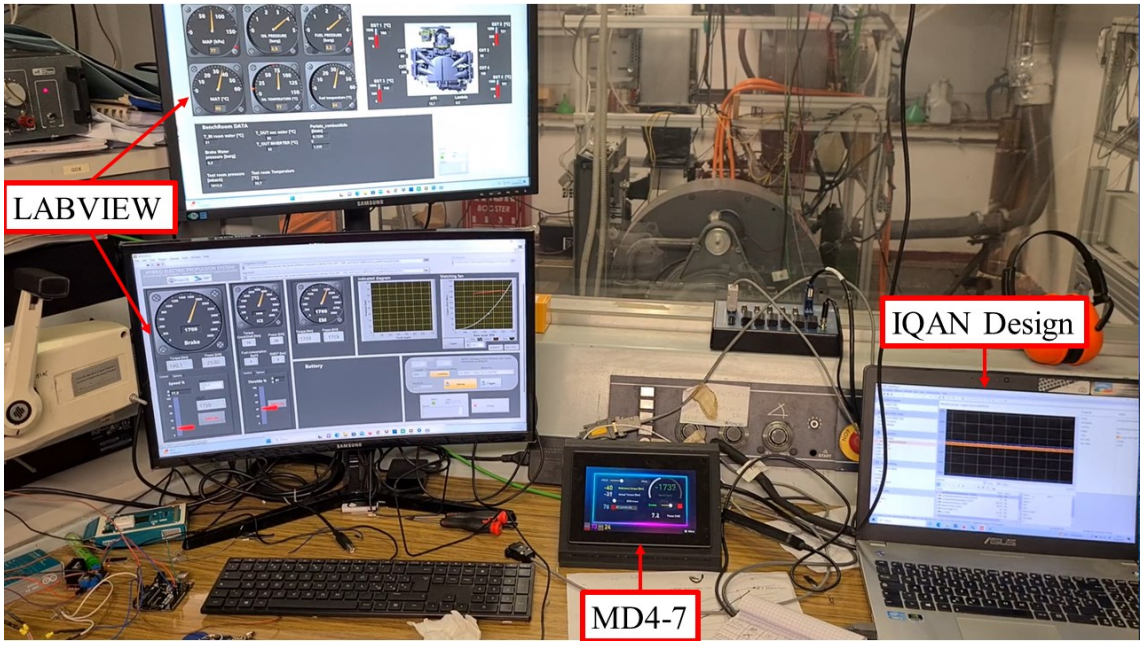

Figure 3.24. Data acquisition setup of HEPS - Control Room.

3.2. Testing Activities and Results

This section has discussed the preliminary experimental activities conducted on the hybrid electric propulsion system HEPS. The principal purpose of the tests is to demonstrate the correct sizing and, thus, the proper operation of the hybrid prototype in the different modes of operation: *fuel-only*, *battery-only*, *hybrid*, and *charging*. The ITECH IT6018C-500-90 bi-directional power supply was critical to the execution of the tests because it allowed the tests to be released from the charge and discharge cycles that the battery would necessarily require. In addition, the bi-directional power supply facilitated the repeatability of the tests without incurring issues related to voltage oscillation that a battery real would have entailed. Unfortunately, the limited power of the bi-directional power supply, just 18 kW, did not allow some tests to push to higher power points. Certainly, the proposed methodology and the operation of HEPS have been demonstrated. Several experimental tests were conducted under different operating conditions to compare the results with the design requirements and to characterize the hybrid propulsion system in terms of performance and efficiency. At each operating point, the following measures are performed:

- Brake average speed n_{brake}, in rpm;
- Brake average torque T_{brake}, in Nm;
- EM average speed n_{EM}, in rpm;
- EM average torque T_{EM};
- ICE average speed n_{ICE}, in rpm;
- ICE average speed T_{ICE}, in Nm;
- ICE fuel mass flow $\dot{m}_f$, in kg/s;
- Battery DC-Link average voltage V_{dc}, in V;
- Battery DC-Link average current I_{dc}, in A;

Figure 3.25 shows the block scheme of the HEPS, highlighting in detail the power flux and efficiencies of the various subsystems. To measure the torque, the shaft of the HEPS propeller was coupled to an eddy-current dynamometer. The dynamometer has an oscillating housing mounted on a load cell to measure the T_{brake}. and a variable reluctance electromagnetic sensor coupled to a 60-tooth wheel has been used to measure the speed of the n_{brake} propeller shaft.

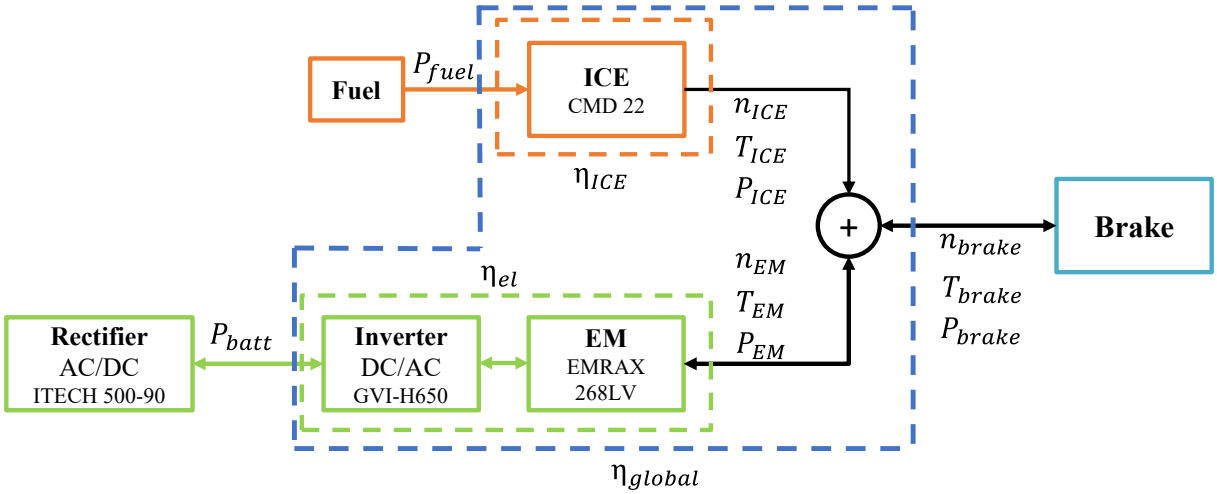

Figure 3.25. Schematization of the power and torque flux, efficiency, and electrical quantities in the HEPS equipped for testing activities.

The internal combustion engine is electronically controlled by a property ECU. Moreover, the crankshaft speed is measured by a Hall sensor connected to a magnetic wheel coupled to the rear of the crankshaft. The speed and torque of the EM are monitored by a dedicated touchscreen controller MD4. In addition, the GVI driver is set to a closed-loop torque mode. The electrical measurements, such as DC-link current and voltage, are recorded by the ITECH IT900 software. The ICE and EM powers contribution has been evaluated as follows:

$$P_{batt} = V_{dc} \cdot I_{dc} \tag{3.7}$$

$$P_{EM} = T_{EM} \cdot \omega_{EM} = P_{batt} \cdot \eta_{el} = V_{dc} \cdot I_{dc} \cdot \eta_{el} \tag{3.8}$$

$$P_{fuel} = \dot{m}_f \cdot H_i \tag{3.9}$$

$$P_{ICE} = T_{ICE} \cdot \omega_{ICE} = P_{fuel} \cdot \eta_{ICE} = \dot{m}_f \cdot H_i \cdot \eta_{ICE} \tag{3.10}$$

where T_{EM}, T_{ICE} and ω_{EM}, ω_{ICE} are respectively the motor torque (Nm) and the speeds in (rad/s), V_{dc} is the DC battery storage voltage, I_{dc} is the DC battery current sent to the EM controller device, η_{el} is the global EM and inverter efficiency, $\dot{m}_f$ is the mass fuel flow to supply the ICE, H_i is the fuel low heating value and η_{ICE} is the global ICE efficiency. By product of this quantity T_{brake} and n_{brake}, it is possible to evaluate the useful mechanical power to the propeller shaft through the well-known Equation (3.1) and substituting the motors power contributions Equations (3.8 and 3.10) is obtained:

$$P_{brake} = T_{brake} \cdot \omega_{brake} = P_{ICE} + P_{EM} = \dot{m}_f \cdot H_i \cdot \eta_{ICE} + V_{dc} \cdot I_{dc} \cdot \eta_{el} \quad (3.11)$$

where $\omega_{brake} = n_{brake} \cdot \frac{2\pi}{60}$ is the brake speed in (rad/s). Moreover, the global HEPS efficiency could be evaluated as follow:

$$\eta_{global} = \frac{P_{brake}}{\dot{m}_f \cdot H_i + V_{dc} \cdot I_{dc}} \quad (3.12)$$

Preliminary tests have been conducted in electric "*battery-only*" and ICE "*fuel-only*" modes. Next, a propeller brake load has been simulated through the eddy-current brake control system, where three operating CMD22 engine mission points have been identified, respectively: Take-off, Maximum continuous power, and 75% Maximum continuous power. The HEPS capabilities have been evaluated in these operating points, where the EM works in both motor and generator modes. Finally, a short flight mission was simulated, including "*hybrid"* and "*charging"* phases, where the bi-directional power supply has been configured as a battery emulator.

3.2.1. Electrical Machine characterisation

In this test, an investigation of the electrical efficiency of the coupling EM and GVI inverter has been carried out. In particular, a comparison between the measured efficiencies and the values provided in the EMRAX 268 datasheet has been made.

The electrical efficiency has been calculated in an indirect way, starting from electrical measures of current, and voltage, and mechanical measures of torque and speed. The tests have been carried out at different speeds and torque. In particular, the speed range has been selected of 250 to 2750 rpm in increments of 250 rpm. Moreover, the torque value has been changed between 10 and 150 Nm. In this test, the bidirectional power supply has been set to a voltage of 250 V, with the current operating range spanning from -80 A to +80 A.

Due to the limited power of the bi-directional converter ITECH (only 18 kW), some tests at high speed and torque haven't been performed.

All the tests have been performed adopting a fixed speed controller ($N = k$), maintaining the Schenck speed at a constant rotational value. Moreover, the desired EM torque has been set through the MD4 touchscreen interface connected to the Parker Inverter via the CAN bus J1939

protocol. Figure 3.26 (a) illustrates the mechanical torque of the electric machine (T_{brake}) across the 250 to 2750 rpm range, while Figure 3.26 (b) displays the DC-Link power curves (P_{batt}) for electrical power evaluation, calculated using Equation (3.7).

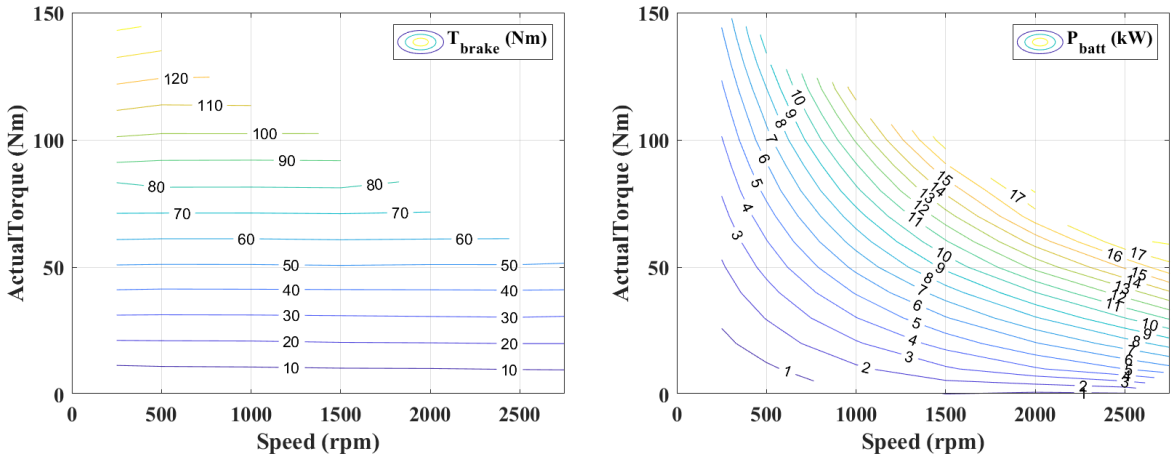

(a) (b)

Figure 3.26. Electrical Machine characterisation: (a) Iso-Torque mechanical (T_{brake});(b) Iso-Power electrical (P_{batt}).

The following test can be considered as $T_{brake} = T_{EM}$ and $n_{brake} = n_{EM}$, which means that the mechanical power calculated at the brake coincides with the mechanical power generated by the EM. Substituting the Equation (3.8) into Equation (3.11) and setting $P_{ICE} = 0$ to zero. Therefore, the electrical efficiency has been calculated through the following relationship:

$$\eta_{el} = \frac{P_{brake}}{P_{batt}} \tag{3.13}$$

Comparing the experimental results of the electrical efficiency (highlighted in dashed red box) with the datasheet values of the EMRAX 268 motor, as shown in Figure 3.27, can be observed: concerning the 86% isoline a matching between the two sets of data (experimental and datasheet) for higher rotational speeds around 2500 to 2000 rpm; for lower rotational speeds ranging from 500 to 1500 rpm, the difference consistently increases as the rotational speed decreases.

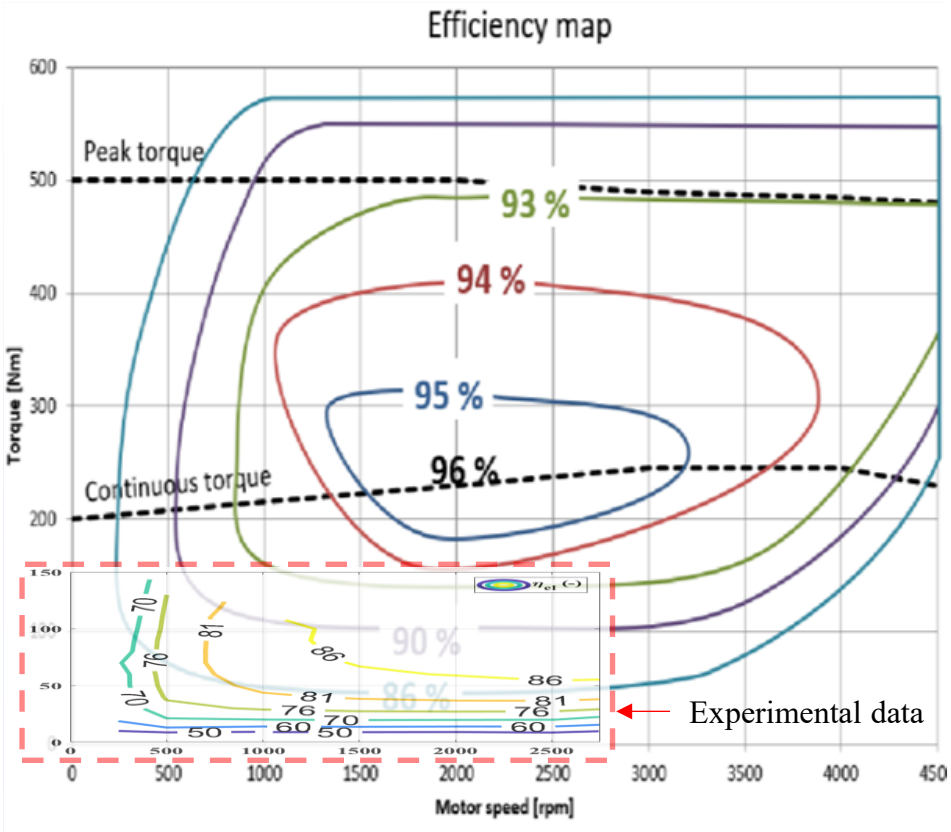

Figure 3.27. EMRAX 268 efficiency map [36]. In dashed red transparency box experimentally results of Iso-efficiency (η_{el}).

This difference could be ascribed to various factors:

a) *Magnetic Polarization* – In a Permanent Magnet Synchronous Motor (PMSM), efficiency is conditioned by the polarization of permanent magnets and their alignment with the motor's windings. At lower speeds, the magnetic field might not be fully aligned with the windings, leading to losses in magnetic flux and reducing the efficiency.

b) *Motor Control* – The control of a PMSM is often optimized for a definite speed range. Generally, the inverter has different control strategies that can changed at low speeds, which may not be as efficient as those used at higher speeds.

c) *Overall Efficiency* – The experimental efficiency data pertains to the combination of the inverter and the electric machine. The datasheet value only refers to the electric machine itself.

d) *Cooling system* – In the conducted tests, the electric machine was cooled using only air, without the water cooled. The EMRAX declared to use both cooling systems.

These factors can contribute to the observed differences in efficiency between the experimental results and the datasheet values for the EMRAX 268 motor.

3.2.2. Internal Combustion Engine characterization

The internal combustion engine is mechanically coupled to the electric machine via a one-way bearing. Therefore, when the ICE is running, the EM is also engaged to the propeller shaft and is placed to rotate. Consequently, in the "*fuel-only*" mode, the power is generated by the internal combustion engine, and, at the same time, the electric machine remains connected to the driveline placed in rotation. In other words, the electric machine behaves as a flywheel.
Through this test, it became possible to evaluate the performance of the ICE and its efficiency (η_{ICE}) when coupled with the electric machine.
Generally, in a HEPS, the motors can be designed to operate in different modes depending on driving needs and the hybrid system type. The two main modes are:

- *Full-Time*: In this mode, one or more motors, including the internal combustion engine (ICE) and the electric motor (EM), are active and contribute to propulsion continuously. This case is typical of light hybrid systems, where the electric motor can assist the ICE in critical situations such as acceleration or low-speed city driving. In plug-in hybrid systems (PHEVs), the electric motor can be continuously active when using electric energy from the battery.
- *On-Demand*: In this mode, the electric motor is activated only when needed, such as during acceleration, low-speed driving, or in heavy traffic conditions. This approach aims to maximize efficiency and reduce fuel consumption since the electric motor can work when it's more efficient than the internal combustion engine.

These modes allow hybrid propulsion systems to optimize their operation based on driving conditions, resulting in improved fuel efficiency and reduced emissions.
The *Full-Time* operating mode generally ensures better drivability and driving safety due to the quicker assistance provided by the electric motors. It also allows for enhanced regenerative capabilities when driving conditions require it.
On the other hand, the *On-Demand* mode requires a more sophisticated control strategy if compared to the former since the activation and deactivation of the motors must be optimal to minimize the drive lag. Simultaneously, it can prove to be more efficient as the electric motor is only engaged when advantageous to do so.

For this purpose, two tests have been performed in the "*fuel-only*" mode (only ICE) at wide open throttle (WOT) conditions. In particular, the first one sees the Inverter GVI power off, and the EM is not enabled to work (the pin C1:35 is open). In the second configuration, the Inverter GVI power is on, and the EM is enabled to work (the pin C1:35 is closed).

Moreover, the tests has been carried on at the same propeller speed in the range 1200÷2750 rpm fixing the eddy-current control at $N = k$ mode.

The engine CMD22 performances in terms of torque and power have been plotted in Figure 3.28 for both GVI Inverter configurations, also called *enable* and *no-enable*. Moreover, when the GVI is enabled, the required EM torque is set to zero 0 Nm.

As shown in Figure 3.29, the experimental tests have been carried out under the same conditions concerning the intake and exhaust gases, including the stoichiometric air condition and the Air Fuel Ratio (AFR) in Figure 3.29 (a), as well as the engine's air intake conditions, specifically Manifold Air Pressure (MAP) and Manifold Air Temperature (MAT) in Figure 3.29 (b).

The experimental results confirm the CMD22 performances at WOT in all speed ranges, but there are some differences between *enable* Vs *no-enable* tests. In particular, in the no-enable GVI configuration, the ICE power performance is generally lower with respect to the same test repeated for the GVI enabled configuration with a maximum percentage difference of 2.7%.

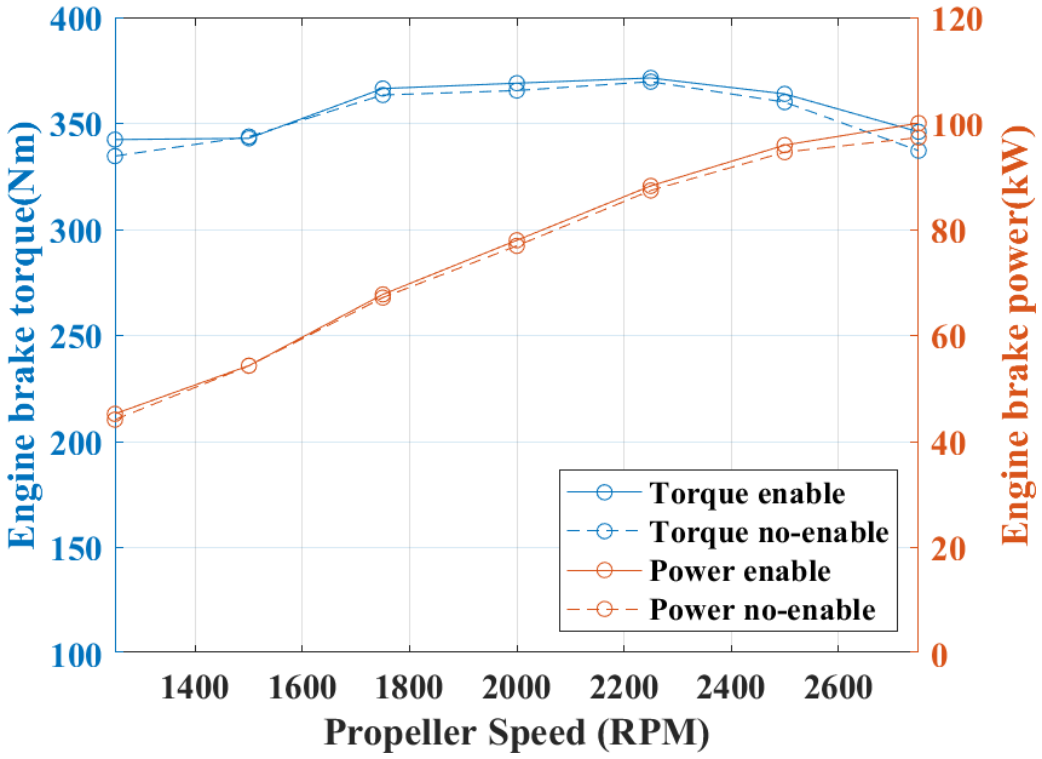

Figure 3.28. CMD22 Torque and Power at WOT with enable and no-enable Inverter GVI.

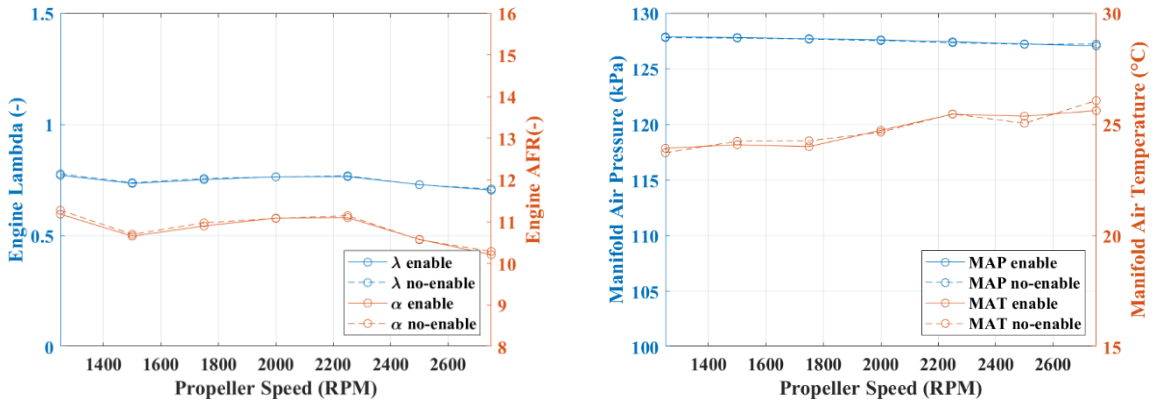

(a) (b)

Figure 3.29. CMD22 parameters at WOT with enable and no-enable Inverter GVI: (a) lambda and AFR; (b) MAP and MAT.

The power difference observed between both configurations is attributed to the uncontrolled rotation of the electric machine in *no-enable* condition, resulting in the accumulation of losses related to hysteresis, eddy-current, and additional losses, each highly non-linear. These combined losses are referred to as "*free run losses*" [49]. They oppose the rotation of the ICE, offering minimal mechanical resistance, which collectively translates to lower useful shaft power.

Figure 3.30 shows the experimental mechanical power difference between the *enable* and *no-enable* configurations (blue curve) and the "*free run losses*" declared on the datasheet by EMRAX d.o.o. (red curve). The trend is increasing with the rotational speed in both cases.

The greater availability of mechanical power in the enabled configuration is needed to active the GVI inverter, which spends a portion of electrical power to control the electric machine EM, ensuring the torque value set through the MD4 interface is equal to 0 Nm and balancing the "*free run losses*". Therefore, a current demand, as shown in Figure 3.31 (a), and subsequently, power demand from the DC-Link (from the bi-directional power supply), as depicted in Figure 3.31 (b).

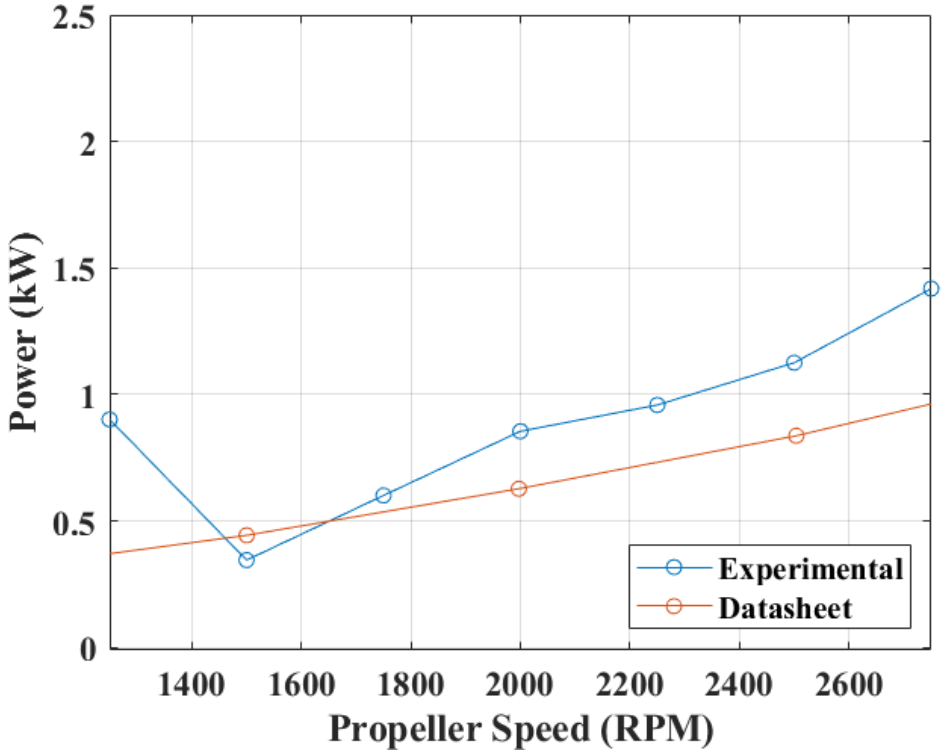

Figure 3.30. Experimental Vs Datasheet mechanical "*free run losses*".

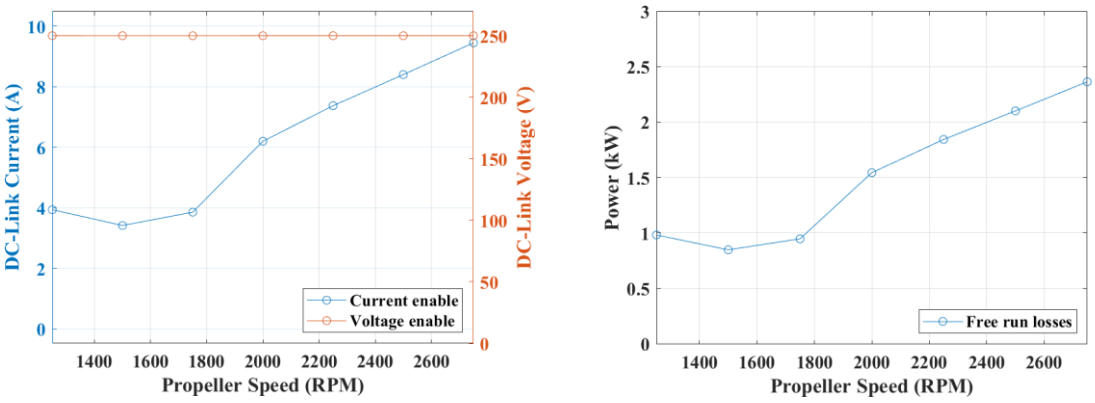

(a) (b)

Figure 3.31. (a) DC-Link Current and Voltage (in *enable* condition);
(b) DC-Link Power.

In future tests, the proposed hybrid electric propulsion system will be considered to work in enabled conditions. Therefore, in all upcoming tests, the GVI Inverter is always enabled and ready to control the EM (such as a *Full-time* configuration).

Subsequently, tests have been conducted to experimentally define the Brake Specific Fuel Consumption (BSFC) map (g/kWh) of the CMD22 engine (Figure 3.32). The tests have been performed at steady-state points, and the Schenck brake control has been sedded in N=k mode.

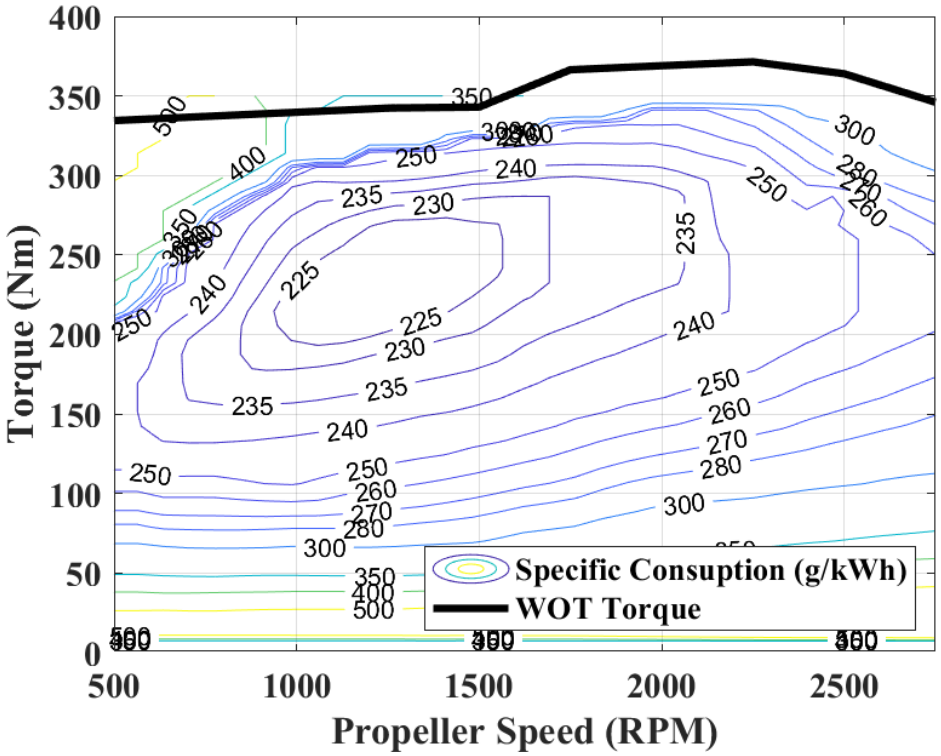

Figure 3.32. CMD 22 Brake specific fuel consumption (BSFC) (g/kWh).

3.2.3. Evaluation of Hybrid operational mode

In this test, the *hybrid* operating modes have been evaluated with the electric machine functioning as both a Motor and a Generator. The tests have been conducted only for the operating mission points (these points represent the aircraft operational range where the propulsion system will be in use for a substantial portion of its lifespan), specifically: Take-off, Maximum Continuous Power, and 75% of Maximum Continuous Power.

These points have been identified on a load curve similar to a propeller simulated through the eddy-current brake using the control mode $Mn^2 = k$, where the braking torque applied by the Schenck brake is proportional to the current, and this current is related to the square of the rotational speed, according to the following relationship:

$$I = k_v \cdot n + k_{Mn^2} \cdot n^2 \tag{3.14}$$

where I is the brake current, n is the speed in revolution per minute, k_v and k_{Mn^2} are two setting coefficients. The propeller chosen as representative for this class of engines is the MTV-6-D/170-112 manufactured by the MT-Propeller company, with a diameter $D = 1{,}7\ m$ and variable pitch.

Through the propeller Momentum Theory [50] application and using the McCormick coefficients [51] of power c_p and torque c_q, the propeller performance curve at different aircraft velocities v can be obtained in all speed ranges. First approximation the aircraft velocity is set equal to economy cruise speed $v = 130\ km/h$ (referred to Cessna 337 Skymaster). The advance ratio J is calculated as follow:

$$J = \frac{v}{nD} \tag{3.15}$$

The power P and torque M can be evaluated using the following equations:

$$P = c_p \cdot \rho \cdot \left(\frac{n}{60}\right)^3 \cdot \left(\frac{D^5}{1000}\right) (kW) \tag{3.16}$$

$$M = \frac{c_q \cdot \rho \cdot (n)^2 \cdot \left(\frac{D^5}{1000}\right)}{2 \cdot \pi \cdot 60} (Nm) \tag{3.17}$$

where ρ is the air density of 1.225 kg/m3, and D is the propeller diameter. From Equation 3.17, derived through the application of the Momentum Theory, the dependence of the propeller torque M on the square of the speed n becomes evident. Therefore, the imposed braking curve at the brake bench is a good approximation of the underlying theory. The two gains referred to in Equation 3.14 were set in the control unit MP2030 as follows: $k_v = 50$ and $k_{Mn^2} = 250$. The propeller curve was obtained through fitting the data (red stars in Figure 3.33 (a, b)) acquired during a maneuver involving slight acceleration followed by deceleration of the CMD22 engine.

These data points exhibit a hysteric behavior attributed to magnetization effects generated by the eddy-current brake. Referring to Type-Certificate TCDS_E120, where the EASA certifies the airworthiness of the CMD22 engine, manufactured by CMD s.p.a., the declared rating points have been summarized in Table 3.3 and plotted (blue points) on the simulated propeller curve in Figure 3.33 (a, b). Therefore, the propeller settings are suitable for the analysis, in fact the operating points are align with the same trace.

Table 3.3. CMD22 Certified flight ratings (No.E.120) to EASA.

Ratings	**Power (kW)**	**Propeller Speed (rpm)**
Take-off	87	2500
Max. Continuous power	78	2400
75% Max Continuous Power	58	2050

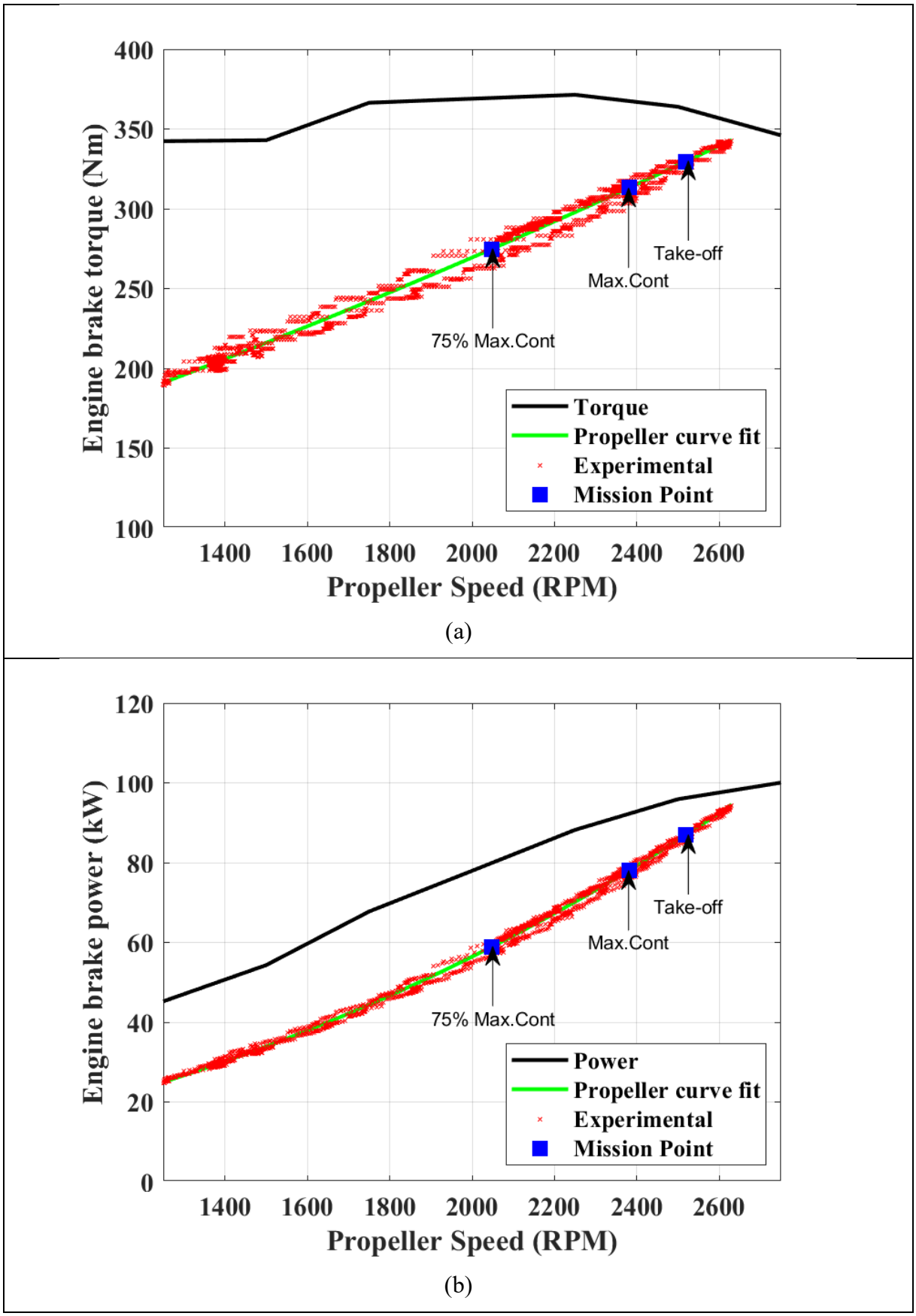

Figure 3.33. CMD 22 certified flight ratings points and propeller fitting curve: (a) Torque; (b) Power.

Each test point is achieved by simultaneously adjusting the actuation commands of both engine and motor. In particular, the throttle position angle for the Internal Combustion Engine (ICE) and the torque signal for the Electric Machine (EM). Once the desired operating point is reached, a sufficiently long period has been attended (approximately 1 minute for each point) to allow a sufficient quantity of data for post-processing, considering the monitored point is stationary for analysis purposes. This procedure confirmed the proper operation of the HEPS in both operating modes, *hybrid*, and *charging*, as designed. Additionally, it was observed that the mechanical coupling achieved through a one-way bearing ensured the correct functioning of the propulsion system.

Moreover, in the *hybrid* configuration (Figure 3.34 (a, b)), the Electric Machine (EM) works as a motor. In this test, the specific maneuver executed to reach the target point is described as follows:

1. Set a desirable EM target torque (i.e., 20, 40, 60 Nm) configured via the MD4 control touchscreen.
2. Adjust the Internal Combustion Engine (ICE) by manipulating the throttle valve position to achieve the desired torque value.

The propose tests in *hybrid* configuration show that the operational points of the Internal Combustion Engine (ICE) (highlighted in red) decrease, and a portion of Torque/Power is balanced by the EM (highlighted in green). Consequently, the operational points at Maximum Continuous Power and 75% of Maximum Continuous Power have been ensured in all tests. The sum of the ICE and EM contributions, in terms of Torque/Power, has been plotted in cyan in the figures. All data shown in Figure 3.34 (a, b) has been summarized in Table 3.4.

Moreover, in Table 3.4 are also indicated for each tested point the DC-Link measure in terms of Voltage V_{dc} and Current I_{dc} useful to calculate the battery power P_{Batt} and the electrical efficiency η_{el} by using the Equation 3.13.

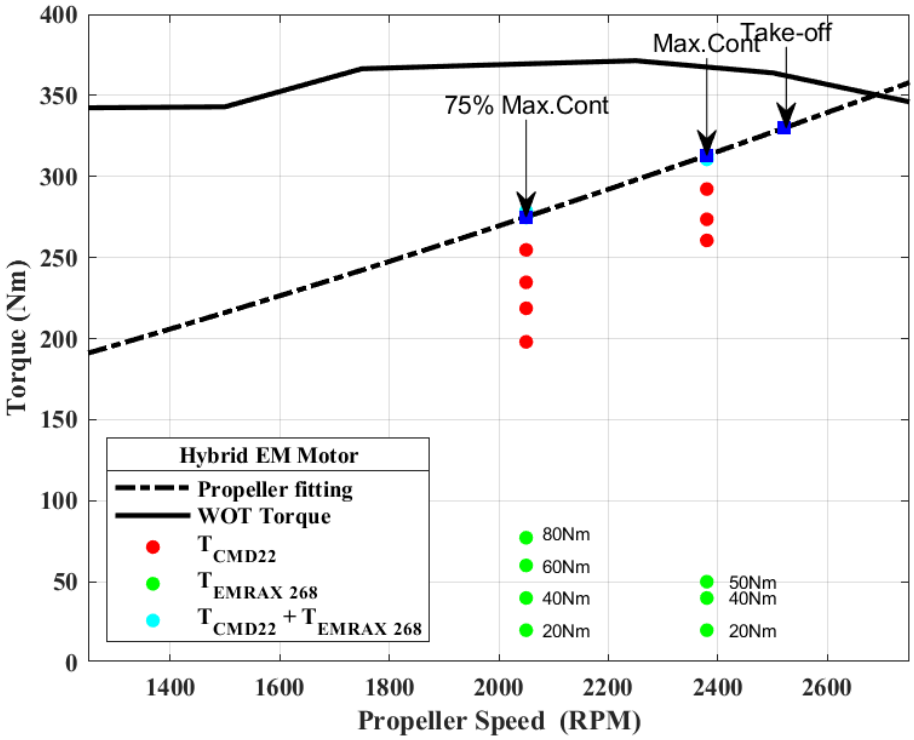

(a)

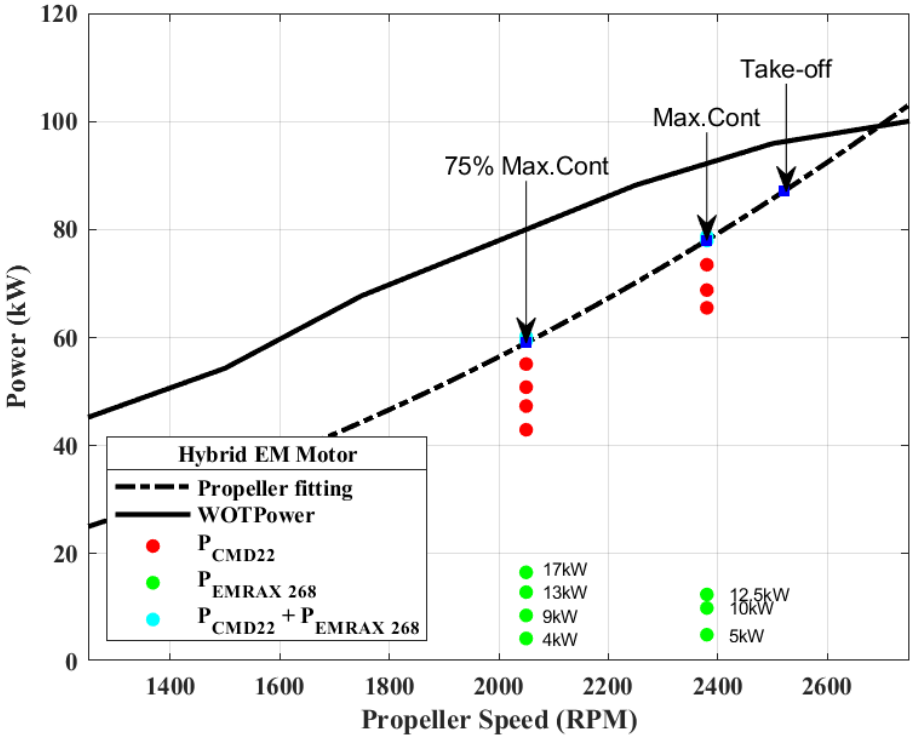

(b)

Figure 3.34.Experimental results in *hybrid* mode:(a) Torque; (b) Power.

Table 3.4. Experimental data in hybrid mode: EM works as a Motor.

Operating Point	T_{ICE} (Nm)	T_{EM} (Nm)	T_{Brake} (Nm)	P_{ICE} (kW)	P_{EM} (kW)	P_{Brake} (kW)	n_{Brake} (rpm)	V_{dc} (V)	I_{dc} (A)	P_{Batt} (kW)	η_{EL} (-)
Max.Cont	292.2	20	312.3	73.5	5	78.5	2380	250	27.5	6.9	0.73
Max.Cont	273.6	40	313.5	68.8	9.9	78.7	2380	250	45.9	11.5	0.87
Max.Cont	260.6	50	310.6	65.5	12.5	78.0	2380	250	55.6	13.9	0.90
75% Max.Cont	254.7	20	274.8	55.1	4.3	59.4	2050	250	24.0	6.0	0.72
75% Max.Cont	234.7	40	274.7	50.8	8.6	59.4	2050	250	40.0	10.0	0.86
75% Max.Cont	218.7	60	278.7	47.3	12.9	60.0	2050	250	57.0	14.3	0.90
75% Max.Cont	198.0	77.1	275.1	42.9	16.5	59.5	2050	250	71.5	17.9	0.93

A different test procedure has been adopted in *charging* mode (Figure 3.35 (a, b)), where the Electric Machine (EM) works as a generator. In this test, the specific maneuver executed to reach the target point is described as follows:

1. Take the Internal Combustion Engine (ICE) at a minimum load that ensures the Idle sustenance of the HEPS, with a torque higher than required for recharging.
2. Set a desirable EM target torque (i.e., -20, -40, -60 Nm) configured through the MD4 control unit.
3. Fine-tune of the ICE throttle valve position to achieve the desired point.

The proposed tests in charging configuration show that the operational points of the Internal Combustion Engine (ICE) (highlighted in red) have significantly increased, almost reaching maximum performance at WOT (Wide Open Throttle). A portion of Torque/Power is subtracted by the EM (highlighted in green). Consequently, the operational points at Maximum Continuous Power and 75% of Maximum Continuous Power have been ensured in all tests. In addition, the sum of Torque/Power contributions from the ICE and EM (in cyan) has been plotted. The test at the Take-off operating point didn't perform due to its highly critical nature for the ICE. The manufacturer typically recommends operating at this point for a maximum of 5 minutes, which is insufficient for a proper test execution. Therefore, the achievable charging Torque/Power at this operating point is minimal. All data shown in Figure 3.35 (a, b) has been summarized in Table 3.5. Moreover, in Table 3.5 are also indicated for each tested point the DC-Link measure in terms of Voltage V_{dc} and Current I_{dc} useful to calculate the battery power P_{Batt} and the electrical efficiency η_{el} by using the Equation 3.13.

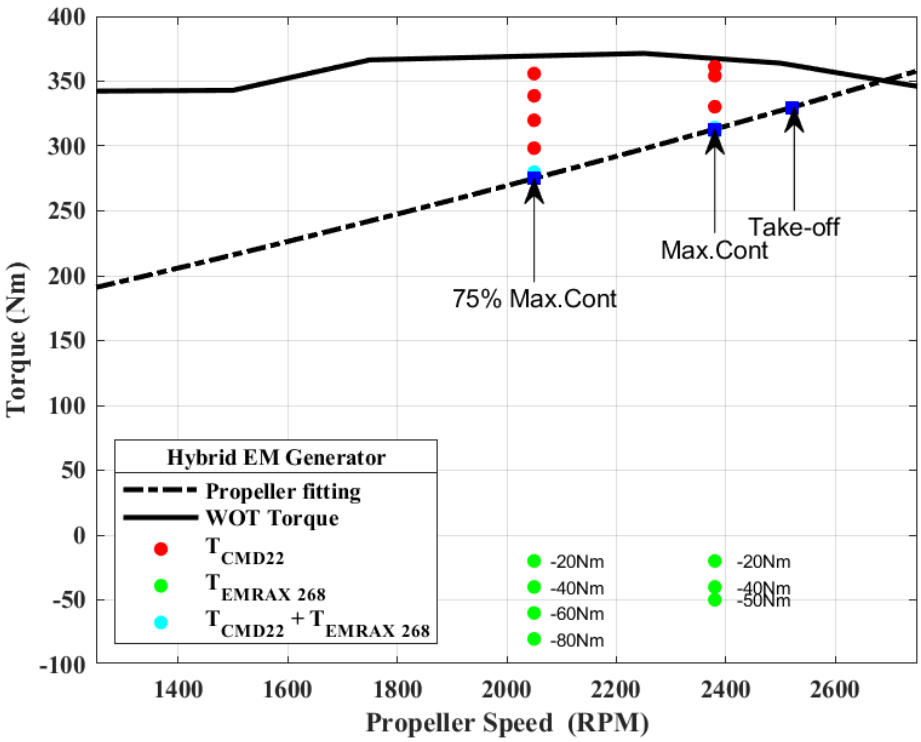

(a)

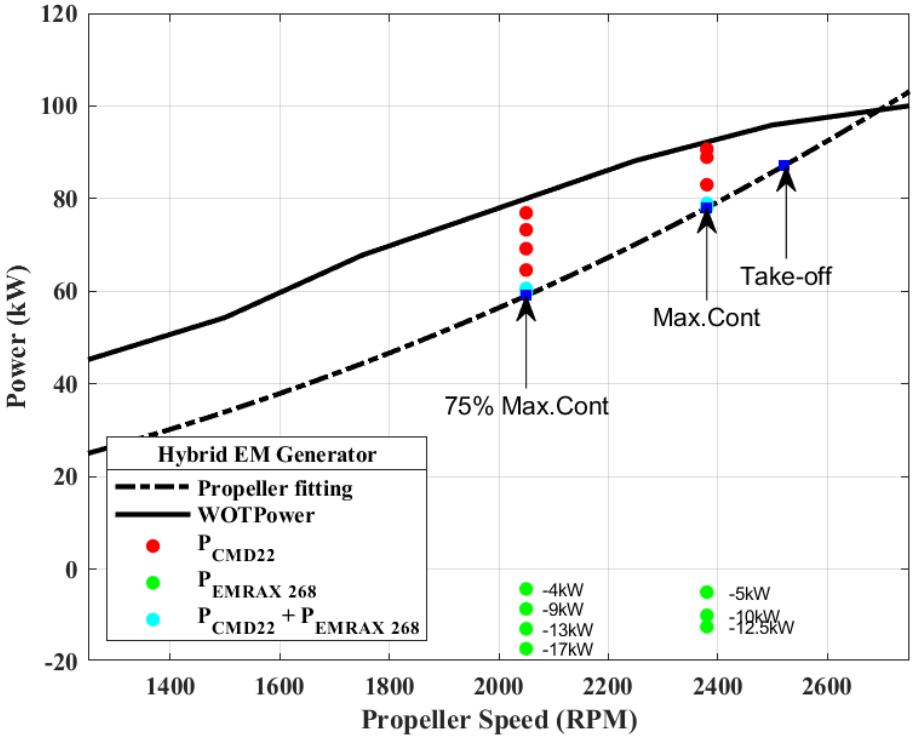

(b)

Figure 3.35.Experimental results in *charging* mode:(a) Torque; (b) Power.

Table 3.5. Experimental data in hybrid mode: EM works as a Generator.

Operating Point	T_{ICE} (Nm)	T_{EM} (Nm)	T_{Brake} (Nm)	P_{ICE} (kW)	P_{EM} (kW)	P_{Brake} (kW)	n_{Brake} (rpm)	V_{dc} (V)	I_{dc} (A)	P_{Batt} (kW)	η_{EL} (-)
Max.Cont	330.4	-20	310.4	83.0	-5.0	78.0	2380	250	-9.1	-2.3	0.46
Max.Cont	354.2	-40	314.2	90.7	-10.0	80.7	2380	250	-23.7	-6.7	0.67
Max.Cont	361.2	-50	311.2	88.9	-12.4	76.5	2380	250	-35.4	-8.8	0.71
75% Max.Cont	298.4	-20	278.4	64.6	-4.3	60.4	2050	250	-8.2	-2.0	0.48
75% Max.Cont	319.9	-40	279.9	69.2	-8.6	60.6	2050	250	-23.5	-5.9	0.68
75% Max.Cont	338.8	-60	278.7	73.3	-12.9	60.4	2050	250	-38.2	-9.6	0.74
75% Max.Cont	355.9	-80	275.8	76.9	-17.2	59.7	2050	250	-52.2	-13.0	0.76

3.2.4. Mission Simulation

In this test, a short flight mission has been simulated, repeated twice, where the HEPS is utilized in *hybrid* and *charging* operating modes. As in the previous test, the control of the Schenck brake has been set to $Mn^2 = k$ mode, where the braking torque exerted by the brake is proportional to the square of the shaft's rotational speed. The gains of the MP2030 control were set to $k_v = 50$ and $k_{Mn^2} = 250$, making the propeller curve identical to the one analyzed in the previous test. The mission is divided into two main parts, and each part consists of the following phases, summarized in Table 3.6:

1. *Taxi* –the HEPS operates in *hybrid* mode, the operating point is set at 32 kW at 1400 rpm. The taxi phase wasn't repeated in the second part of the mission.
2. *Take-off* – the HEPS operates in *hybrid* mode, the operating point is set at Take-off performances 87 kW at 2500 rpm.
3. *Climb* – the HEPS operates in *hybrid* mode, the operating point is set at Max. Continuous Power 78 kW at 2380 rpm.
4. *Cruise* – the HEPS operates in *hybrid* mode, and the operating point is set at 75% Max. Continuous Power 58 kW at 2050 rpm.
5. *Approach and Landing* – the HEPS operates in *charging* mode, at operating points with decreasing power.

The second part of the mission is repeated like the first one (excluding the initial taxi part), assuming that at the end of the first landing, the pilot performs a manoeuvre known as a "*touch-*

and-go". Additionally, it's assumed that the landing in the second phase is longer than the first, highlighting the operation of the HEPS in the charging mode.

Table 3.6. Mission phases and duration.

Mission Phase	Start Time (s)	Stop Time (s)	Duration (s)
Taxi	$t_0 = 0$	$t_1 = 24$	24
Take-off	$t_1 = 24$	$t_2 = 70$	46
Climb	$t_2 = 70$	$t_3 = 110$	40
Cruise	$t_3 = 110$	$t_4 = 265$	155
Approach & Landing	$t_4 = 265$	$t_5 = 390$	125
Take-off	$t_5 = 390$	$t_6 = 425$	35
Climb	$t_6 = 425$	$t_7 = 475$	50
Cruise	$t_7 = 475$	$t_8 = 615$	140
Approach & Landing	$t_8 = 615$	$t_9 = 728$	113

In order to make the tested mission closer to reality, the dynamic behavior of a Lithium-Ion battery has been simulated using the IT9000 simulation software of the bi-directional power supply ITECH IT6018C-500-90. For this purpose, a battery is programmed with cell specifications based on the PANASONIC NCR18650B [52], as indicated in Figure 3.36. Thus, a module is composed of 62s62p cells, with a nominal voltage of $V_{nom} = 225\ V$, a nominal capacity of $C_{nom} = 210\ Ah$, and a stored energy of $E_{nom} = 47\ kWh$.

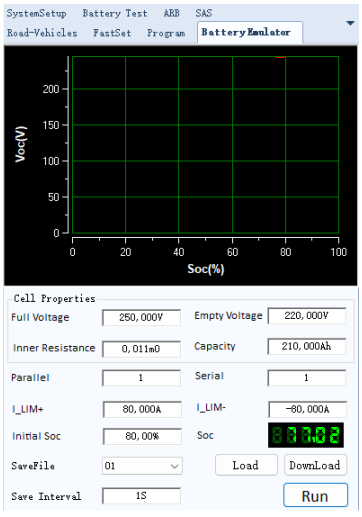

Technical specification	UoM	Data
	CELL	
Full Voltage	V	4.2
Nominal Voltage	V	3.6
Empty Voltage	V	2.5
Inner Resistance	Ω	0.011m
Rated Capacity	Ah	3400m
	PACK	
Parallel	-	62
Serial	-	62
Initial SoC	%	80
I_{max} (ITECH limit)	A	80
I_{min} (ITECH limit)	A	-80
V_{nom}	V	225
C_{nom}	Ah	210
E_{nom}	kWh	47

Figure 3.36. Cell Technical specification setting in IT9000 SW.

The experimental torque and power data related to the simulated mission have been plotted over time in Figure 3.37(a, b). These figures show the trends of torque and power over time for the

ICE, the EM, and the Brake. The Brake curve is the sum of the contributions from the ICE and EM. At time $t_4 = 265\ s$, the charging phase begins, and the EM transitions from motor operation to generator operation, reversing the sign of both torque and power. From time $t_4 = 265\ s$ to $t_5 = 390\ s$, the torque and power output from the ICE are higher than what the propeller requires (cyan Brake curve). This phenomenon can be explained by the fact that in charging mode, the CMD22 engine needs to provide extra power to balance the load of the propeller and the EM, which operates as a generator.

In Figure 3.37(b), the measured electrical power at the DC-Link (black curve), measured by the ITECH module, has also been plotted. The "*spent*" power at the DC-Link is higher than the power "*useful*" by the EM during the discharge phase (when the EM works as a motor) due to electrical efficiency losses. Similarly, during the recharge phase (when the EM works as a generator), the power "*useful*" at the DC-Link is lower than the mechanical power "*spent*" by the EM.

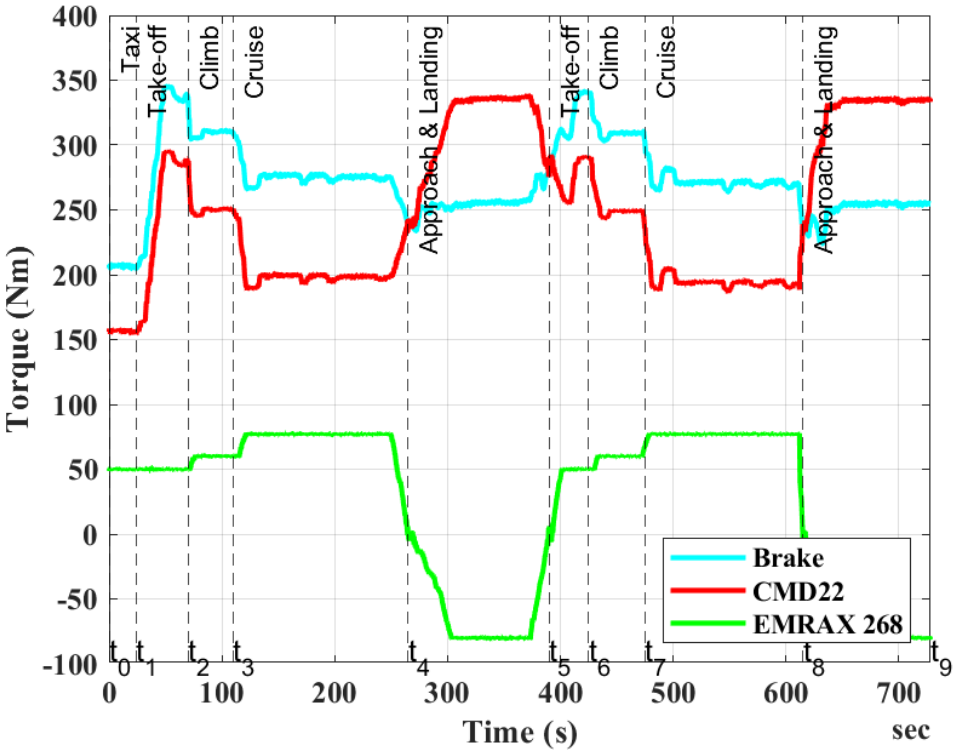

(a)

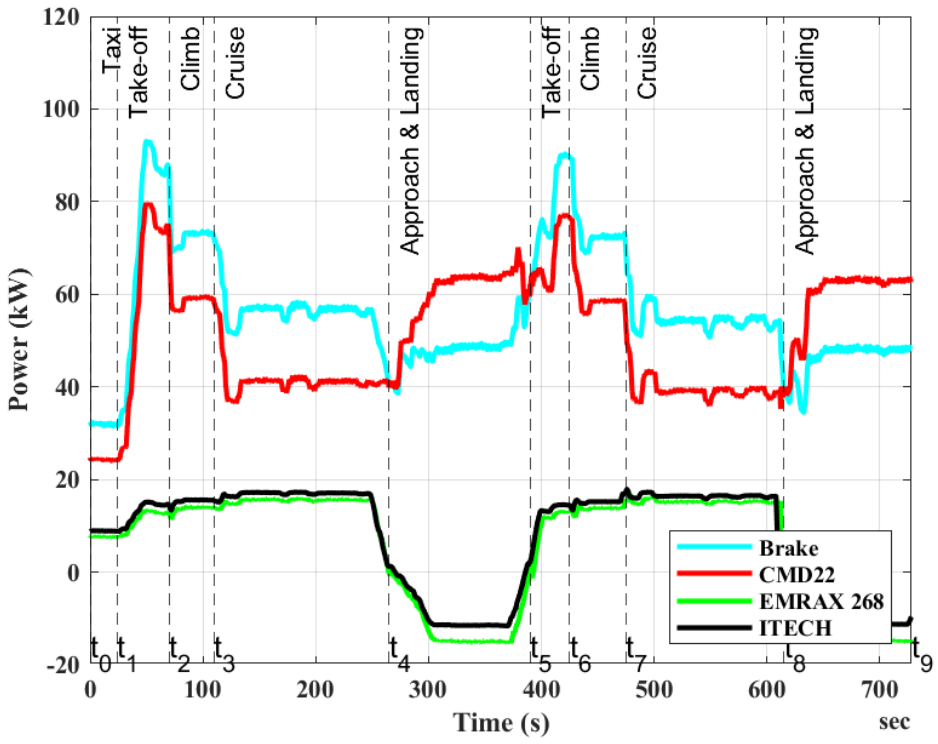

(b)

Figure 3.37. Experimental mission data on the time:(a) Torque; (b) Power.

The electrical efficiency has been calculated using Equation 3.13, and Figure 3.38 shows the efficiency values plotted during all mission time. The average efficiency during the take-off, climb, and cruise phases is around 90%. A different result has been obtained in the charging phase, where the efficiency drops significantly to 76%. The spikes shown in the graph are expected and refer to asymptotic values during the transition of the EM from motor to generator mode. The IT9000 software also recorded the State of Charge (SoC) trend of the battery over time, which is plotted in Figure 3.39. Moreover, the initial state of charge has been set equal to 80% (Figure 3.36) and decreases until 77.7% at time $t_4 = 265\ s$. Subsequently, during the landing phase, the battery has been recharged, reaching a state of charge of approximately 78.2% at time $t_5 = 390\ s$. The repetition of the second part of the mission further decreased the state of charge, reaching a minimum value of about 76.3% at time $t_8 = 615\ s$. The mission concludes at time $t_9 = 728\ s$ with a final SoC value of 77%. The overall change in the state of charge from the beginning to the end of the mission is $\Delta SoC_{t_9-t_0} = 3\%$.

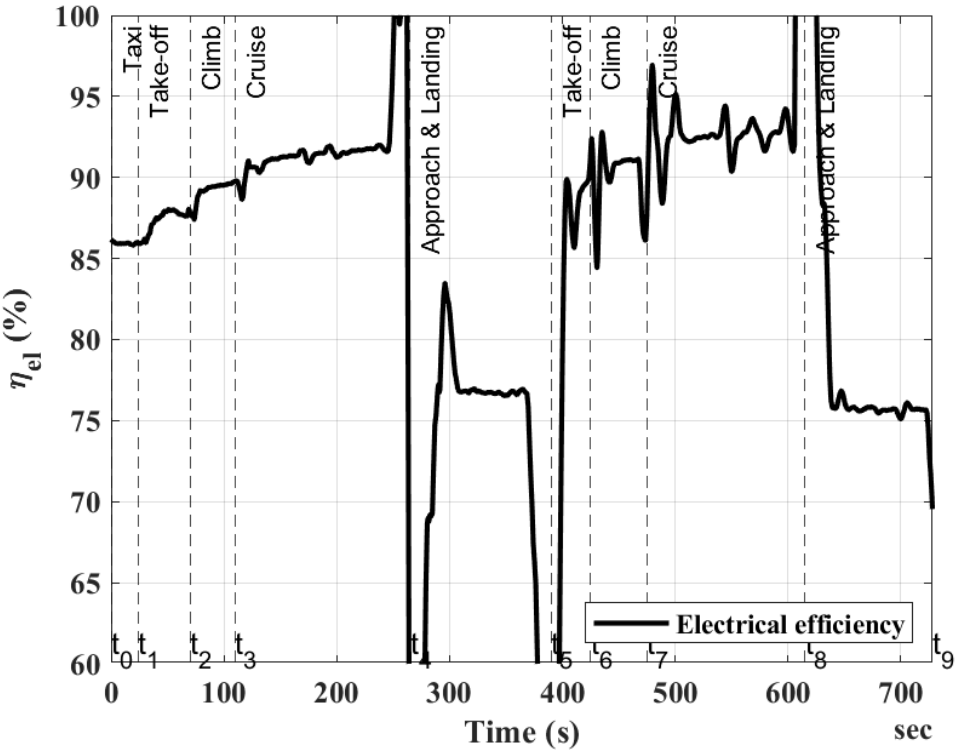

Figure 3.38. Experimental mission data on the time:(a) Torque; (b) Power.

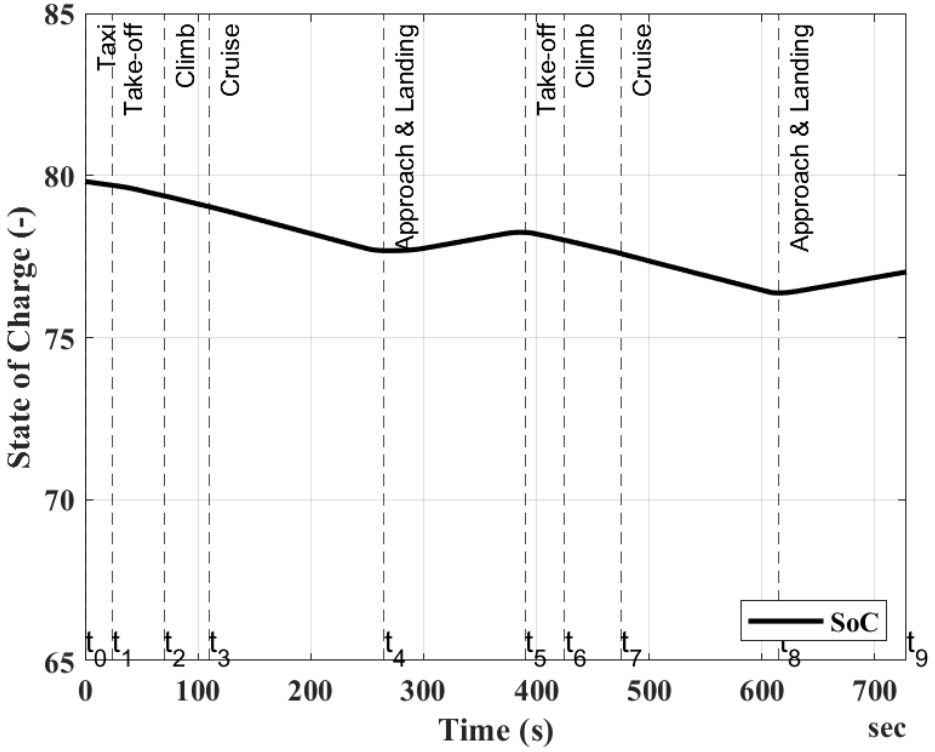

Figure 3.39. State of Charge Simulation during the mission.

The same experimental data, plotted in Figure 3.37, have also been graphed in the propeller speed to torque/power planes, as represented in Figure 3.40 (a, b, c). These figures show the ICE and EM relations to the propeller load (Brake). The propeller load appears to remain unaffected by the different operating modes of the HEPS. In fact, the torque or power values at the brake (cyan colour) consistently distribute around the propeller load represented by the dashed line. In Figure 3.40 (c), the torque values have also been plotted on the brake-specific fuel consumption (BSFC) plane of the CMD22 engine. This graph clearly indicates that the operating points of the HEPS, as related to the ICE (highlighted in red), are spread across a broader range when compared to Conventional ("*Fully-Thermal*") scenarios where only the ICE is directly connected to the propeller. Therefore, can be seen that unlike the ICE engine alone coupled to the propeller, in the HEPS propulsion architecture, the ICE can operate independently of the propeller load, allowing better or worse BSFC values to be achieved. Figure 3.40 (c) suggests that recharging the batteries may not always be advantageous. In fact, the ICE's operating points shift towards higher specific fuel consumption areas (when more torque is required at lower speed), resulting in a decreased overall efficiency of the HEPS system.

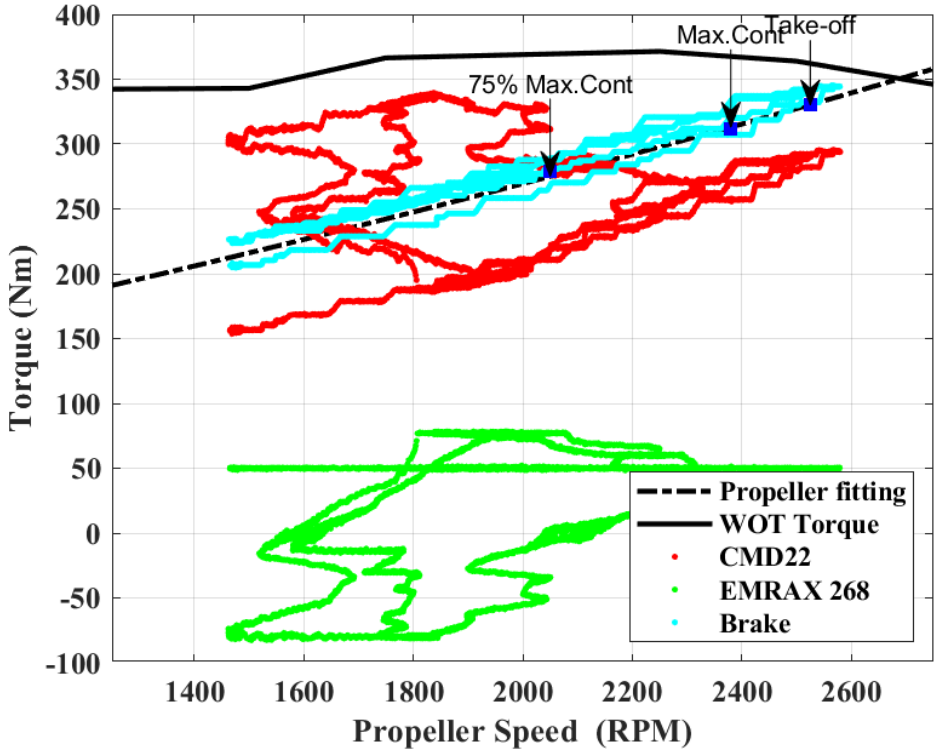

(a)

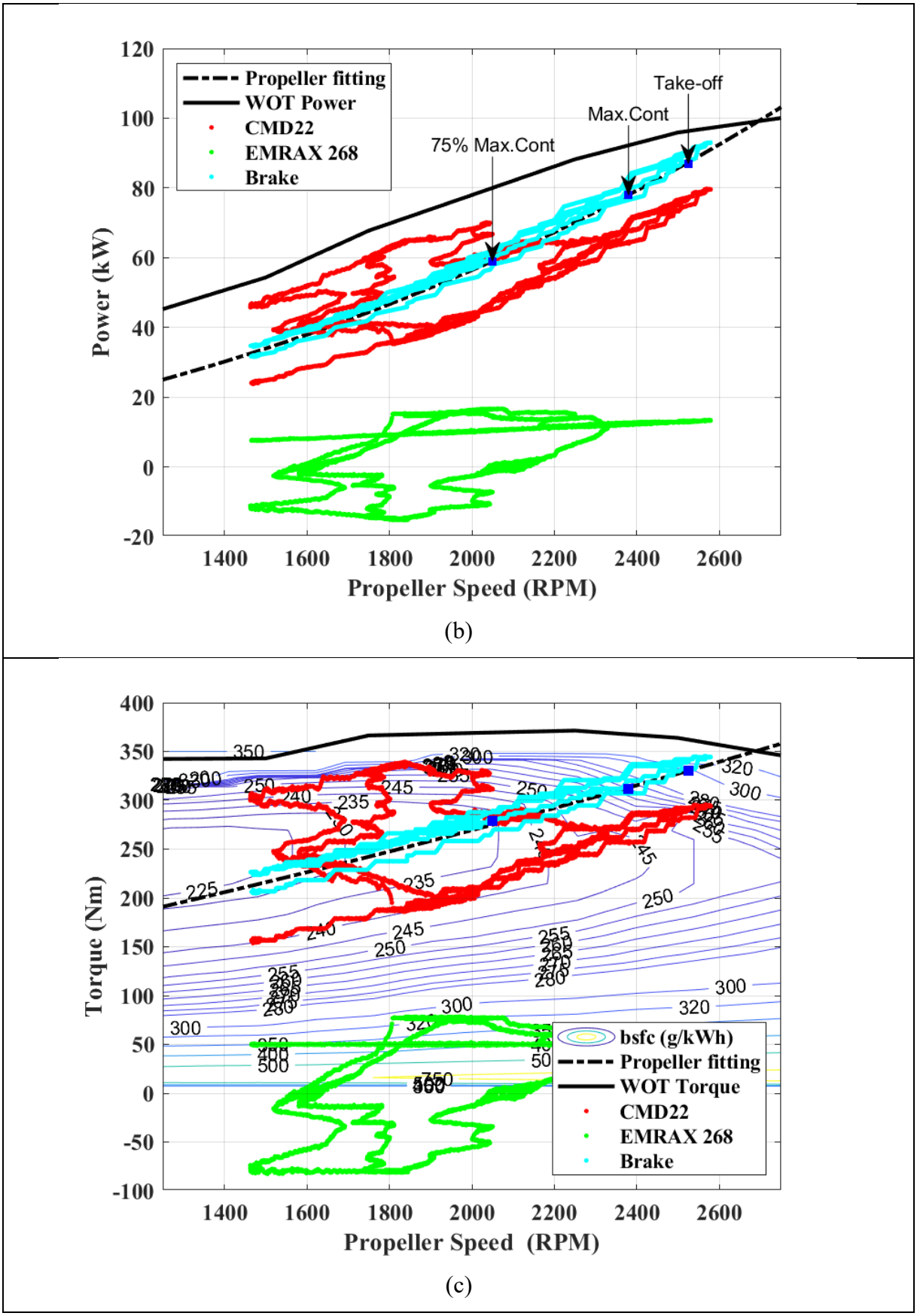

Figure 3.40.Experimental mission data on propeller speed:(a) Power; (b) Torque; (c) bsfc map.

An overall consumption assessment has been conducted by comparing the execution of the entire flight mission using two different propulsion architectures: the conventional one, which involves only the ICE (Full-Thermal), and the hybrid one (HEPS). The results, plotted in Figure 3.41, show that the fuel mass flow consumption of the HEPS architecture is generally lower than the "*Fully-Thermal*" configuration only during mission phases where the EM works as a motor. A different trend is observed during mission segments when battery charging begins; in these cases, the fuel mass flow consumption of the HEPS architecture clearly increases and becomes higher than the "*Fully-Thermal*" configuration. Moreover, a post-process of the data reveals that fuel consumption in the "*Fully-Thermal*" configuration amounts to 2.7 kg while, for HEPS, it is 2.62 kg, leading to a fuel efficiency improvement of approximately 5%. Of course, the fuel savings achieved with HEPS should also account for the energy contribution provided by the battery, which is $\Delta SoC_{t_9-t_0} = 3\%$, as it wasn't possible, within the examined mission, to return the final SoC to the initial value.

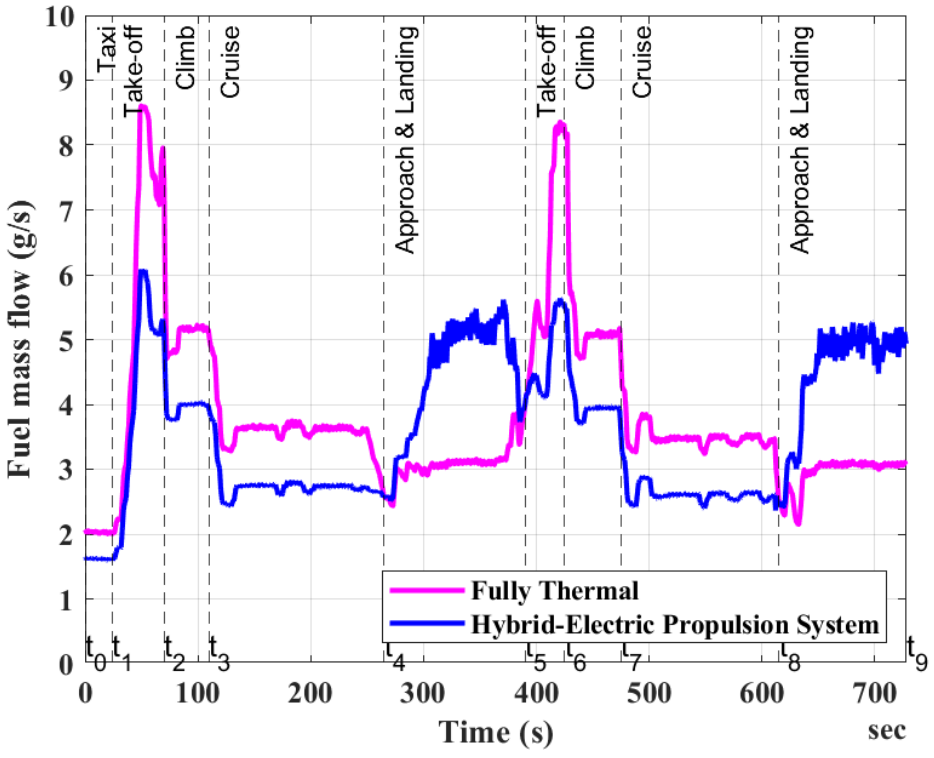

Figure 3.41. Experimental Fuel mass flow data during the mission.

A method to compare the two propulsion systems in terms of their total primary energy E_p^{total}, encompassing both the chemical energy derived from fuel E_p^{fuel} and the electrical energy stored

in the battery $E_p^{battery}$, consists of calculating the energy in both sources using the following considerations [53].

$$E_p^{total} = E_p^{fuel} + E_p^{battery} \tag{3.18}$$

where, energy E_p^{fuel} depends on the fuel consumption, while $E_p^{battery}$ depends on the battery energy consumption, both calculated through equation (3.19) and (3.20)

$$E_p^{fuel} = m_{fuel} \cdot H_i \tag{3.19}$$

$$E_p^{battery} = \frac{(SoC_{t_o} - SoC_{t_f})/100 \cdot E_{nom}}{\eta_{el}^{grid}} \tag{3.20}$$

where, m_{fuel} is the mass of fuel consumption, H_i is the AvGas 100 low heating value $H_i = 43500\, kJ/kg$ [54], SoC_{t_o} and SoC_{t_f} refers respectively to initial and final battery state of charge, E_{nom} is total battery energy capacity (see Figure 3.36), $\eta_{el}^{grid} = 0.554$ (at 2020) National Electricity Grid efficiency referred to Italian State [55]. It has been assumed that the electricity stored in the battery has been taken from the Italian National Electricity Grid and the initial battery $SoC_{t_o} = 80\%$. All data are summarized in Table 3.7.

Table 3.7. Summary of primary energy consumption.

Propulsive configuration	m_{fuel} **(kg)**	E_p^{fuel} **(kJ)**	SoC_{t_o} **(%)**	SoC_{t_f} **(%)**	$E_p^{battery}$ **(kJ)**	$E_{p_{total}}$ **(kJ)**
Fully-Thermal	2.76	$\sim 1.20 \cdot 10^5$	-	-	-	$\sim 1.20 \cdot 10^5$
HEPS	2.62	$\sim 1.14 \cdot 10^5$	80	77	$\sim 9.16 \cdot 10^3$	$\sim 1.23 \cdot 10^5$

The percentage of primary energy has been obtained by total energy comparison between "*Fully-Thermal*" $E_{p_{total}}^{FT}$ and HEPS $E_{p_{total}}^{HEPS}$ configurations through the following equation (3.21):

$$\Delta E_{\%} = \frac{E_{p_{total}}^{FT} - E_{p_{total}}^{HEPS}}{E_{p_{total}}^{FT}} = \frac{1.20 \cdot 10^5 - 1.23 \cdot 10^5}{1.20 \cdot 10^5} \approx -2.5\% \tag{3.21}$$

The analysis reveals a 5% fuel savings in the HEPS configuration compared to the "*Fully-Thermal*" one. The cost of primary energy to perform the same mission has increased by about 2.5% in the HEPS configuration if compared to the "*Fully-Thermal*".

The primary objective of these tests is to evaluate the performance of HEPS in different operating modes. Therefore, the result in terms of primary energy consumption hasn't been optimized. Additional tests and optimizations will be conducted in the future.

Chapter 4

4. HYBRID PROPULSION AIRCRAFT MODEL AND CONTROL STRATEGY

Abstract

This chapter provides a detailed description of the hybrid electric propulsion aircraft model with a numerical assessment carried out considering an air-taxi mission for 45 minutes.

The first paragraph will discuss the experimental validation of the hybrid-electric propulsion model. For this purpose, the experimental data obtained during the mission simulation (in Chapter 3) has been used to validate the hybrid powertrain consisting of an internal combustion engine, an electric machine, and the battery model linked to the dynamic model.

The second paragraph will discuss the control strategy based on the equivalent fuel consumption (ECMS). The proposed optimization strategy can be solved instantaneously, leading to a sub-optimal control strategy. In particular, the formulation of this control policy is based on the physical equivalence between the electric energy usage of the battery and the virtual fuel consumption associated with it.

Furthermore, the global hybrid electric aircraft model will be assembled and constituted by the aircraft, propeller, mission, and control strategy model.

Finally, several simulations will conducted on the parallel hybrid-electric aircraft propulsion system developed in Matlab/Simulink for different configurations based on two degrees of hybridization.

4.1. Hybrid Propulsion Model and Validation

The aircraft hybrid-electric propulsion system (HEPS), designed and experimentally characterized at the test bed (Chapter 3), has been subjected to numerical modeling and experimental validation. The numerical validation of the model has been carried out based on the experimental data obtained during the test execution of the flight mission (Chapter 3 Paragraph 3.2.4. Mission Simulation).

For this purpose, the HEPS model shown in Figure 4.1 has been designed in the Matlab/Simulink environment, consisting of the main blocks: Hybrid Propulsion, Brake Curve, and Dynamic Model. The model inputs are the torque required by the ICE (EngTrq_exp) and the torque required by the EM (MtrTrq_exp) respectively [56].

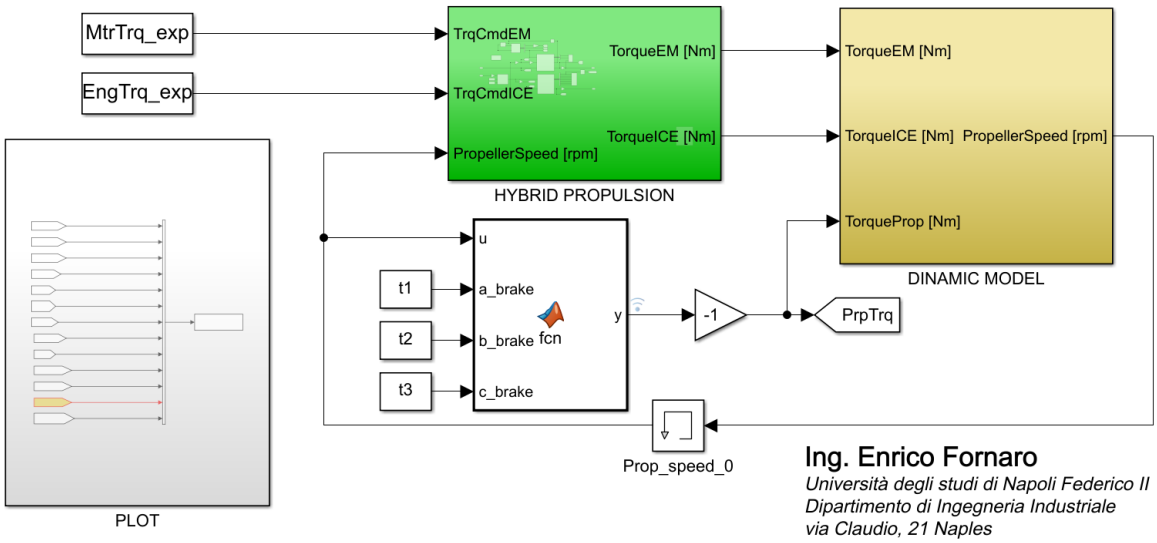

Figure 4.1. Hybrid Propulsion Model in Matlab/Simulink.

Figure 4.2 shows the inside of the Hybrid Propulsion block, which represents the heart of the propulsion system, where the following parts have been modeled: the internal combustion engine CMD22, the electric motor EMRAX 268, and the battery pack.

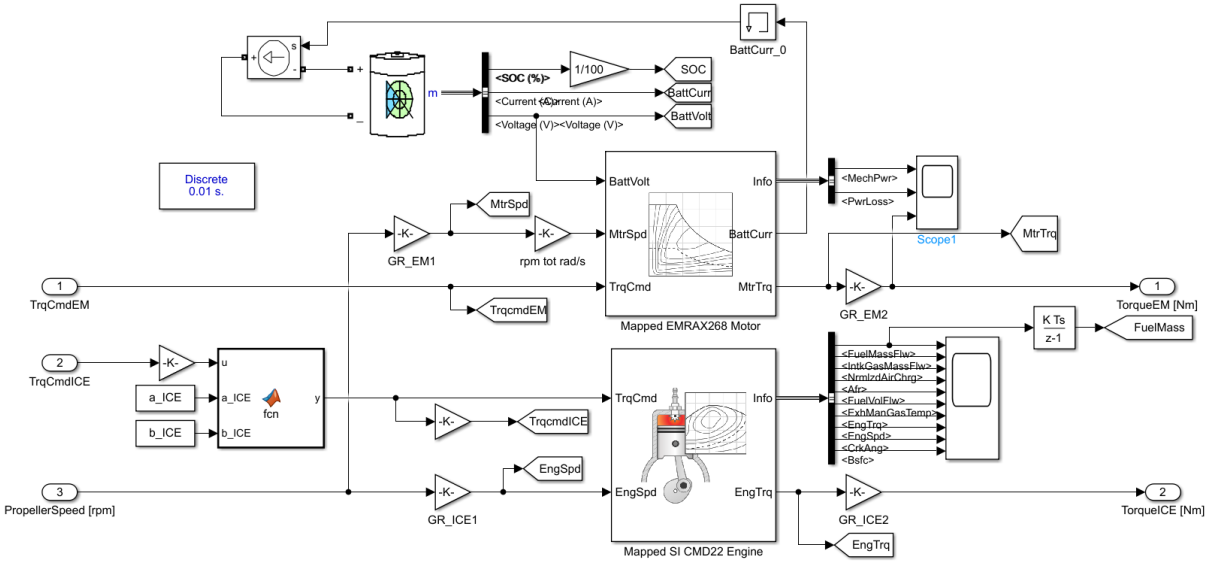

Figure 4.2. Hybrid Propulsion Block.

The ICE and EM are Map-based models employing the experimentally acquired performance data collected on a dedicated test rig. The Matlab Mapped SI Engine block is used to implement the experimental CMD22 torque and the brake specific fuel consumption (BSFC) [57]. A similar approach has been adopted for the EM where the Matlab Mapped Motor/Generator block has been used to implement the EMRAX 268 torque and efficiency [58]. Moreover, the battery voltage V_{batt} is modelled using the Simulink battery block [59]. This block implements a generic dynamic model that represents the most popular types of rechargeable batteries. In this study, a Lithium-Ion pack battery has been modelled, neglecting the battery aging effect the sizing parameter are indicated in (Cap. 3, Figure 3.36). The discharge and charge model has been described through equations 4.1 and 4.2 [60], where, i represent the charging/discharging current, i^* is the filtered current value, Q is the all battery pack capacity, and it is the current time integral plus the initial battery charge. In Figure 4.3 the most important parameters E_0, R, K, A and, B considered in this model have been shown, and in the same figure the discharge model of the battery pack is represented.

Discharge ($i^* > 0$)
$$V_{batt} = E_0 - R \cdot i - K\frac{Q}{Q - it}(i^* + it) + A \cdot exp(-B \cdot it) \quad (4.1)$$

Charge ($i^* < 0$)
$$V_{batt} = E_0 - R \cdot i - K\frac{Q}{it + 0.1 \cdot Q}i^* - K\frac{Q}{Q - it}it + A \cdot exp(-B \cdot it) \quad (4.2)$$

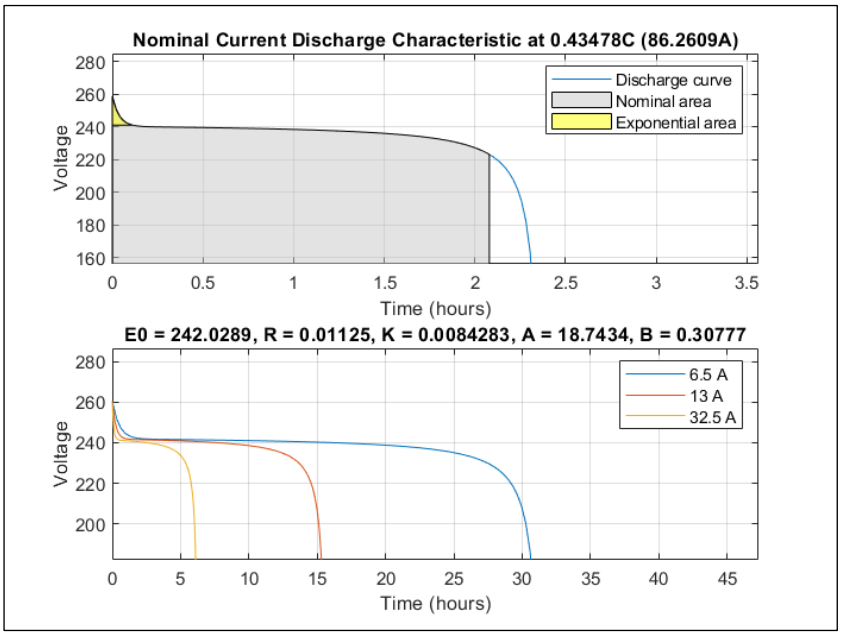

Figure 4.3. Battery pack discharge characteristics model.

The Brake Curve, like to the propeller load, has been experimentally simulated by setting the MP2030 control of the Schenck brake to the $Mn^2 = k$ mode has shown in Figure 3.33 and Figure 3.40. The numerical equation referred to the brake load has been evaluate through a best fitting starting form experimental data (speed, torque, power). Moreover, the numerical torque $T(n)$ and power $P(n)$ curves are following described:

Torque Brake

$$T(n) = t1 \cdot n^2 + t2 \cdot n + t3$$
$$t1 = 8.94 - 06;\ t2 = 0.075;\ t3 = 82.65 \tag{4.3}$$

Power Brake

$$P(n) = p1 \cdot n^3 + p2 \cdot n^2 + p3 \cdot n + p4$$
$$p1 = 9.59 - 10;\ p2 = 7.82 - 6;\ p3 = 0.0087;\ p4 = -0.013 \tag{4.4}$$

Where n is the propeller speed in rpm.

Finally, the Dynamical Model has been modelled using the torque balance Equation 4.5 and discretizing this equation is possible estimate the propeller speed velocity trough the Equation 4.6.

$$T_{ICE} + T_{EM} - T_{PROP} = I\frac{d\omega}{dt} \cong I\frac{\omega_f - \omega_i}{t_f - t_i} \tag{4.5}$$

$$\omega_f = (T_{ICE} + T_{EM} - T_{PROP}) \cdot \frac{\Delta t}{I} + \omega_i \tag{4.6}$$

Where, T_{ICE} is the ICE torque, T_{EM} is the EM torque (positive when EM work as a motor, negative work as a generator), T_{PROP} is the propeller's resistant torque, I is the system's overall moment of inertia, and ω is the propeller angular speed in rad/s. The moment of inertia (Table 4.1) is sum of three components: I_{EM} has been given by the manufacturer's EM datasheet; in this case, I_{PROP} has been replaced by the brake dynamometer moment of inertia; the remaining moment of inertia (ICE, pulleys, and free wheel inertia) has been obtained through a parameter estimator process and reflected to the propeller shaft.

Table 4.1. Summary of Moment of Inertia.

Description	UoM	Inertia
EMRAX 268	kgm^2	0.0922
EDDY BRAKE SCHENCK	kgm^2	0.61
CMD22 and mech. coupling	kgm^2	0.3

The simulation solver is ode4 (Runge-Kutta), with a fixed step size $\Delta t = 0.01s$. Moreover, the initial value of propeller speed has been set equal to zero $\omega_0 = 0$, and the initial battery State of Charge is set equal to 80%.

The speed trends in Figure 4.4 (a) are almost similar in EM, ICE and the brake, confirming the correct mechanical coupling constraints between all components. The EM torque comparison, in Figure 4.4 (b), confirm a good matching between the experimental and simulation one results. Otherwise, the ICE and brake torque shows more variation, which could be ascribed to a less ICE map accuracy, and a braking curve approximation. The battery trends shows in Figure 4.4 (c) is good. The simulated battery current and voltage variation with respect experimental one can be attributed to a simple battery model chosen. In fact, the battery model does not take into account the thermal and aging behavior of the battery.

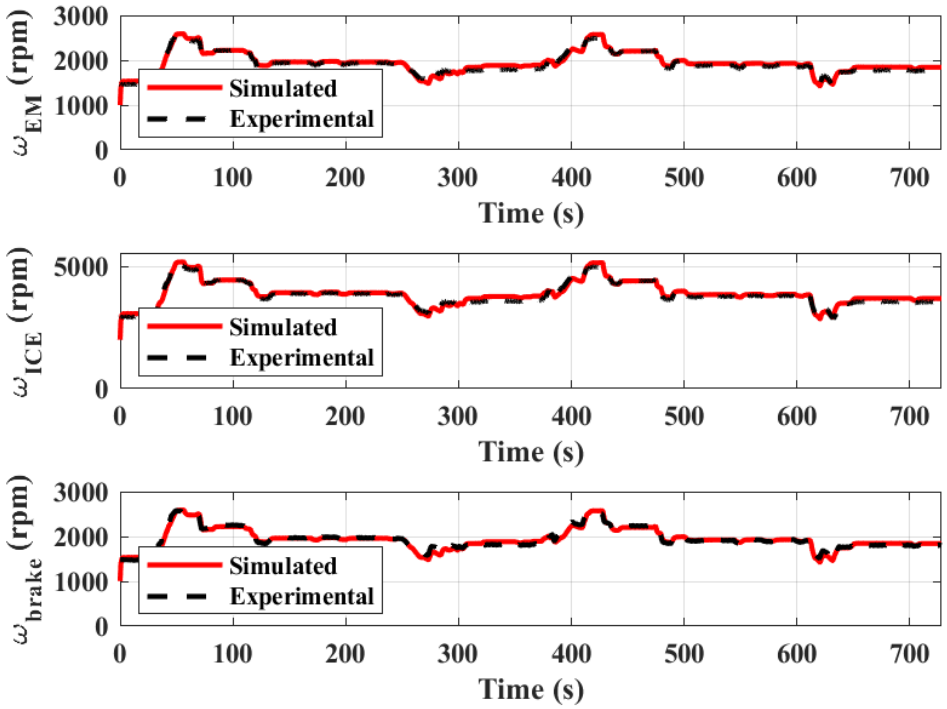

(a)

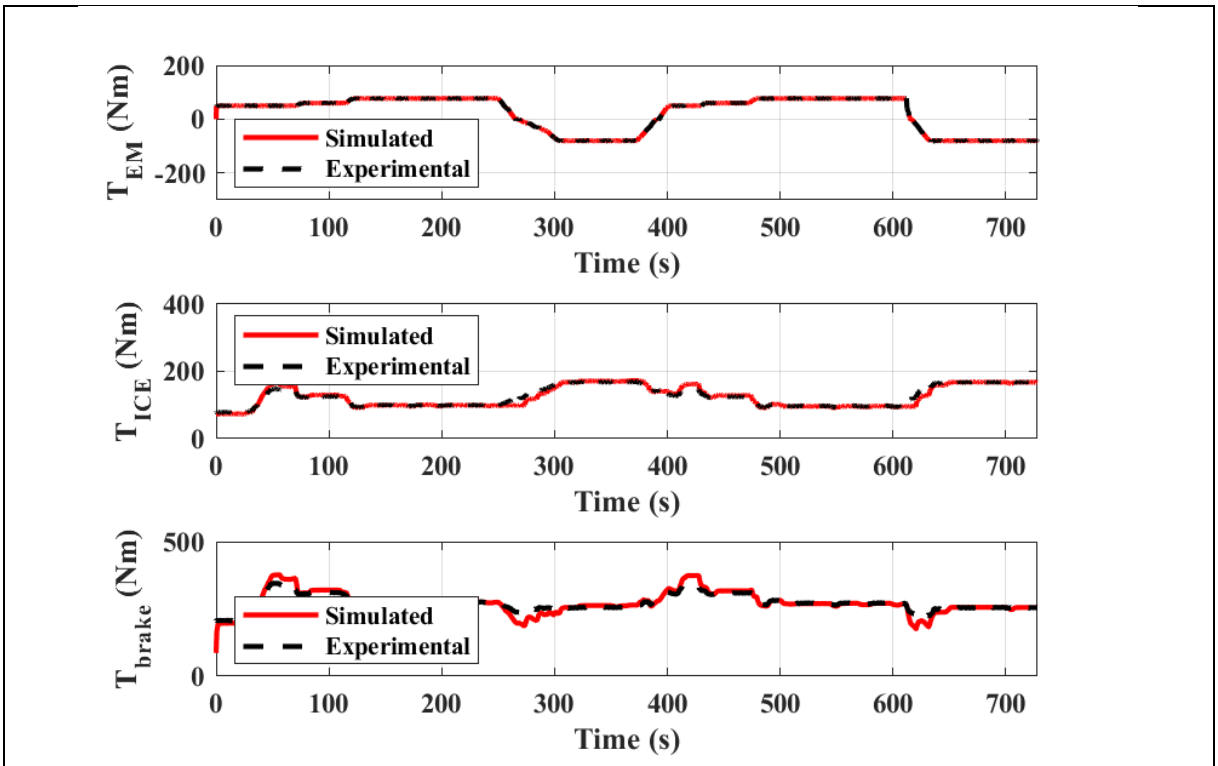

(b)

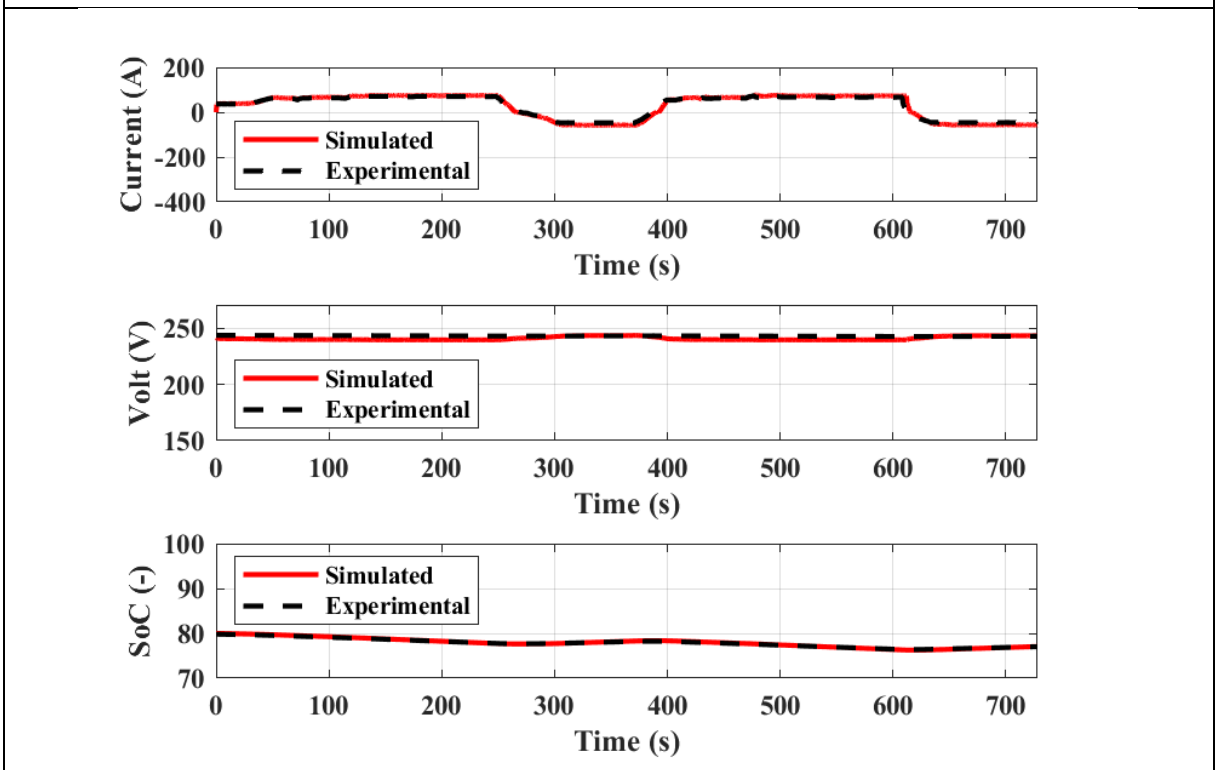

(c)

Figure 4.4. Comparison between experimental and simulated signals: (a) speed, (b) torque and (c) battery quantities.

In all cases a good matching between the experimental and simulated curves has been highlighted. Moreover, same considerations are true for battery State of Charge, Current and Voltage. Two different statistical indexes are also calculated for a better performance analysis. These indexes are respectively, Root Mean Square Error (RMSE) and Normalized Root Mean Square Error (NRMSE). Normalizing the RMSE facilitates the comparison between datasets or models with different scales. Moreover, the NRMSE value is commonly expressed as a percentage where the normalization is referred to the magnitude variation range $(\mathrm{t}_{\mathrm{max,k}} - \mathrm{t}_{\mathrm{min,k}})$.

$$\mathrm{RMSE}_{,\mathrm{k}} = \sqrt{\frac{1}{\mathrm{N}}\sum_{i=1}^{N}\left(t_{i,k} - y_{i,k}\right)^2} \tag{4.7}$$

$$\mathrm{NRMSE}_{,\mathrm{k}} = \frac{\mathrm{RMSE}_{,\mathrm{k}}}{t_{\mathrm{max,k}} - t_{\mathrm{min,k}}} \tag{4.8}$$

In Equations 4.7 and 4.8, $t_{i,k}$ are the reference values provided by the experimental tests, $y_{i,k}$ are the simulated value provided by the model. Moreover, the subscript k is referred to the different considered signal, summarized in Table 4.2.

Table 4.2. Goodness indexes of the modeling matching for Speed, Torque and Battery parameters.

Signals	**UoM**	**RMSE (UoM)**	**NRMSE (%)**
Speed ICE	(rpm)	107.4	0.04
Speed EM	(rpm)	54.1	0.04
Speed Brake	(rpm)	48.41	0.04
Torque ICE	(Nm)	90.7	2.97
Torque EM	(Nm)	0.56	0.003
Torque Brake	(Nm)	14.0	0.49
Battery Current	(A)	7.7	0.06
Battery Voltage	(V)	2.6	2.54
Battery SoC	(-)	0.16	0.04

The NRMSE confirm the good matching of the proposed model with experimental data, the maximum percentage error is 2.97% regarding to estimation of torque ICE thath could be

ascribed to a less ICE map accuracy and 2.54% regarding to estimation of battery voltage thath could be ascribed to a simple battery model chosen.

4.2. Control Strategy Implementation (ECMS)

Generally, the goal of hybrid-electric control is the instantaneous management of the power flow from the ICE and the EM able to minimize the overall consumption. For this purpose, many control and optimization strategy has been developed, but each one has good and negative characteristics. If the mission profile is a-priori known, Dynamic Programming (DP) or analytical optimal control techniques could be used to find optimal solution [61]. Unfortunately, this solution cannot be implemented in real-time but only be used as a benchmark for other real-time strategies. These include rulebased control, Model Predictive Control (MPC) and Equivalent Consumption Minimization Strategy (ECMS). The last optimization strategy proposed by Paganelli [62] can be solved instantaneously, leading to a sub-optimal control strategy. In particular, the formulation of this control policy is based on the physical equivalence between the electric energy usage of the battery and the virtual fuel consumption associated with it [63]. Thus, the instantaneous equivalent fuel consumption to be minimized results in:

$$\dot{m}_{f,eq}(t) = \dot{m}_f(t) + \dot{m}_{f,b}(t) \tag{4.9}$$

where $\dot{m}_f(t)$ is the effective fuel consumption referred to the ICE, and $\dot{m}_{f,b}(t)$ is the virtual fuel consumption associated with battery usage. By analogy with the engine, the latter can be expressed introducing a virtual specific fuel consumption, $sfc_{eq}\left(\frac{g}{kWh}\right)$, giving:

$$\dot{m}_f = \frac{P_{ICE}}{\eta_{ICE} \cdot H_i} \tag{4.10}$$

$$\dot{m}_{f,b} = sfc_{eq} \cdot P_{batt} = s \cdot \frac{P_{batt}}{H_i} \tag{4.11}$$

Where, H_i is the fuel lower heating value, η_{ICE} engine efficiency, P_{ICE} power produced by engine, P_{batt} is the battery power. By substituting the Equations 4.10 and 4.11 in Equation 4.9 and multiply all for H_i yields:

$$\mathrm{P}_{eqv}(t) = P_{fuel}(t) + s \cdot P_{batt} \tag{4.12}$$

The main aim of this work is to show that the power of the ECMS based on Pontraygin's Minimum Principle (PMP) [64] could be used for a hybrid-electric propulsion system for aircraft applications, considering the propulsion coupling effects on the propeller. Moreover, the ECMS control strategies is computationally cheap for real-time implementation even if the reduces the non-realizable global minimization criterion to a realizable local one.

4.2.1. Optimization problem

In general, for the control system, a control-oriented model of the battery is used; it's based on a zero-th order equivalent circuit model. According to definition of State of Charge (SoC) Equation 4.13 and control input Eqation 4.14, the system dynamics Equation 4.15 given by [61], [65]:

$$x = SoC \tag{4.13}$$

$$u = P_{batt} \tag{4.14}$$

$$\dot{x} = -\frac{I}{C_{nom}} \tag{4.15}$$

where I is the current flowing supplied by the battery and C_{nom} is the battery nominal capacity. Thus, the battery power can be expressed as follow:

$$P_{batt} = V_{batt} \cdot I \tag{4.16}$$

where, V_{batt} is battery voltage. Solving the Equation 4.16 for the current and replacing into Equation 4.15, yields:

$$\dot{x} = -\frac{P_{batt}}{V_{batt} \cdot C_{nom}} \tag{4.17}$$

The energy management is formulated into a global optimization problem, of which objective is to minimize the fuel consumption for the complete mission, but this formulation requires a priori knowledge of the complete mission profile.

$$J = \int_{t_0}^{f_f} \dot{m}_f(u,t)\,dt \tag{4.18}$$

where t_0 is the initial time and t_f the final time. To avoid this drawback, the ECMS proposes to replace the noncausal formulation with an instantaneous one based on Pontraygin's Minimum Principle formulation [64]. In this way, global optimization can be replaced by sub-optimal optimization by adopting the Hamiltonian function (Equation 4.19) and minimizing it at each time instant

$$H = \dot{m}_f + \lambda \cdot \dot{x}(t) \tag{4.19}$$

Where λ is a vector of optimization variables, also know as adjoint states or co-states of the system. By substituting Equation 4.17 in Equation 4.19 and multiply all for H_i yields:

$$H = P_{fuel} + \lambda \cdot \left(-\frac{P_{batt}}{V_{batt} \cdot C_{nom}}\right) \cdot H_i \tag{4.20}$$

Therefore, the equivalence between the Hamiltonian Equation 4.20 and ECMS instantaneous cost Equation 4.12 is complete if the *s* equivalence factor are linked to the λ co-state as follow:

$$s = \lambda \cdot \left(-\frac{1}{V_{batt} \cdot C_{nom}}\right) \cdot H_i \tag{4.21}$$

Thus, the Equation 4.20 can rewrite as follow:

$$H = P_{fuel} + s \cdot P_{batt} \tag{4.22}$$

When ECMS is implementing, a penalty function is often used to guarantee that the battery SoC does not exceed the admissible limits [66]. Therefore, the Equation 4.22 could be modified by using an appropriately constructed multiplicative penalty function, $p(SoC)$ as follow:

$$p(SoC) = 1 - \left(\frac{SoC(t) - SoC_{target}}{\frac{SoC_{max} - SoC_{min}}{2}} \right)^{a} \tag{4.23}$$

The penalty function plays a critical role to achieve a desirable online battery SoC target avoiding to exceed the battery charge limits. To correct the battery SoC are possible different function shapes when exponent $a = 1; 3; 5$ is correctly chosen (Figure 4.5). Generally, the battery SoC limits are included in a range between $SoC_{min} = 20\%$ and $SoC_{max} = 95\%$, but these can be changed depending on the case study analysed [66].

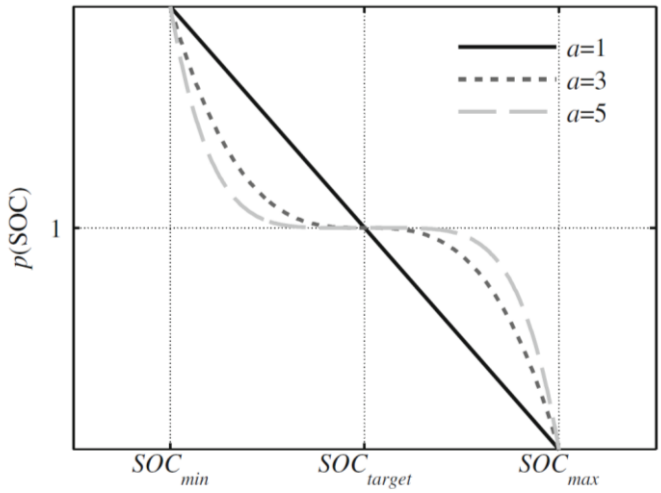

Figure 4.5. Multiplicative penalty function $p(SoC)$ [61].

Moreover, a Trace Power Error parameter ($TracPwrErr$) (Equation 4.24) has been added to the Hamiltonian function. This parameter increases the value of the worst command torques combination between ICE ($\boldsymbol{T}_{ICE}^{options}$) and EM ($\boldsymbol{T}_{EM}^{options}$), while reduce the value of the better value combination. Therefore, the Trace Power Error parameter helps to choose the correct command torques combination between ICE and EM, during the Hamiltonian function minimization.

$$TracPwrErr = \left| \left(PropTrqCmd - (\boldsymbol{T}_{ICE}^{options} + \boldsymbol{T}_{EM}^{options}) \right) \right| \cdot PropSpeed \cdot TPE_{factor} \tag{4.24}$$

The TPE_{factor} is a multiplicative constant factor assumed in this work equal to $TPE_{factor} = 6$. Finally, the physical constraints of each HEPS component is also considered. Following the boundary expression are highlighted:

$$\begin{aligned} SoC_{min} \leq SoC \leq SoC_{max} \\ P_{batt_{min}} \leq P_{batt} \leq P_{batt_{max}} \\ T_{i_{min}} \leq T_i \leq T_{i_{max}} \\ \omega_{i_{min}} \leq \omega_i \leq \omega_{i_{max}} \end{aligned} \tag{4.25}$$

Where T and ω are respectively torque and angular speed and $i = ICE, EM$.

A trick implementing solution has been developed when the engine's torque values involve a physical out-range solution Equations 4.25. In this case, the parameter ($Constraint\ Penalty$) increases, making the combined torque solution range not the preferred solution.

The global Hamiltonian function needs to be minimized can be written as follows:

$$\min_{ICE,EM} H = P_{fuel} + s \cdot P_{batt} \cdot p(SoC) + TracPwrErr + Constraint\ Penalty \tag{4.26}$$

In Figure 4.6 has been shown the ECMS Control Strategy Block implemented in Matlab/Simulink environment.

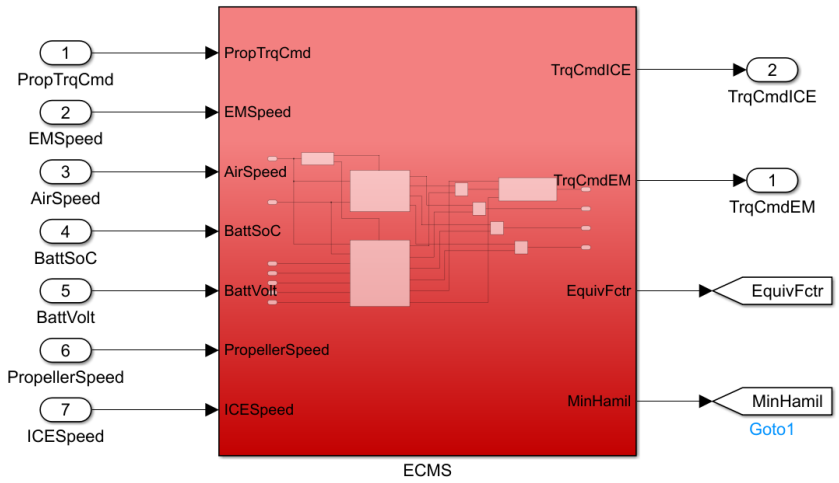

Figure 4.6. ECMS Control Strategy Block in Matlab/Simulink.

Moreover, in the Figure 4.7, the implementation scheme of the Equivalent Consumption Minimization Strategy adopted in this work has been shown.

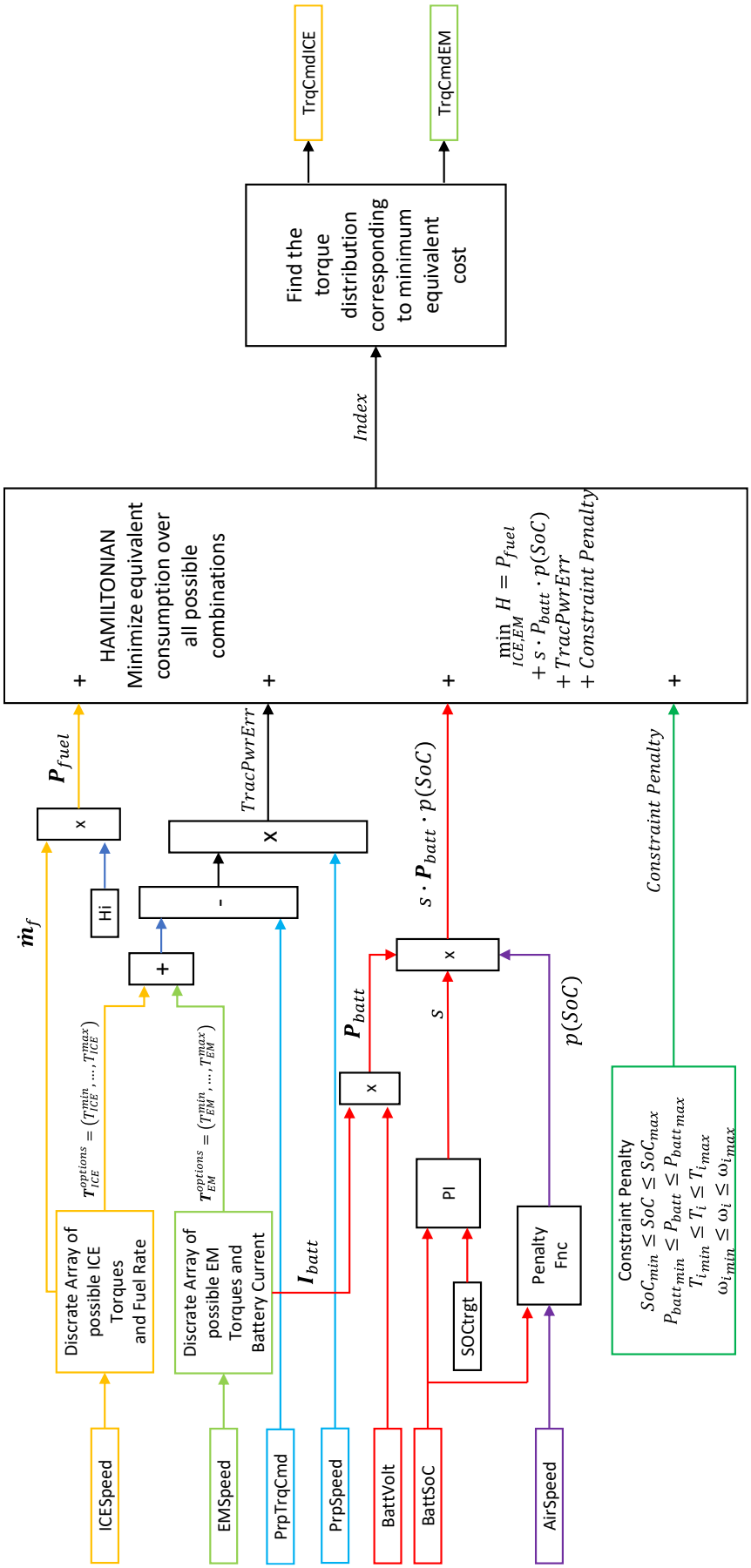

Figure 4.7. ECMS Implementation Scheme.

A. Rezaei et al. [67] purpose a way to find consistent values for s in order to have a better calibrated equivalence factor. Their work does not seek to estimate the optimal equivalent factor, but instead upper and lower bounds of s are estimated. They obtain two inequalities, using the actual values of efficiency at the predicted operating conditions of the components in the hybrid electric propulsion system, regardless of the drive-cycle or of the trip duration. For a parallel hybrid-electric system the equivalent factor s lies within the range:

$$1 < s < \frac{\eta_{trs}^{max} \cdot \eta_{EM}^{max} \cdot \eta_{inv}^{max} \cdot \eta_{batt}^{max}}{\eta_{trs}^{min} \cdot \eta_{ICE}^{min}} \tag{4.27}$$

Where η_{trs}^{max} is the transmission efficiency, η_{EM}^{max} is the electrical machine efficiency, η_{inv}^{max} is the inverter efficiency, η_{batt}^{max} is the battery efficiency and η_{ICE}^{min} is the internal combustion engine efficiency.

The equivalent factor, in ECMS control, is considered constant during the mission equal to $s_0 = 3.395$, in this case the mean efficiency are assumed $\bar{\eta}_{EM} = \bar{\eta}_{Inverter} = 0.92$, $\bar{\eta}_{batt} = 0.88$, $\bar{\eta}_{ICE} = 0.22$ and $\bar{\eta}_{trs} = 1$.

4.2.2. Adaptation Based on Feedback from SOC (A-ECMS)

Approaches developed to design adaptive optimal supervisory control methods based on SOC feedback [68 - 70] are based on the idea to change dynamically the value of the co-state at the present time (without using past driving information or attempting to predict future driving behavior), in order to contrast the SOC variation and thus maintain its value around the target value. If, on one hand this method is easy to implement, robust (as it all rely on feedback from SOC) and computationally cheap, on the other hand it performance relies on a suitable tuning of the parameters used in the adaptation law.

The online adaptation of the co-state through SOC feedback uses the difference between the target state of charge, SoC_{target} (considered constant during mission time), and its instantaneous value, SOC(t). A similar approach adopted in [68] has been used in this work, where an adaptation law based on a proportional-integral (PI) controller of the type

$$s(t) = s_0 + k_P \left(SoC_{target} - SoC(t)\right) + k_I \int_0^t \left(SoC_{target} - SoC(t)\right) dt \tag{4.28}$$

was proposed. In the Equation 4.28, s_0 represents the initial value of s at time $t = 0$, and k_P and k_I are the proportional and integral gains of the adaptation law. The initialization of this algorithm, i.e., the choice of s_0, is arbitrary, and it can be done by averaging different optimal initial values obtained offline.

4.3. Global Hybrid Propulsion Aircraft Model

This section describes the global hybrid propulsion Aircraft Model. The global model is constituted by Hybrid Propulsion and Dynamic Model blocks described and validated in section 4.1. Moreover, Aircraft and Propeller models have been added to the global one. The Hybrid Propulsion, constituted by ICE, EM, and battery, is controlled by the ECMS block presented in section 4.2. Finally, a representative mission has been selected to evaluate the performance of the proposed hybrid-electric architecture.

4.3.1. Aircraft

A lumped parameters model of the Cessna 337 aircraft has been developed. The aircraft has been considered as a 4th order point mass describing the longitudinal dynamic along the aerodynamic axis X_a, as shown in Figure 4.8. The ordinary differential equation (ODE) associated with the longitudinal motion of the aircraft model is written as follows [71]:

$$m\dot{v} = T + L + D + W \tag{4.29}$$

Where:

- $\dot{v} = \frac{dv}{dt}$ is the acceleration of the aircraft, in m/s^2;
- $m = 1700\ kg$ is the lumped mass of the aircraft [72];
- T is the propeller thrust, in N;
- D is the drag force, in N;
- L is the lift force, in N;
- W is the weight, in N;
- the product $m\dot{v}$ is the inertia force produced by the aircraft in N.

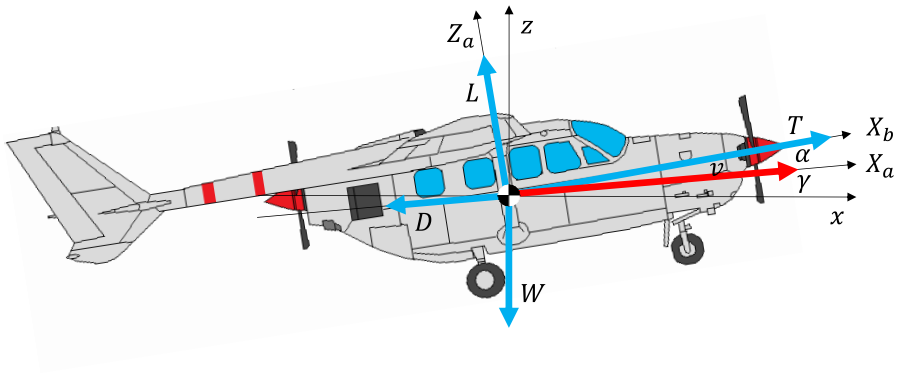

Figure 4.8. Schematization of the aircraft dynamical model [72].

The flight path angle γ is the one between the x axis and the true speed v. The angle of attack α is the one between the longitudinal axis X_b and the true speed v. The sum of angles α and γ constitutes the pitch angle φ. The aerodynamic axis X_a is parallel to the true speed v and is considered positive in the flight direction. The sustenance force F_z and the propulsion force F_x, which balance the composition of lift L, drag D, thrust T, and weight W forces, can be obtained by applying Newton's Second Law on the aircraft, providing the following equations related to a symmetric flight of the aircraft model:

$$F_z = mv\dot{\gamma} = \big(L + Tsin(\alpha)\big) - Wcos(\gamma) \tag{4.30}$$

$$F_x = m\dot{v} = Tcos(\alpha) - D - Wsin(\gamma) \tag{4.31}$$

$$\dot{h} = \sin(\gamma) \tag{4.32}$$

where Equation 4.32 constitutes the altitude kinematic one. Furthermore, drag, lift and weight forces are computed as follows:

$$D = \frac{1}{2}\rho S v^2 C_D \tag{4.33}$$

$$L = \frac{1}{2}\rho S v^2 C_L \tag{4.34}$$

$$W = mg \tag{4.35}$$

Where:

- $\rho = 1.225\ kg/m^3$ is the air density;
- $S = 19\ m^2$ is the aircraft wing area;

- C_D and C_L are the drag and lift coefficients related to a NACA 2412 airfoil (Figure 4.9) [73];
- $g = 9.81\ m/s^2$ is the gravity acceleration.

The total drag coefficient C_D is evaluated as the sum of the aircraft cabin frontal drag $C_{d0} = 0.054$ and the airfoil one C_d:

$$C_D = C_{d0} + C_d \tag{4.36}$$

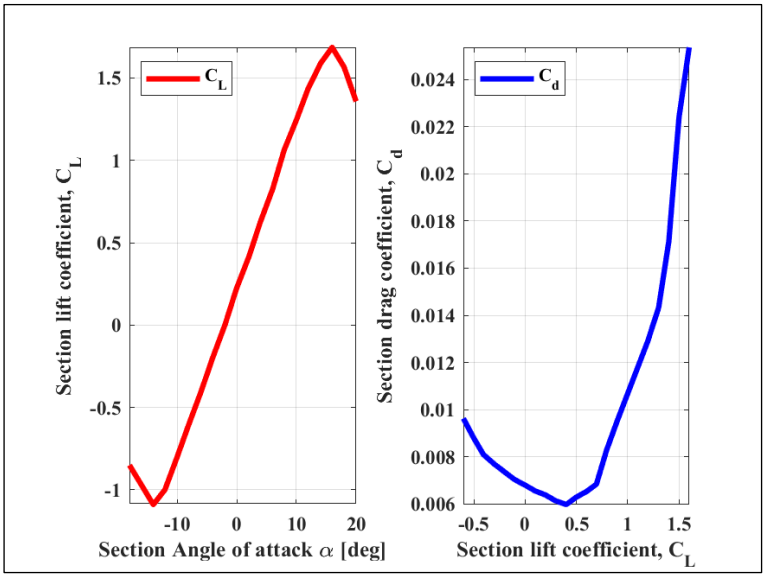

Figure 4.9. Lift and drag coefficient of NACA 2412 airfoil [73].

4.3.2. Propeller

The power P, torque M, and thrust T exerted by the propeller are computed by applying the Momentum Theory [71],[74] in different conditions of true speed v and rotational speed n related to the propeller shaft:

$$P = C_p \rho n^3 d^5 \tag{4.37}$$

$$M = C_q \rho n^2 d^5 \tag{4.38}$$

$$T = C_t \rho n^2 d^4 \tag{4.39}$$

where C_p is the power coefficient, C_q is the torque coefficient, and C_t is the thrust coefficient. The coefficients C_p, C_q, and $C_t$are evaluated through nonlinear maps [71] by knowing the advanced ratio J and the pitch of the propeller p.

$$J = \frac{v}{nd} \tag{4.40}$$

Geometric and inertial parameters related to the propeller are indicated in Table 4.3 [75].

Table 4.3. Parameters related to the propeller model [75].

Propeller Parameter	**Symbol**	**UoM**	**Value**
Diameter	d	(m)	1.70
Pitch	p	(deg)	22
Moment of Inertia	I_{prop}	(kgm^2)	0.35

4.3.3. Mission

In the automotive field, there is a multitude of standard mission profiles for testing both the performance and emission of hybrid engines [76]. Thus, following one of these missions, it is possible to obtain the results to compare them with other automotive propulsions. The aircraft mission plays a significant role in a new hybrid-propulsion and energy storage design, but generally, there aren't standard profiles to refer to. Generally, a different approach is considered in the aeronautical field, where only the operational points are optimized, such as take-off power, maximum continuous power, and 75% of maximum continuous power. The principal reason finds justification in the stationary mission of the aircraft if compared to the automotive urban cycle.

Usually, aeronautical engines are optimized for cruising speed at 75% of maximum continuous power. Therefore, the electric machine can work as a motor boost during brief flight maneuvers, such as take-off or climb when more power is required, while used as a generator for recharging the battery during descending and landing phases. For this reason, the mission is an essential requirement for a new hybrid propulsion concept design.

The proposed method is applied to a representative mission, able to highlight the strengths points of a hybrid propulsion system, where a short cycle that involves take-off, climb, and a brief cruise, followed by immediate descending and landing, such as "touch and go" used for

pilot training, or short-range mission typical of air-taxi applications. In the Table 4.4, the mission plane sequence is defined in terms of Aircraft speed for each mission interval [77].

Table 4.4. Mission plan sequence: input data [77].

Mission Sequence	Time Interval (s)	Duration (s)	Aircraft velocity (km/h)	Path angle γ (deg)	Angle of attack α (deg)	Altitude (m)
Take-off	0 - 48	48	137	0	12 - 8	0
Climb	49 - 233	184	155	2.5	8	0 - 330
Cruise	234 - 453	219	155	0	6	330
Descent	454 - 610	156	144	-1	6	330 - 220
Approach	611 - 710	99	153	0	6	220
Landing	711- 891	180	144	-1.7	6	220 - 0

This mission has been implemented in the Matlab/Simulink model to evaluate both the performance of the hybrid propulsion system and the developed control strategy. The mission profile in terms of altitude is displayed in Figure 4.10. The duration of the mission is about 15' minutes.

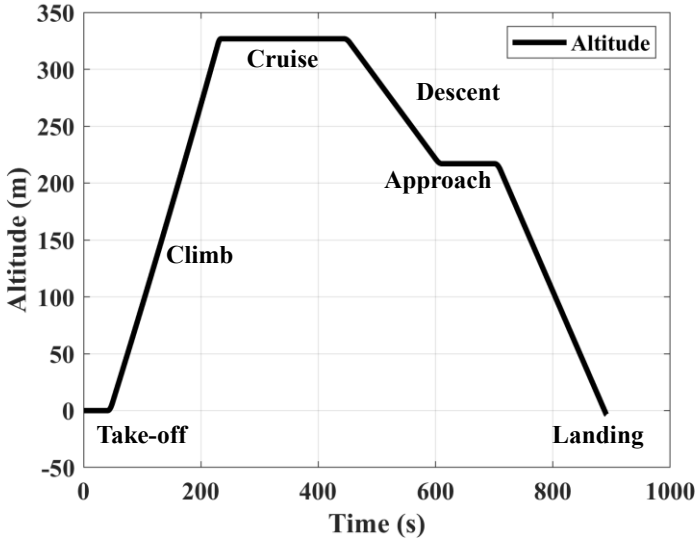

Figure 4.10. Altitude profile of the chosen short range mission [77].

Finally, the Global Hybrid-Electric Propulsion Aircraft Model designed in Matlab/Simulink has been shown in Figure 4.11. The required torque related to the propeller $PropTrqCmd$ is provided by a PID controller, employed to simulate the action of a real driver (i.e. Pilot) to control the aircraft's true speed, as shown in Figure 4.11 [77].

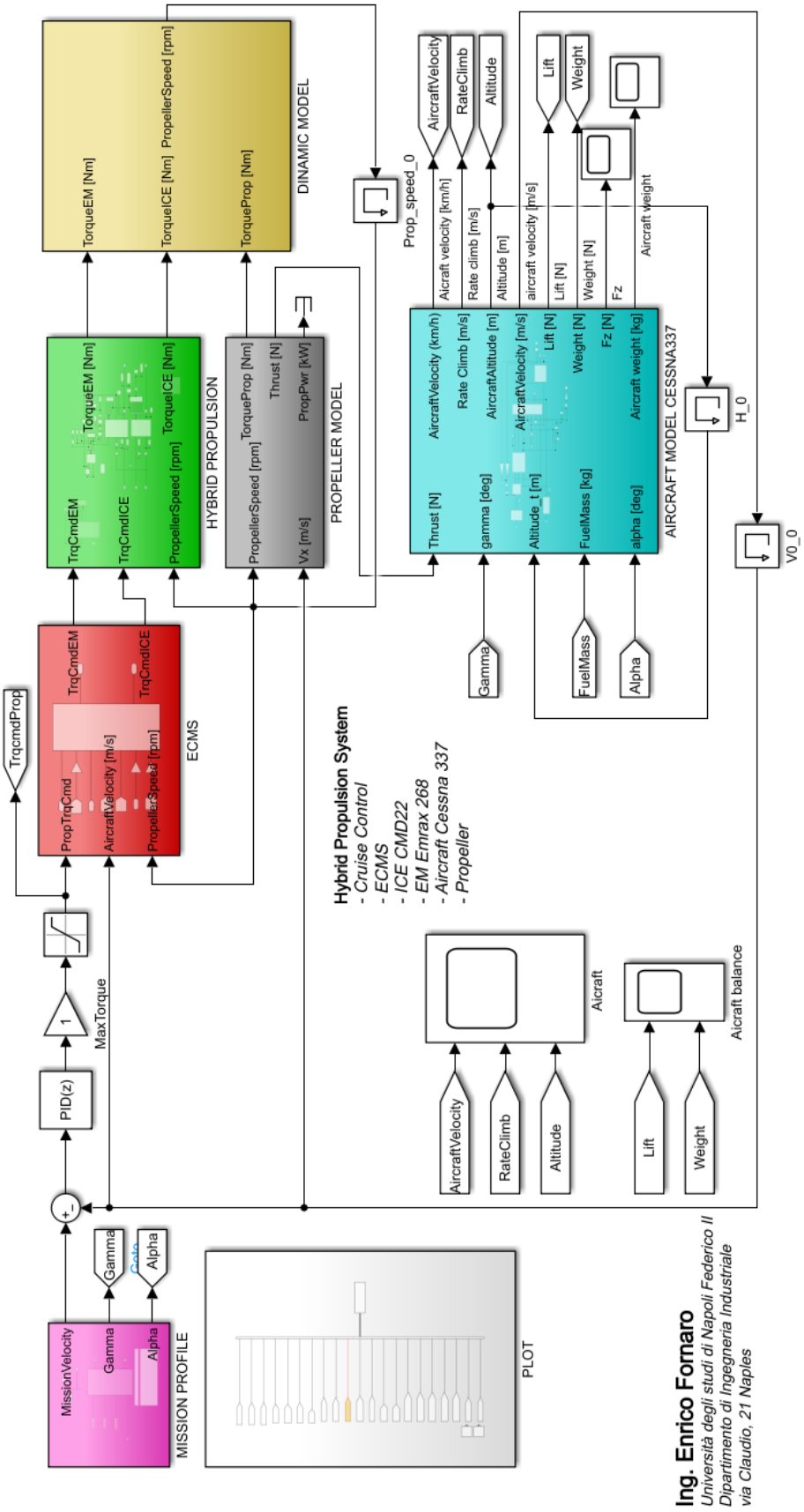

Figure 4.11. Global Hybrid-Electric Propulsion Aircraft Model in Matlab/Simulink.

4.4. Simulation Results

This section will present simulations conducted on a parallel hybrid-electric aircraft propulsion system controlled by an optimization strategy based on the minimization of equivalent fuel consumption (ECMS). Additionally, the model flexibility and ease of use, developed in Matlab/Simulink, have allowed for rapid analysis repetition, expanding the scope to other parallel hybrid propulsion configurations. For this purpose, in addition to the CMD22 internal combustion engine, another engine widely used in the general aviation sector, the Continental IO-360, has also been considered. This latter engine has been coupled with the electric machine EMRAX 268 in the same parallel hybrid propulsion architecture. Subsequently, the Degree of Hybridization DoH_P has been determined, taking into account the maximum continuous power of the electric motor at 2750 rpm, which is 62 kW. Table 3.1 in Chapter 3 provides the manufacturer-defined target performance for both internal combustion engines, while Table 4.5 lists the technical specifications of these engines, including the Degree of Hybridization. Finally, the obtained performance in both configurations will be compared with the conventional "*Fully-Thermal*" one consisting of a single Continental IO-360 thermal engine.

Table 4.5. ICE Technical Specifications.

Technical Specifications	**UoM**	**CONTINENTAL IO-360**	**CMD 22**
Bore	mm	112.7	100
Stroke	Mm	98.5	70
Displacement	cm^3	5899.3	2198
Compression ratio	-	85:1	9.7:1
Cylinder N°	-	6	4
Prop. drive ratio	-	1:1	1:2
Prop. driven rotation	-	Clockwise	Clockwise
Dry Weight	kg	158.7	77.6
Weight/Power	kg/Hp	0.756	0.657
Degree of Hybridization	-	0.28	0.4

The investigation has been carried out considering a total mission duration of 45 minutes, as shown in Figure 4.12, consisting of three repetitions of the air-taxi mission described in the previous section. Additionally, both control strategies have been compared under non-adaptive ECMS conditions and adaptive A-ECMS conditions. Moreover, the setup model parameters are indicted in Table 4.6.

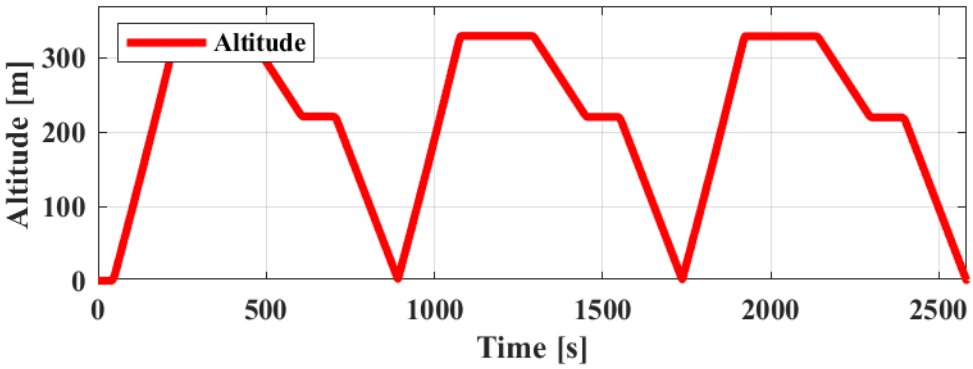

Figure 4.12. Altitude profile of the 3 short range mission repetition.

Table 4.6. Setup of model parameters.

Model Parameter	UoM	ECMS	A-ECMS
SoC_{min}	%	20	20
SoC_{max}	%	95	95
SoC_{target}	%	95	95
SoC_{ini}	%	95	95
s_0	-	3.385	3.385
k_P	-	0	0.1
k_I	-	0	0.02
$p(SoC)$	-	0÷2	0÷2
a	-	3	3
TPE_{factor}	-	6	6
$Constraint\ Penalty$	-	10^7	10^7
H_i	MJ/kg	43.5	43.5

In Figure 4.13, the simulation results considering only the Continental IO-360 thermal engine have been presented. Figure 4.13 (a) shows that the contribution of electric motor torque from the EMRAX 268 *"CmdEM"* is zero throughout the mission duration. The estimated fuel consumption for completing the mission is about 20 kg (Figure 4.13 (b)). Moreover, by applying Equation 3.19, have been calculated the primary energy expended, which amounts to 241.7 kWh. Furthermore, in Figure 4.13 (c), the mission points (in RPM-Torque) have been plotted on the specific fuel consumption plane of the Continental IO-360 engine. In this figure, the operating points are constrained by the propeller load and their distribution look like a quadratic curve.

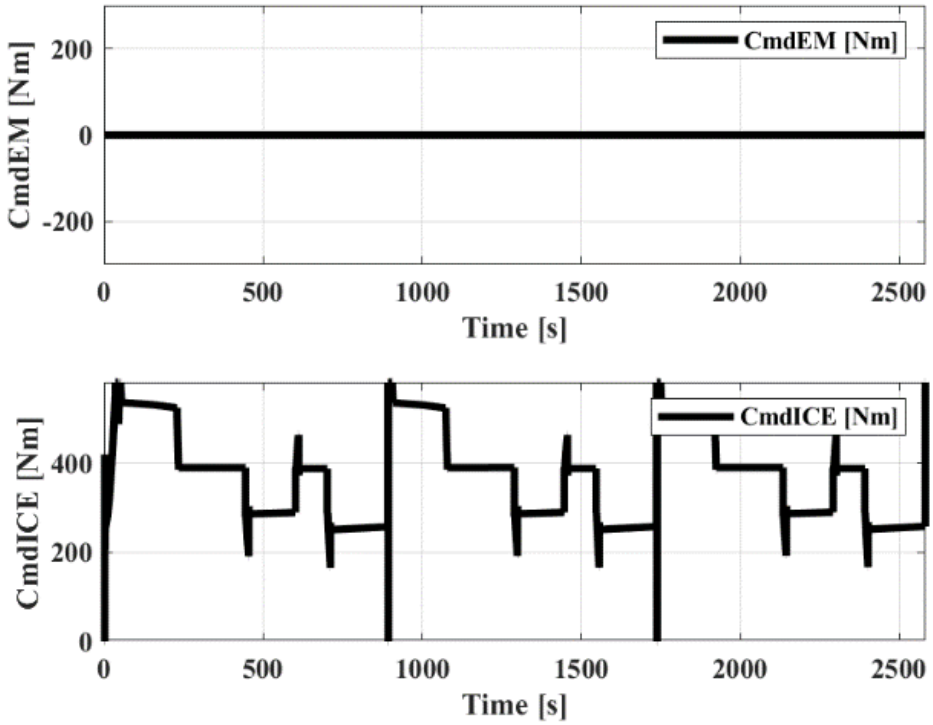
CmdEM [Nm]
200
0
-200
0
500
1000
1500
2000
2500
Time [s]
CmdICE [Nm]
400
200
0
0
500
1000
1500
2000
2500
Time [s]

(a)

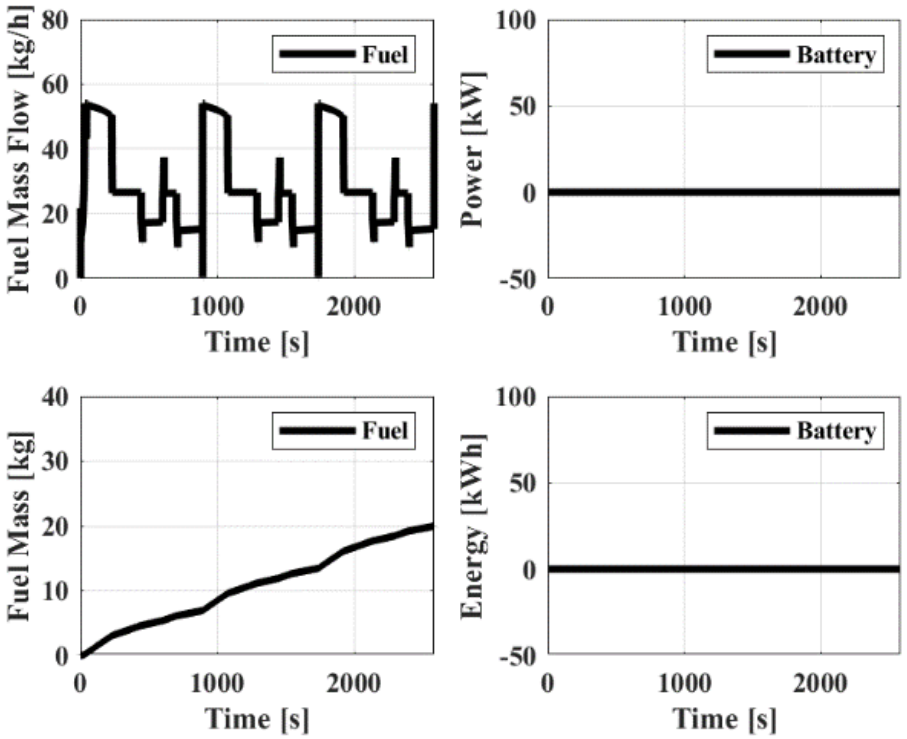
Fuel Mass Flow [kg/h]
80
60
40
20
0
Fuel
0
1000
2000
Time [s]
Power [kW]
100
50
0
-50
Battery
0
1000
2000
Time [s]
Fuel Mass [kg]
40
30
20
10
0
Fuel
0
1000
2000
Time [s]
Energy [kWh]
100
50
0
-50
Battery
0
1000
2000
Time [s]

(b)

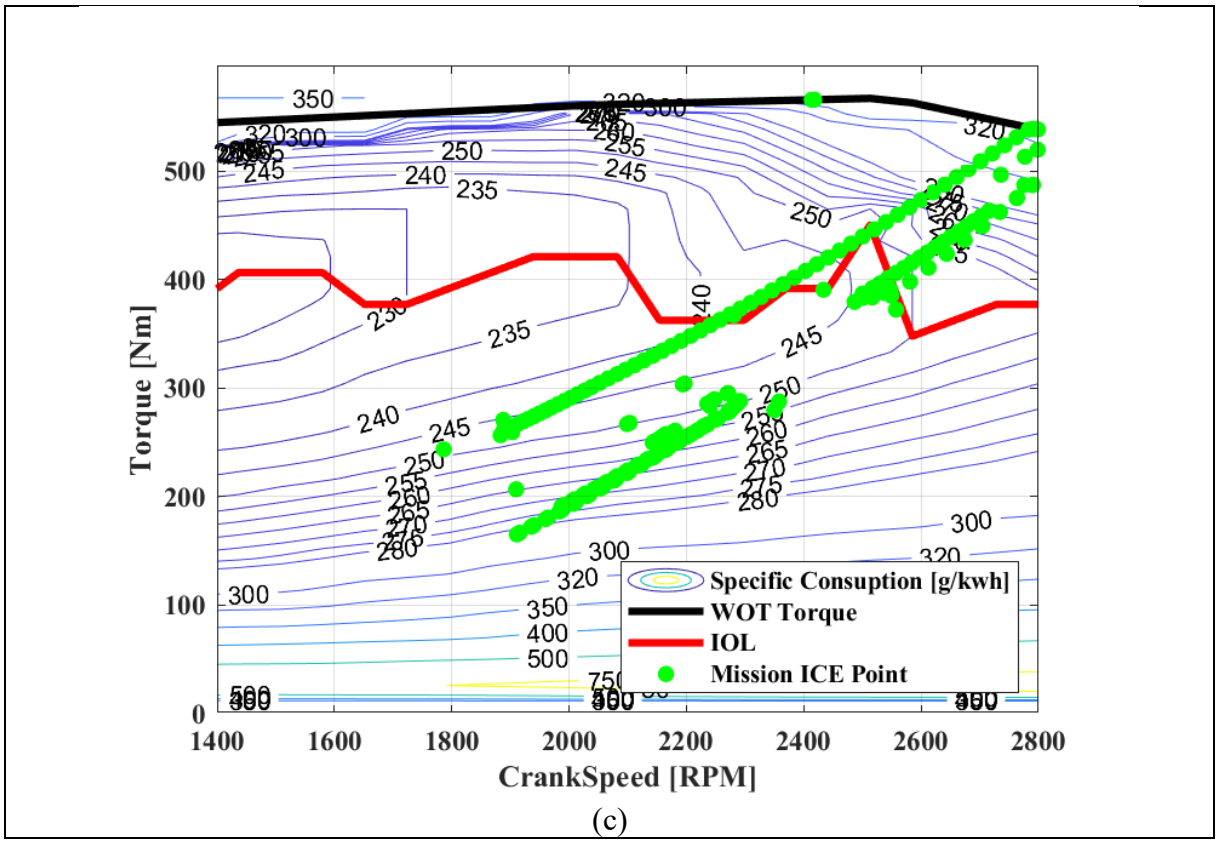

(c)

Figure 4.13. Results for "*Fully-Thermal*" (Continental IO-360) propulsion.

In Figure 4.14 the simulation results of the HEPS configuration equipped with Continental IO-360 and the CMD 22 engine, both coupled with the electric machine EMRAX 268, have been reported. These HEPS have been controlled by a non-adaptive optimization strategy based on ECMS, and the equivalent factor is considered constant during the mission, equal to $s_0 = 3.385$. In Figures 4.13 (a), the contribution of the electric motor EMRAX 268 *"CmdEM"* is visible working as a motor when the torque is positive and as a generator when the torque is negative. The HEPS configuration equipped with the CMD 22 engine shows in Figures 4.13 (a) that the thermal engine reaches and maintains the maximum torque limit *"CmdICE"* approximately 350 Nm referred to the propeller shaft (175 Nm if referred to the crankshaft Figures 4.14 (a2)), throughout the mission duration. However, in neither HEPS configuration, the final battery energy and also state of charge is restored to the initial 95%, as shown in Figures 4.13 (b, c). The primary energy needed to complete the mission with the Continental IO-360 engine is 221.3 kWh and 166.1 kWh for the configuration with CMD22. The total energy is calculated by applying the Equations discussed in Chapter 3 (3.18, 3.19, and 3.20). Both values are approximately 8.4% and 31.3% lower than the "*Fully-Thermal*" case, respectively, as indicated in Table 4.7. The primary energy reduction is ascribable to the *"better quality"* of the electrical energy produced by the National Thermoelectric Plants used to restore

the final battery charge level to the initial one. Therefore, for the non-adaptive ECMS-based control configuration, it is necessary to plan a battery recharging at the end of the mission. Therefore, the hybrid-electric propulsion system must be designed as a *"Plug-in"*. Moreover, Figure 4.14 (d) shows the trends of the equivalent specific consumption s, which is constant throughout the mission duration, and the values of the Hamiltonian.

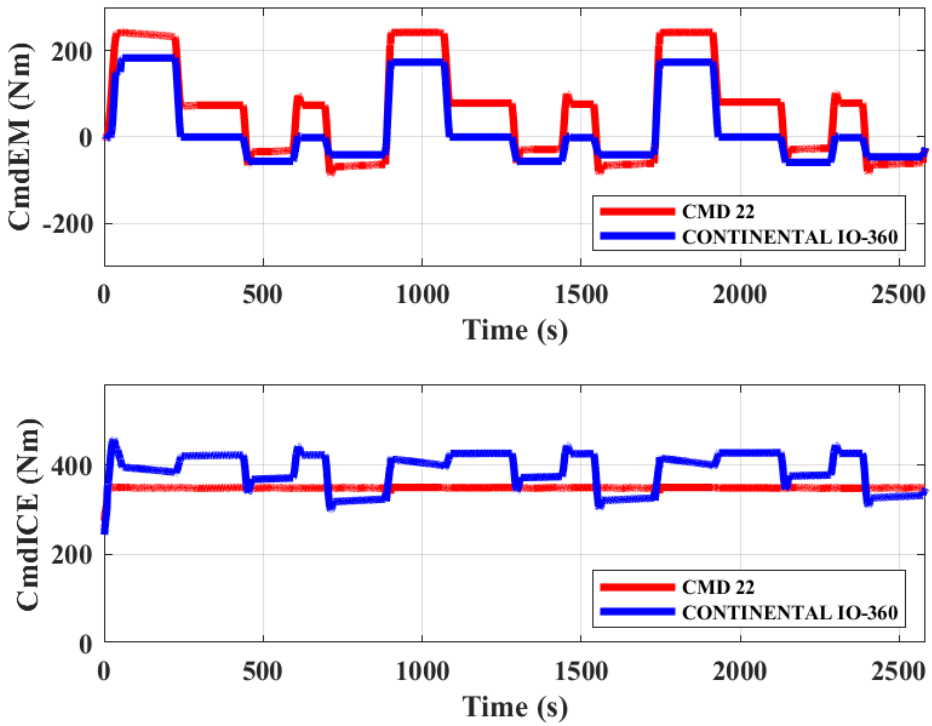

(a)

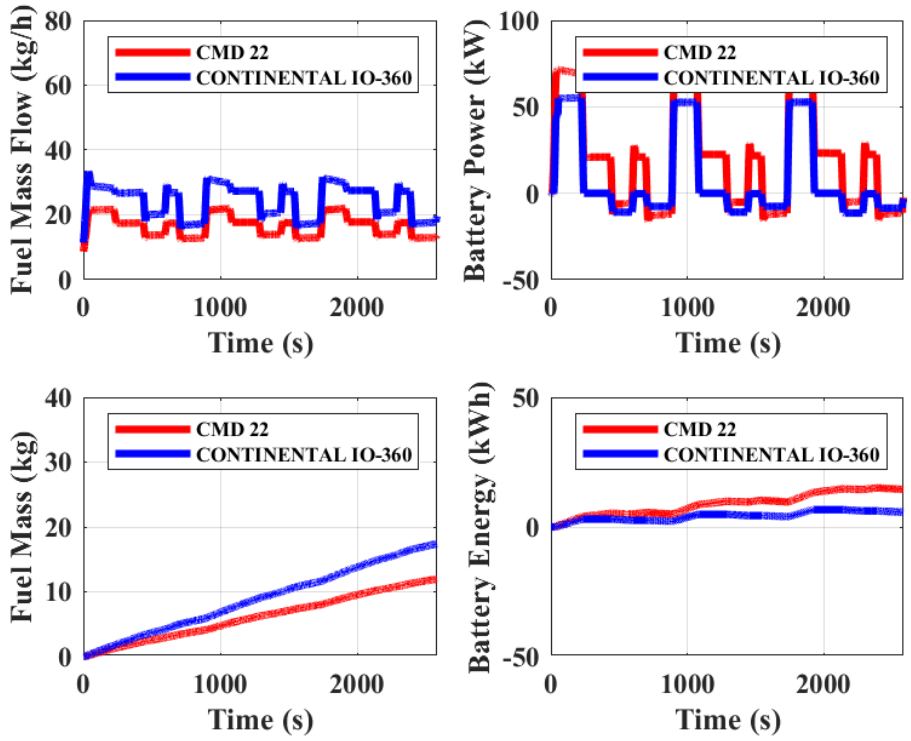
Fuel Mass Flow (kg/h)
Battery Power (kW)
Fuel Mass (kg)
Battery Energy (kWh)
Time (s)
CMD 22
CONTINENTAL IO-360

(b)

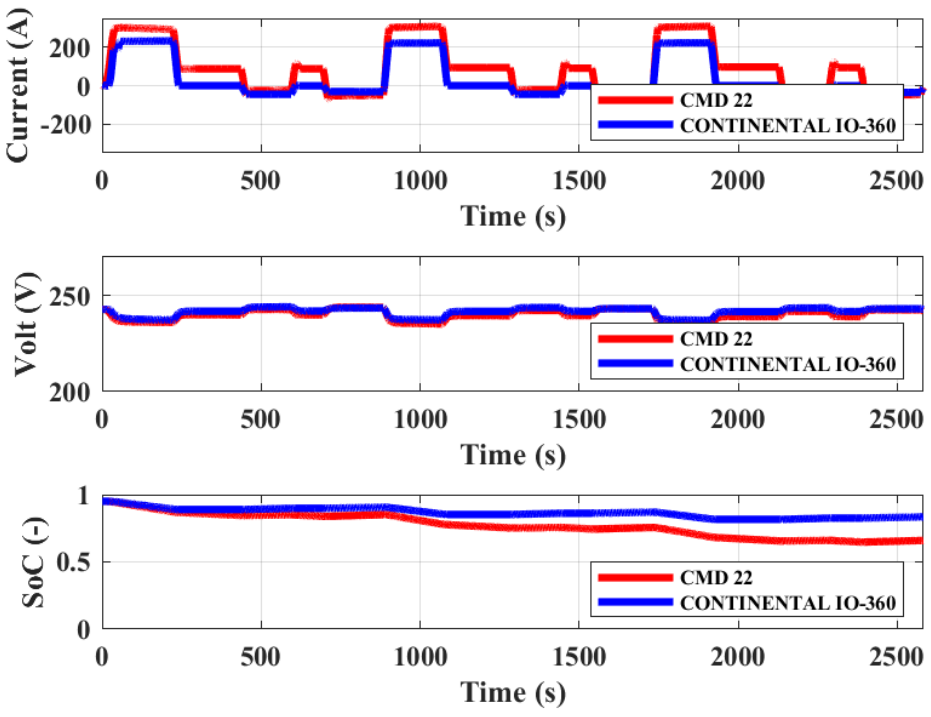
Current (A)
Volt (V)
SoC (-)
Time (s)
CMD 22
CONTINENTAL IO-360

(c)

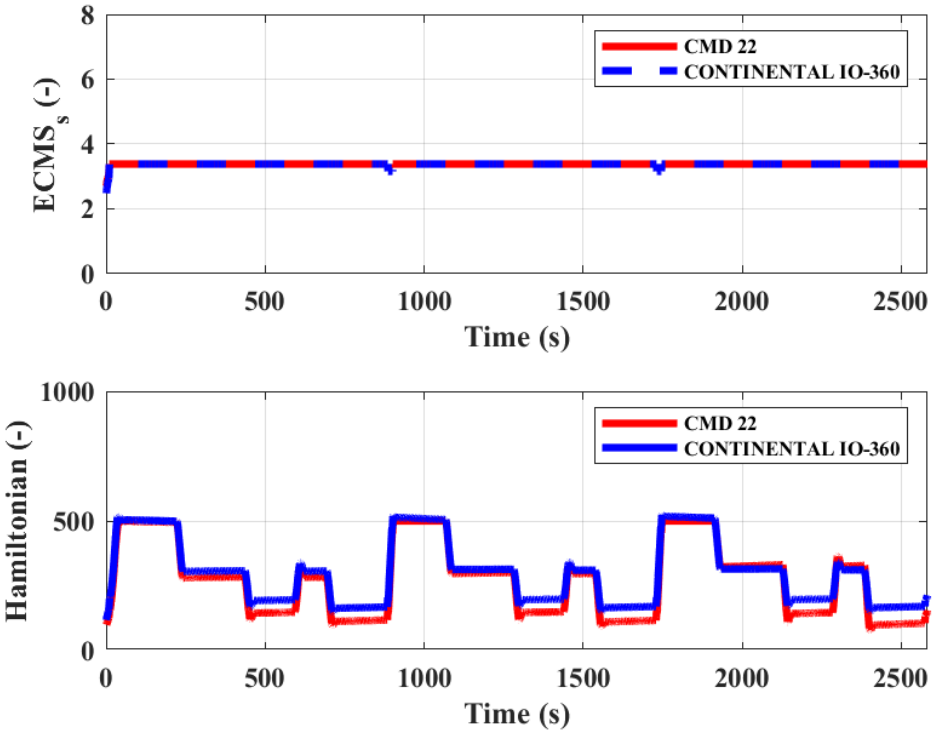

(d)

Figure 4.14. Results for HEPS (CMD22 and Continental IO-360) with ECMS control.

Furthermore, in Figure 4.15 (a1-a2), mission points (in RPM-Torque) on the specific fuel consumption plane of the both engines are depicted. In this Figure, the operating points are not directly constrained by the propeller load, as was the case for the conventional configuration. In fact, the operating points for the Continental IO-360 engine are allocated around the curve of minimum specific fuel consumption defined as the "*Ideal Operating Line*" (red curve in figure). Conversely, for the CMD 22 engine, the operative points are distributed around the maximum torque curve because the chosen value of equivalent specific fuel consumption $s_0 = 3.385$ is a limit value for this configuration able to avoid the fast battery discharge.

CONTINENTAL IO-360 + EMRAX 268 ECMS	CMD 22 + EMRAX 268 ECMS
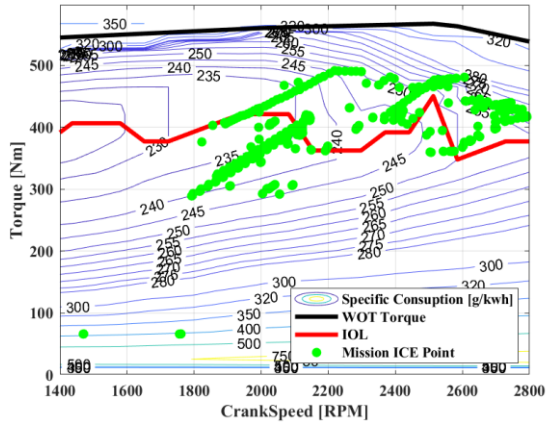	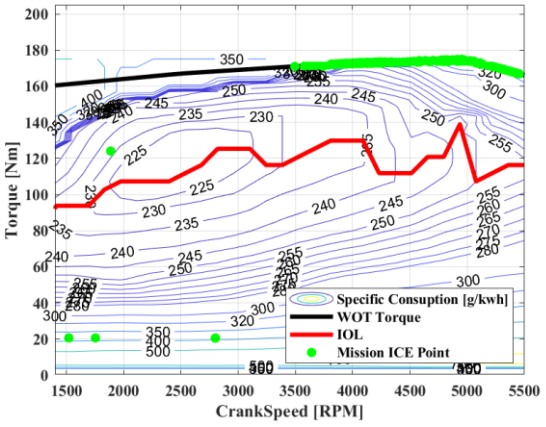
(a1)	(a2)
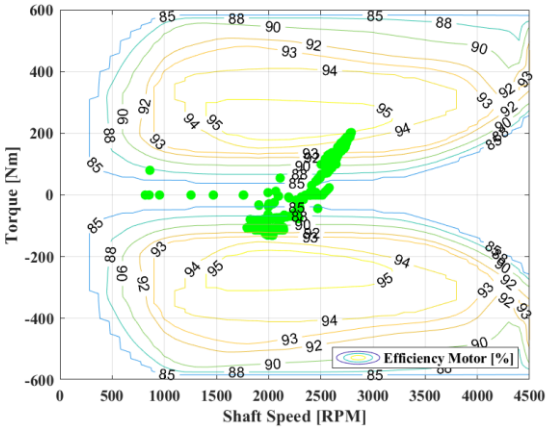	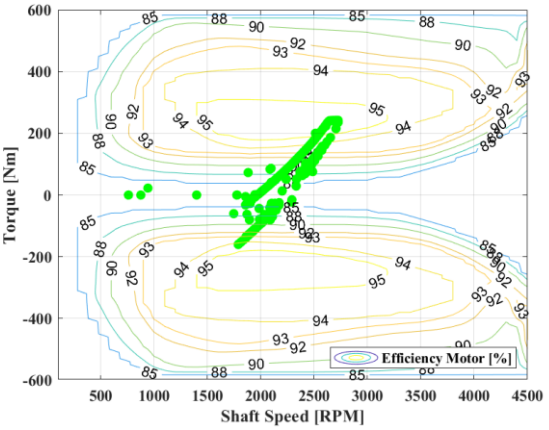
(b1)	(b2)

Figure 4.15. Results for HEPS on efficiency-map using ECMS control.

In Figure 4.16 the simulation results of the HEPS configuration equipped with Continental IO-360 and the CMD 22 engine, both coupled with the electric machine EMRAX 268, have been reported. These HEPS have been controlled by an adaptive optimization strategy based on A-ECMS, and the equivalent factor is controlled through a PI during the mission within the interval $1 < s < 4.6$.

In Figures 4.15 (a), the contribution of the electric motor EMRAX 268 *"CmdEM"* is visible working as a motor when the torque is positive and as a generator when the torque is negative. The HEPS configuration equipped with the CMD 22 engine shows in Figures 4.15 (a) that the thermal engine reaches and maintains the maximum torque limit *"CmdICE"* approximately 350 Nm referred to the propeller shaft (175 Nm if referred to the crankshaft Figures 4.16 (a2)), throughout the mission duration, unable to restore the final state of charge of the battery to the

initial one. Only the configuration with the Continental IO-360 engine is able to restore the final battery energy and state of charge to the initial 95%, as shown in Figures 4.15 (b, c).

The primary energy needed to complete the mission with the Continental IO-360 engine is 227.2 kWh and 166.9 kWh for the configuration with CMD22. The total energy is calculated by applying the Equations discussed in Chapter 3 (3.18, 3.19, and 3.20). Both values are approximately 6% and 31% lower than the "*Fully-Thermal*" case, respectively, as indicated in Table 4.7. The primary energy reduction in HEPS with CMD22 configuration is ascribable to the *"better quality"* of the electrical energy produced by the National Thermoelectric Plants used to restore the final battery charge level to the initial one. In this case, the propulsion equipped with the Continental IO-360 engine can restore the final state of charge of the battery equal to the initial one, thanks to the A-ECMS strategy.

Therefore, the hybrid-electric propulsion system equipped with Continental IO-360 can be designed as a *"Full-Hybrid"* for the chosen mission. Moreover, Figure 4.16 (d) shows the trends of the equivalent specific consumption s, and the values of the Hamiltonian. The adaptation law is based on a proportional-integral (PI) controller (Equation 4.28), and the s value increases when the battery state of charge decreases.

In the HEPS configuration, equipped with a CMD22 engine, the value of s reaches the upper limit. In this case, the chosen thermal engine is undersized. Differently, for the HEPS configuration with Continental IO-360 engine, a slow increase of the equivalent specific consumption is obtained. It is observed from Figure 4.16 (a) that the torque demand of the electric motor "CmdEM" during recharging increases from the second repetition of the mission, and also the recharging battery power and current increases as shown in Figures 4.15 (b, c) respectively.

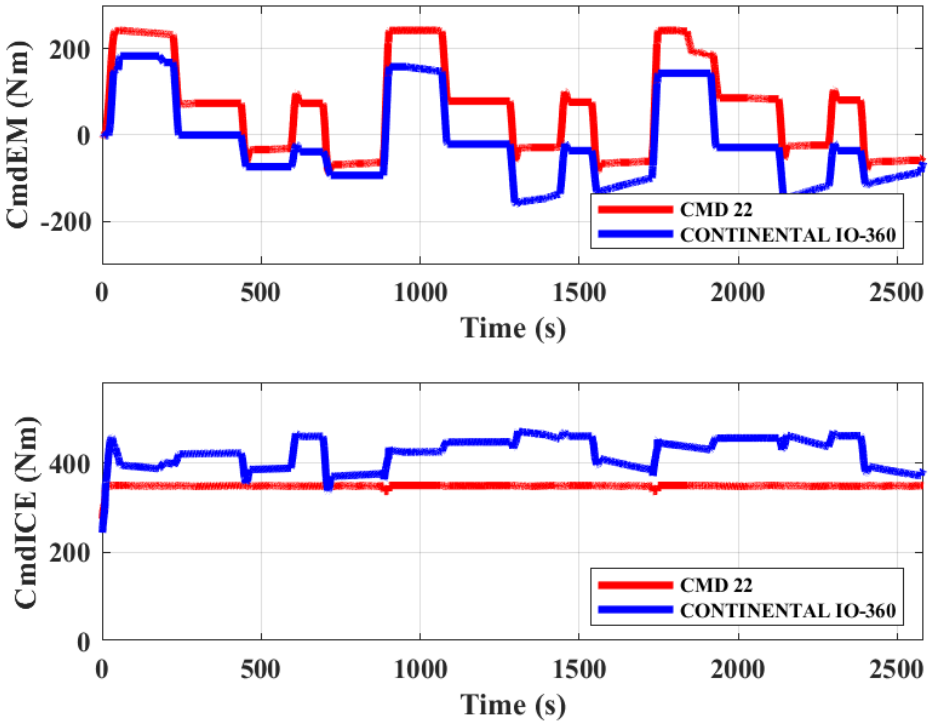
CmdEM (Nm)
200
0
-200
0
500
1000
1500
2000
2500
Time (s)
CMD 22
CONTINENTAL IO-360
CmdICE (Nm)
400
200
0
0
500
1000
1500
2000
2500
Time (s)
CMD 22
CONTINENTAL IO-360

(a)

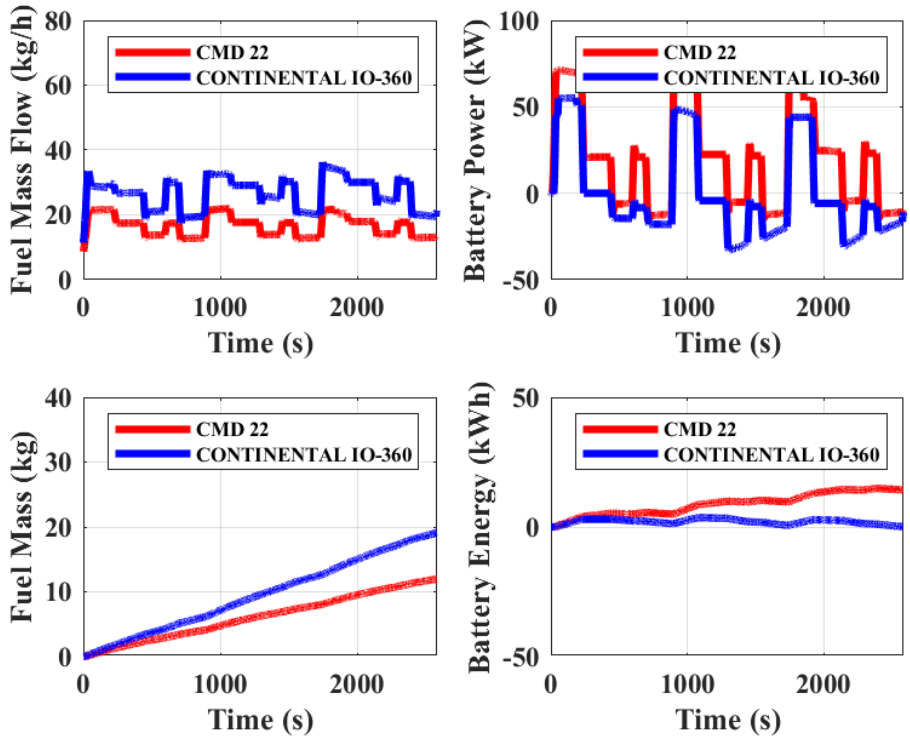
Fuel Mass Flow (kg/h)
80
60
40
20
0
0
1000
2000
Time (s)
CMD 22
CONTINENTAL IO-360
Battery Power (kW)
100
50
0
-50
0
1000
2000
Time (s)
CMD 22
CONTINENTAL IO-360
Fuel Mass (kg)
40
30
20
10
0
0
1000
2000
Time (s)
CMD 22
CONTINENTAL IO-360
Battery Energy (kWh)
50
0
-50
0
1000
2000
Time (s)
CMD 22
CONTINENTAL IO-360

(b)

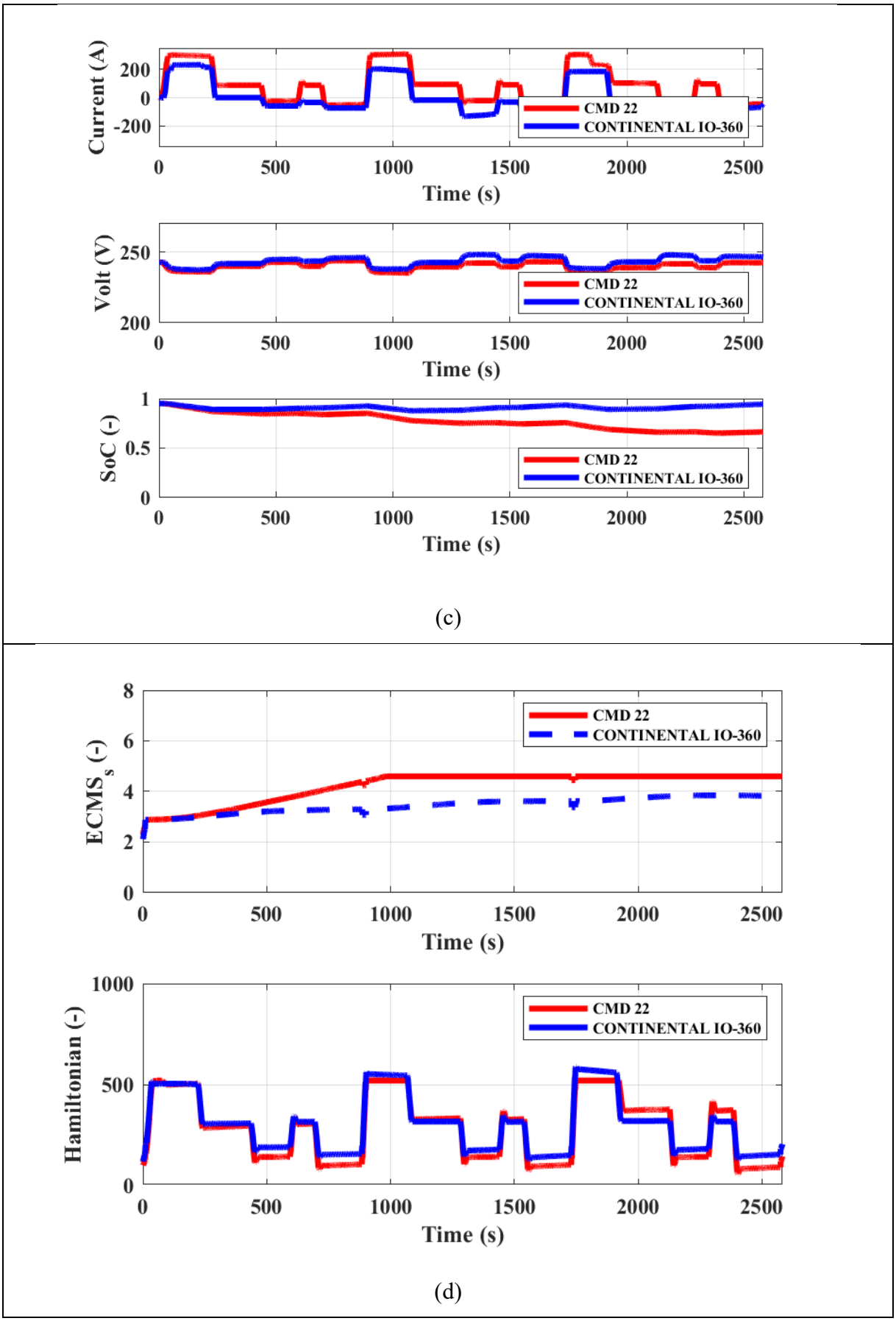

Figure 4.16. Results for HEPS (CMD22 and Continental IO-360) with A-ECMS control.

Furthermore, in Figure 4.17 (a1-a2), mission points (in RPM-Torque) on the specific fuel consumption plane of the engines are depicted. In this Figure, the operating points are not directly constrained by the propeller load, as was the case for the conventional configuration. In fact, the operating points for the Continental IO-360 engine are allocated around the curve of minimum specific fuel consumption defined as the "*Ideal Operating Line*" (red curve in figure). Conversely, for the CMD 22 engine, the operative points are distributed around the maximum torque curve because the A-ECMS strategy pursues the battery recharging requirement at the end of the mission.

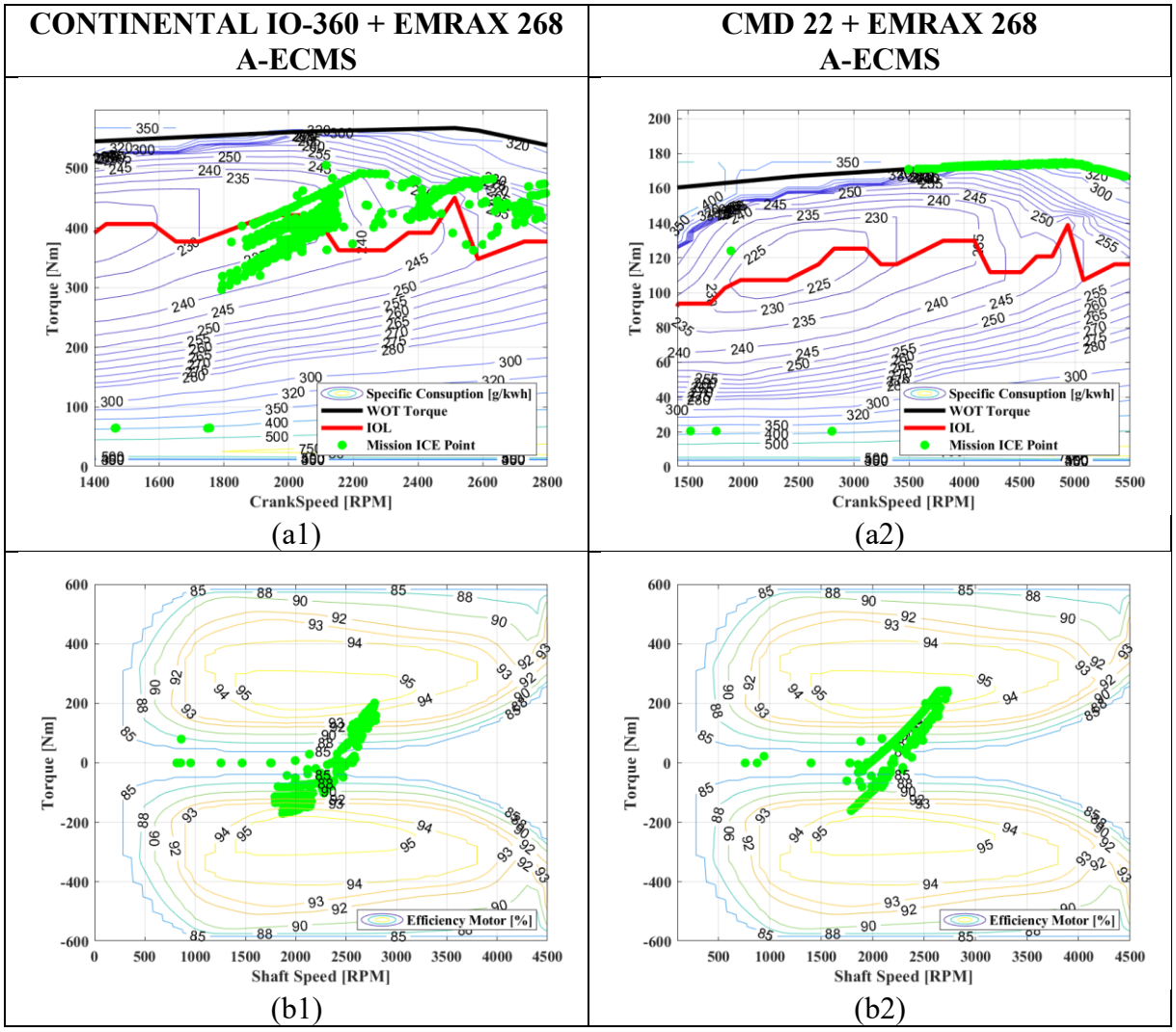

Figure 4.17. Results for HEPS on efficiency-map using A-ECMS control.

The mass of CO_2 gas emission $M_{CO_2}^{total}$ has been estimated in all cases by the sum of directly CO_2 emission by fuel consumption $M_{CO_2}^{fuel}$ and indirect emission linked to grid energy consumption necessary to charge the battery $M_{CO_2}^{battery}$.

$$M_{CO_2}^{total} = M_{CO_2}^{fuel} + M_{CO_2}^{battery} \quad (3.41)$$

$$M_{CO_2}^{fuel} = m_{fuel} \cdot 3.16 \quad (3.42)$$

$$M_{CO_2}^{battery} = \Delta E_{battery} \cdot 444.4 \quad (3.43)$$

where, m_{fuel} is the mass of fuel consumption, assuming the average chemical formula of AvGas 100 to be C_8H_{15}, the approximated amount of Carbon Dioxide emitted in the atmosphere for each kilogram of fuel is $3.16\, kgCO_2/kg_{fuel}$ [78]. $\Delta E_{battery}$ is the battery energy consumption, and the value $444.4\, gCO_2/kWh$ is referred to the Italian National Electricity Grid efficiency (2020) [55]. The primary energy calculation is referred to the equations in Chapter 3 Equations 3.18 to 3.20.

Table 4.7. Simulation Results.

		CONTINENTAL IO-360 + EMRAX 268 A-ECMS	**CONTINENTAL IO-360 + EMRAX 268 ECMS**	**CMD 22 + EMRAX 268 A-ECMS**	**CMD 22 + EMRAX 268 ECMS**	**CONTINENTAL IO-360 Fully thermal**
Degree of Hybridization		0.28	0.28	0.4	0.4	0
$SOC_{initial}$	%	95	95	95	95	-
SOC_{final}	%	95	87.7	67.8	67.3	-
ΔSOC	%	0	7.3	27.2	27.7	-
$\Delta E_{battery}$	kWh	0	3.4	12.8	13.0	-
m_{fuel}	kg	18.8	17.8	11.9	11.8	20.0
$E_p^{battery}$	kWh	0	6.2	23.1	23.5	-
E_p^{fuel}	kWh	227.2	215.1	143.8	142.6	241.5
E_p^{tot}	kWh	227.2	221.3	166.9	166.1	241.5
$M_{CO_2}^{battery}$	kg	0	1.5	5.7	5.8	-
$M_{CO_2}^{fuel}$	kg	59.4	56.2	37.6	37.3	63.2
$M_{CO_2}^{tot}$	kg	59.4	57.8	43.3	43.1	63.2
$m_{fuel}\ improv$	%	6.0	11.0	40.5	41.0	-
$E_p^{tot}\ improv$	%	6.0	8.4	31.0	31.3	-
$M_{CO_2}^{tot}\ improv$	%	6.0	8.6	31.5	31.8	-

The simulation results, reported in Table 4.7, show an efficiency improvement in all HEPS configurations. In fact, in all HEPS cases, the reduction of the total primary energy consumption E_p^{tot} between 6 ÷ 31.3 %, and therefore, a reduction of CO_2 emissions $M_{CO_2}^{tot}$ released into the atmosphere to perform the same mission compared to the "*Fully-Thermal*" configuration.

The hybrid-electric propulsion configurations equipped with the CMD22 engine (with a higher Degree of Hybridization $DoH_P = 0.4$) yield almost similar results for both optimization strategies proposed, ECMS and A-ECMS, as the Adaptive strategy has little impact on the overall system operation. Indeed, the size of the CMD22 internal combustion engine is too small, and the torque contribution it provides throughout the mission duration, in both cases, is always close to the maximum available torque value. These results highlight in both strategies the inability of the internal combustion engine to recharge the battery, as the final state of charge is always lower than the initial one. This system is configured as a "*range extender*" propulsion, where the contribution of the internal combustion engine extends the range and operating time of the hybrid system before the battery is depleted. Therefore, with such a high Degree of Hybridization, the hybrid-electric propulsion system must be designed to perform missions similar to the one considered with a "*Plug-In*" charging system, where battery pack recharging is ensured by connecting to the electric grid once landed.

A different result can be achieved when the hybrid-electric propulsion system has a lower Degree of Hybridization $DoH_P = 0.28$. In this case, the hybrid-electric propulsion system is equipped with the Continental IO-360 engine, and it is possible to recharge the battery at the end of the mission, thus restoring the final state of charge to the initial level when the adaptive configuration of the A-ECMS control strategy is chosen. The adaptive control strategy increases the weight of the specific equivalent consumption of the chemical energy stored in the battery (making it more precious). The Continental IO-360 engine has a greater torque availability when compared to the CMD 22 engine and, therefore, more power availability to recharge the battery. Moreover, this hybrid configuration, equipped with A-ECMS control, can be designed as a "*Full-Hybrid*" when the battery recharge is not necessary for the aircraft once it lands.

When the ECMS strategy is adopted, the final battery state of charge isn't restored to the initial one. The main reason regards the specific equivalent consumption value that remains fixed during all mission time, involving non-adaptive management of the engines.

However, these configurations allow for recharging totally or partially the battery at the end of the mission while simultaneously reducing fuel consumption and CO_2 emissions compared to the conventional setup. This achievement is possible thanks to the electric machine's mechanical coupling and its work when being useful. In fact, when the thermal engine is coupled directly to the propeller ("*Fully-thermal"* case), it is not simple to optimize its operation, as can be seen in the specific consumption map in Figure 4.13, because the propeller imposes a constraint. Figure 4.13 shows that the operating points (in green) are distributed along a parabolic curve, sometimes reaching high specific consumption regions. Therefore, the

hybrid-electric configuration helps to improve the thermal engine efficiency, enabling it to work in more efficient zones as show in Figure 4.15 (a1) and Figure 4.17 (a1).
All of these considerations are true for missions like the chosen one. Indeed, when a new hybrid-electric propulsion system must be designed, the mission plan is a fundamental requirement.
Generally, the cruise flight phase in the general aviation field accounts for approximately 90% of the entire mission. Therefore, considering the obtained simulation results, an aeronautical hybrid-electric propulsion system can be designed as follows:

- *Plug-In* – More electric motor power is needed during the cruise phase, making it impossible to fully recharge during the short mission phases of runway approach and landing. Therefore, it is necessary to consider a "*Plug-in"* configuration able to recharge the battery on the ground.
- *Full-Hybrid* – The electric motor power is available as a boost during mission phases with higher power demand (e.g., take-off, climb, turns), and the EM works as a generator during cruising phases. Therefore, the internal combustion engine can recharge the battery during the cruise and landing phases, restoring the battery's initial charge level if a control energy strategy is implemented.

Point out of overall efficiency and environmental impact, "*Plug-In"* and "*Full-Electric*" configurations certainly offer an advantage that can only increase when considering future improvements in the efficiency of the National Electric Grid and the energy mix of the National Power Plants with an increase of the renewable share. However, it's important to note that these configurations face challenges due to the significant size and weight of the battery pack, which strongly limits their operational range.
On the other hand, the scenario is different for "*Full-Hybrid*" configurations. These HEPS configurations solve the problem related to the limited operative range, achieving an improvement in overall efficiency of around 6%. Generally, the efficiency improvement is not high because the flight missions often involve long steady-state phases with few load variations. This configuration makes life difficult for hybrid-electric propulsion systems, which usually gain greather efficiency points by assisting the internal combustion engine during recurring transient phases (i.e., as in the automotive field).

Chapter 5

5. EXPERIMENTAL REAL-TIME EVALUATION OF THE CONTROL STRATEGIES

Abstract

This chapter describes an experimental activity on the HEPS prototype carried out to test the real-time control A-ECMS strategies. For this purpose, a short-duration mission has been chosen to represent the typical aviation maneuvers generally performed by a pilot (i.e., Take-off, climb, cruise, and landing).

The first paragraph will discuss the hardware setup needed to control the HEPS engines. For this purpose, the ICE and the EM commanded torque signals calculated by the A-ECMS control strategy have been converted into actuation signals sent to each motor. The ICE torque command signal is sent to a linear actuator using a dedicated driver connected by wire to the throttle body. Moreover, the EM torque command signal is sent to the inverter controller through a CAN bus network.

The results show the capability of the A-ECMS to control in real-time the hybrid electric system splitting quickly the engine command and at the same time following the pilot imposed required torque.

5.1. Hardware set-up for Real-Time configuration with A-ECMS

The Hybrid Electric Propulsion System prototype designed for testing activities and equipped at the engine test bed is composed of an ICE CMD22 and an EM EMRAX 268 LV connected to the inverter GVI-H650 supplied by battery simulator ITECH IT6018C-500-90. This HEPS has been controlled in real-time through the minimization consumption strategy (A-ECMS), able to split the required torque at both Engines.

The A-ECMS strategy has been designed in a Matlab/Simulink environment (as described in the previous chapter). This strategy runs on a PC Notebook connected to seven inputs and two control outputs. The following paragraphs describe the physical connections between the Software and the Hardware consisting of two actuators for controlling the motors.

5.1.1. Torque Command ICE – Throttle signal configuration

The CMD 22 throttle body is driven by a steel cable connected to a throttle lever in the aircraft cabin. This control system does not lend itself to integrated electronic management of the hybrid-electric powertrain, so controlled implementation is required. For this purpose, a linear actuator LACT4P-12V-5 with feedback has been used to control the throttle body. This actuator is connected mechanically to the steel cable and electronically to the driver motor board L298N controlled by Arduino Mega microcontroller. The electrical wiring connections are indicated in Table 5.1 and shown in Figure 5.1. The driver L298N has been designed to control the DC motor and stepper motor, and the function is to amplify and manage control signals from a microcontroller, like Arduino, able to control the connected motors [79]. The main functions and features of the L298N board are:

- *H-Bridge Driver* – An H-bridge driver is a circuit that allows you to control the direction and speed of a DC motor.
- *Direction Control* – The H-bridge driver allows you to reverse the motor's rotation direction, enabling the motor to turn forward or backward.
- *Speed Control* – You can adjust the speed of DC motors by varying the pulse width of Pulse Width Modulation (PWM) signals sent to the L298N board from a microcontroller. This feature allows for precise motor speed control.

The linear actuator LACT4P-12V-5 used in this work is equipped with a feedback stroke position necessary for better controlling the throttle body. Therefore, the feedback PIN 3 (CYAN) has been connected to Analog Input A0 of the Arduino Mega. The digital control pins of the Arduino Mega D13 and D4 are connected to the IN 1 and IN 2 pins of the L298N board. These pins will be used to control the direction and speed of the motors. Moreover, the external power supply (12V - GND) has been connected to the L298N supply terminal block, and the output terminal blocks OUT 1 and OUT 2 are connected to the linear actuator supply.

Table 5.1. Wiring connections.

Arduino Mega	Linear Actuator	L298N
		Power Supply (12V)
5V	PIN1 (RED)	VCC (5V)
GND	PIN2 (BLACK)	GND
A0	PIN3 (CYAN) Fbk	
	PIN4 (BLACK)	OUT 1
	PIN5 (RED)	OUT 2 (12V)
D9		ENABLED
D13		IN 1
D4		IN 2

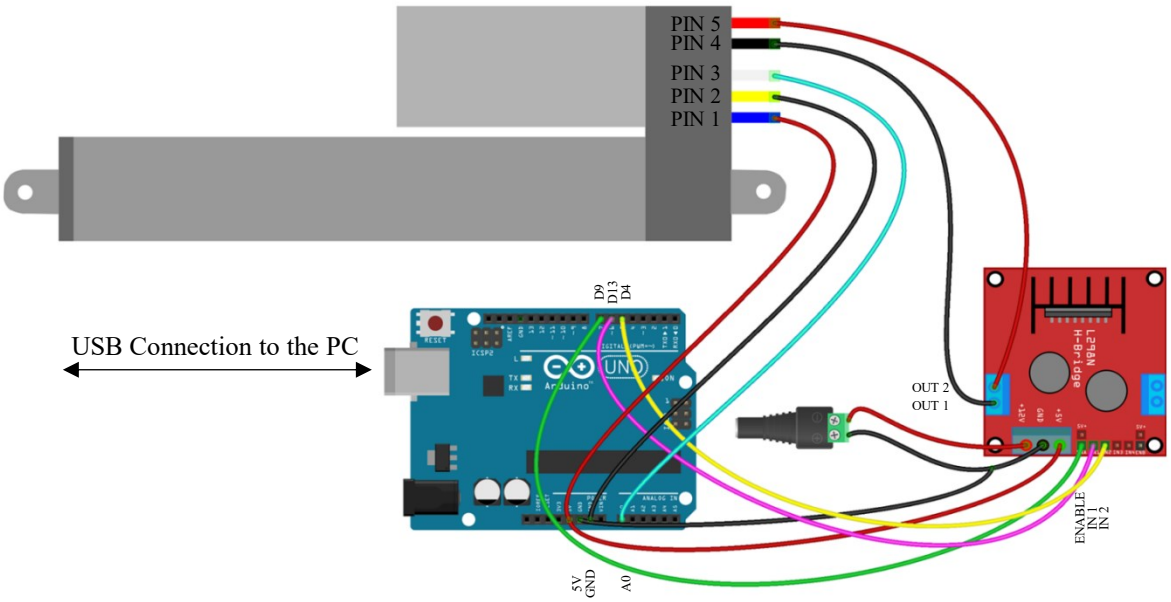

Figure 5.1. Linear Actuator Connections with Feedback to Arduino and L298N Driver.

In Matlab/Simulink has been written the Arduino code able to read the feedback from the linear actuator and uses the control pins to manage the direction and speed of the DC motor based on the position feedback [80]. The Arduino Mega control block is shown in Figure 5.2.

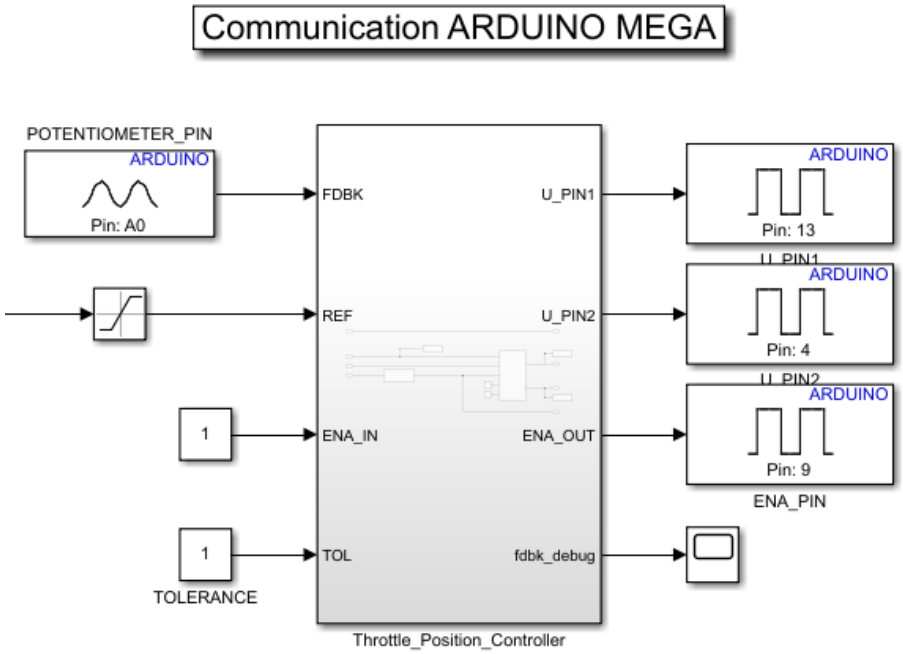

Figure 5.2. Arduino Mega control block in Matlab/Simulink.

5.1.2. Torque Command EM – CAN bus J1939 configuration

The EMRAX 268 LV Command Torque is driven by IQAN-MD4-T1E2 Display connected to Inverter GVI-H650 through CAN bus communication (Master-to-Slave connection). Differently from the throttle body, this control system lends good itself to integrated electronic management of the hybrid-electric powertrain using the CAN bus communication protocol J1939, but a different Master-to-Slave connection is required. For this purpose, the IQAN-MD4-T1E2 Display has been disconnected from the CAN bus network and replaced with the PC notebook connected to the CAN bus through the Kvaser Hs v2 USB device.

In Matlab/Simulink, a program for communication CAN J1939 has been developed, capable of reading and writing signals transmitted on the bus. The message encoding database is called "*test.dbc*" where all messages have been defined with specific addresses.

The code has been composed of two main blocks: the CAN Receive block to ensure the measure of the ECMS Input variable (i.e., Propeller speed, EM Speed, ICE Speed, Battery Volt) and the CAN Transmit block to send the Torque Command to the EM. The ECMS input Airspeed velocity is set equal to one at this stage. Moreover, the Battery SoC has been calculated by applying the equation 2.5 (in Chapter 2). The CAN bus J1939 control blocks are shown in Figure 5.3 [81].

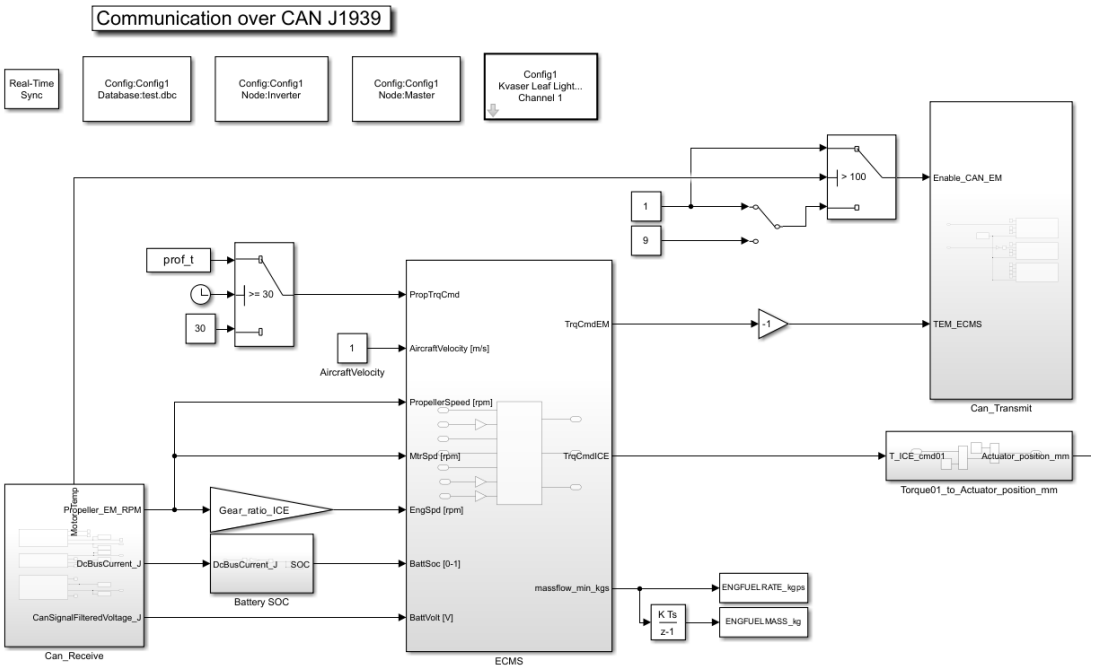

Figure 5.3. CAN bus J1939 Receive and Transmit blocks in Matlab/Simulink.

Figure 5.4 shows the global code used to manage the HEPS motors in real-time. The essential block adopted in Matlab/Simulink code is the "Real-Time Sync". This block is able to synchronize the simulation time based on the PC clock to the real one. In this way, the "Real-Time Sync" ensures that the simulation proceeds synchronized to the real time. The discretization time step has been set to 0.05 seconds. This time has been tested and considered acceptable to ensure good ICE and EM control together with a limited computational cost.

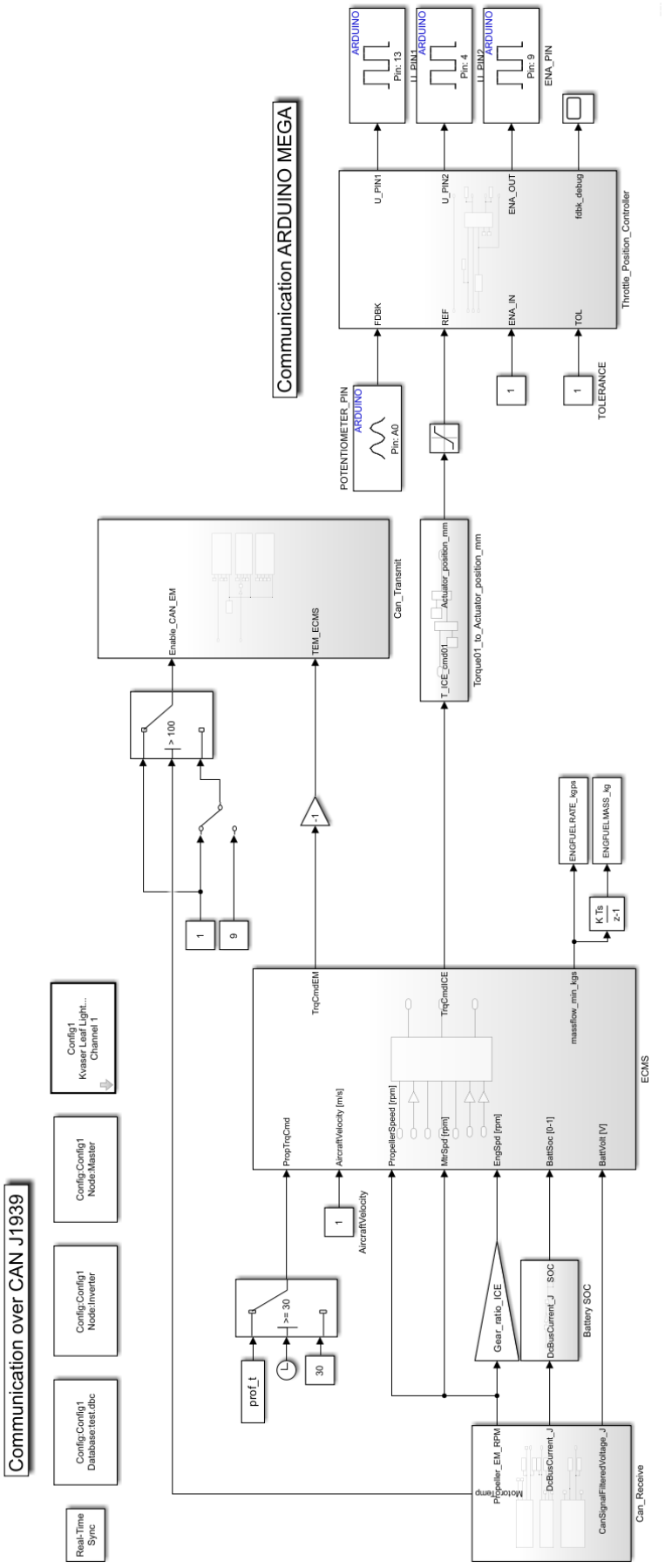

Figure 5.4. Real-Time control strategy A-ECMS in Matlab/Simulink.

5.2. Experimental Real-Time Test of the A-ECMS

The mission profile has been assigned during the time in terms of the required torque at the propeller "PropTrqCmd" with an overall duration of 300 seconds (5 minutes). The chosen profile has a short duration representative of the typical phases of an aviation mission usually carried out by a pilot during take-off, climb, cruise, and landing maneuvers (which certainly have a longer duration). Therefore, the conducted test focuses on the feasibility of the A-ECMS strategy to control the physical propulsion units in the real-time test facility and be able to split the torque required by the pilot "PropTrqCmd" into two torques, "TrqCmdICE" and "TrqCmdEM," respectively.

Furthermore, it has been chosen not to implement closed-loop (feedback) control for the reference torque assigned to controller A-ECMS but to leave it in an open-loop configuration for several reasons closely related to experimental test activities in the engine test bed:

- *Simplicity* – the open-loop control tends to be simpler to implement if compared to closed-loop control;
- *Inherent stability* – open-loop control ensures reliable actuation when the system is not strongly disturbed. In the examined case, the mission profile is intermittently stationary, and external disturbances are practically negligible (e.g., propeller load variation, misfire, etc.), making this control acceptable in the initial analysis;
- *Predictable responses* – it is possible to predict the system's behavior over time with reasonable precision;
- *Safety* – the system stability and predictable response contribute to increasing the safety in test execution. Undoubtedly, this is preferable in initial experimental tests.

However, it is important to highlight that open-loop control has significant limitations as it cannot adapt to changes in conditions or external disturbances and cannot correct system errors. Figure 5.5 displays the selected torque profile "PropTrqCmd" for test execution, and Table 5.2 provides detailed information on the durations of each mission phase. The mission chosen is less demanding than the simulated one in Chapter 4, not only for less duration but also for less required propeller torque of 300 Nm concerning the 580 Nm in the simulated one.

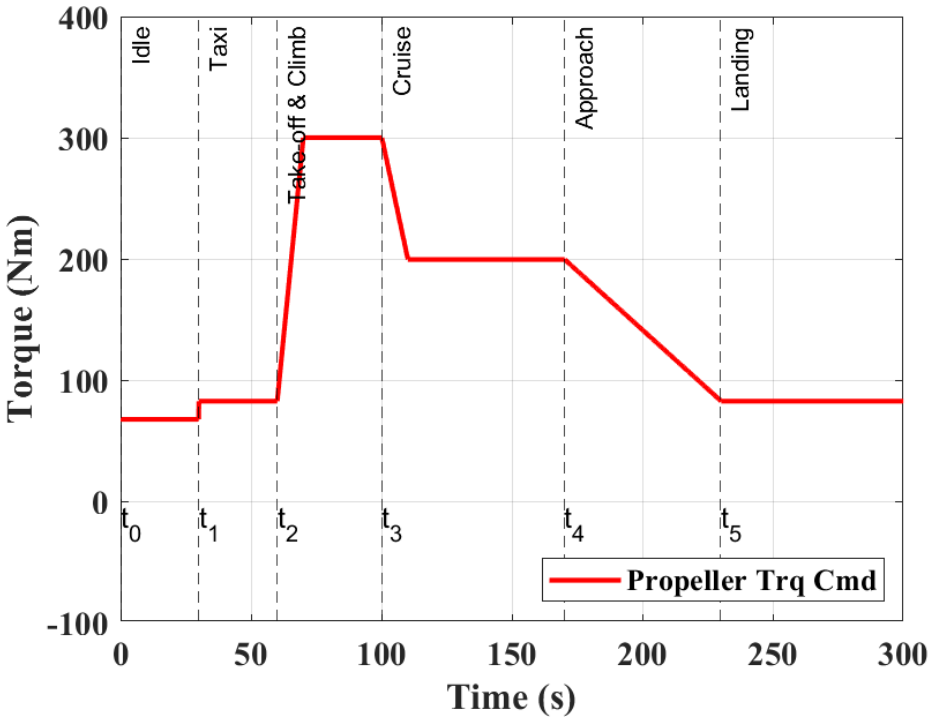

Figure 5.5. Propeller Torque Command (A-ECMS Input).

Table 5.2. Mission phases and duration.

Mission Phase	Start Time (s)	Stop Time (s)	Duration (s)
Idle	$t_0 = 0$	$t_1 = 30$	30
Taxi	$t_1 = 30$	$t_2 = 60$	30
Take-off & Climb	$t_2 = 60$	$t_3 = 100$	40
Cruise	$t_3 = 100$	$t_4 = 170$	70
Approach	$t_4 = 170$	$t_5 = 230$	60
Landing	$t_5 = 230$	$t_6 = 300$	70

The test under consideration has been conducted by setting the MP2030 control of the Schenck brake to the $Mn^2 = k$ mode. Moreover, the A-ECMS setup parameters are shown in Table 5.3. Furthermore, for the following test, it was chosen to simulate a battery with a nominal capacity of $E_{nom} = 1.5\,kWh$ and a maximum charge and discharge power of the battery equal to $C_{rate}^{Charge} = 1.5\,kW$ and $C_{rate}^{Discharge} = 14\,kW$, respectively (precautionary limits respect to the ITECH bi-directional power supply with a peak power of 18 kW). The choice to adopt this battery is primarily related to the nature of the short-duration test conducted, and it was necessary to use a battery with reduced capacity to amplify the effect on the State of Charge, highlighting SoC variations during the mission time.

Table 5.3. Setup of A-ECMS parameters.

Model Parameter	UoM	A-ECMS
SoC_{min}	%	20
SoC_{max}	%	95
SoC_{target}	%	95
SoC_{ini}	%	90
s_0	-	3.385
k_P	-	1
k_I	-	0.1
$p(SoC)$	-	0÷2
a	-	3
TPE_{factor}	-	6
$Constraint\ Penalty$	-	10^7
H_i	MJ/kg	4.35

The desiderate torque to the propeller shaft is called "PropTrqCmd", and it is represented with the red curve in Figure 5.6. The "PropTrqCmd" curve is split into two parts by the A-ECMS control strategy, "TrqCmdICE" (green curve) and "TrqCmdEM" (blue curve), both sent as signals command to the Internal Combustion Engine and Electric Motor respectively, as shown in Figure 5.6. The electric motor torque, denoted as "TrqCmdEM," assumes positive values when the electric machine work as a motor and negative values when it operates as a generator.

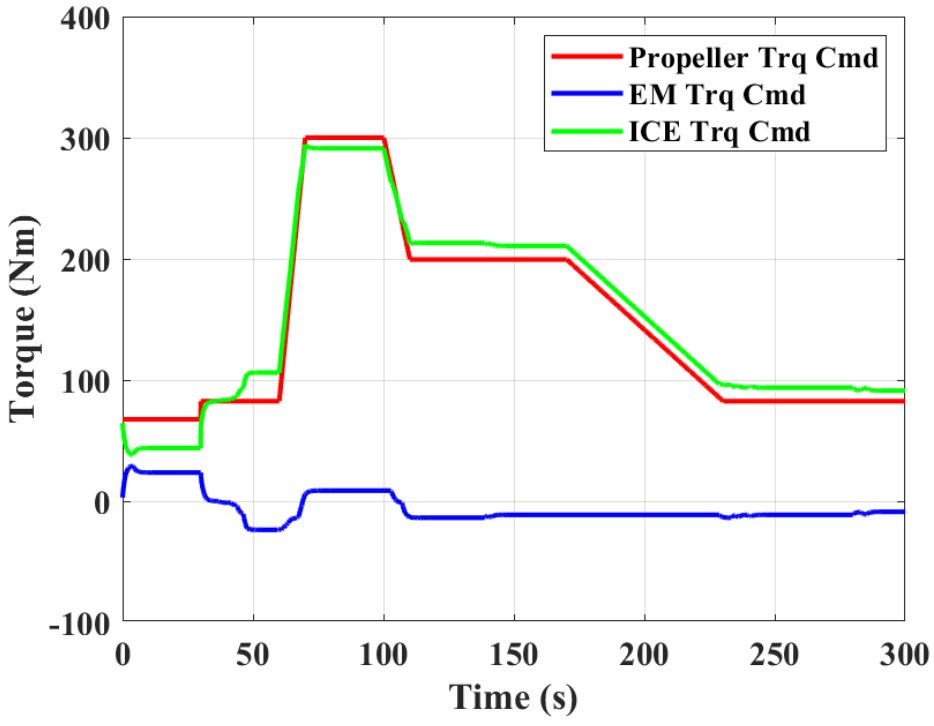

Figure 5.6. Propeller, EM and ICE torque command.

Moreover, Figure 5.7 is plotted (in a dashed black curve) the brake torque measured experimentally through the Eddy Brake. The error between the requested propeller torque (red curve) and the measured one (dashed black curve) is around 4%, increasing at low loads. The difference between these two torque quantities can be attributed to system errors influenced by approximation and interpolation in the map. The torque error between the desired and the measured can be deleted or minimized if a feedback control loop is considered.

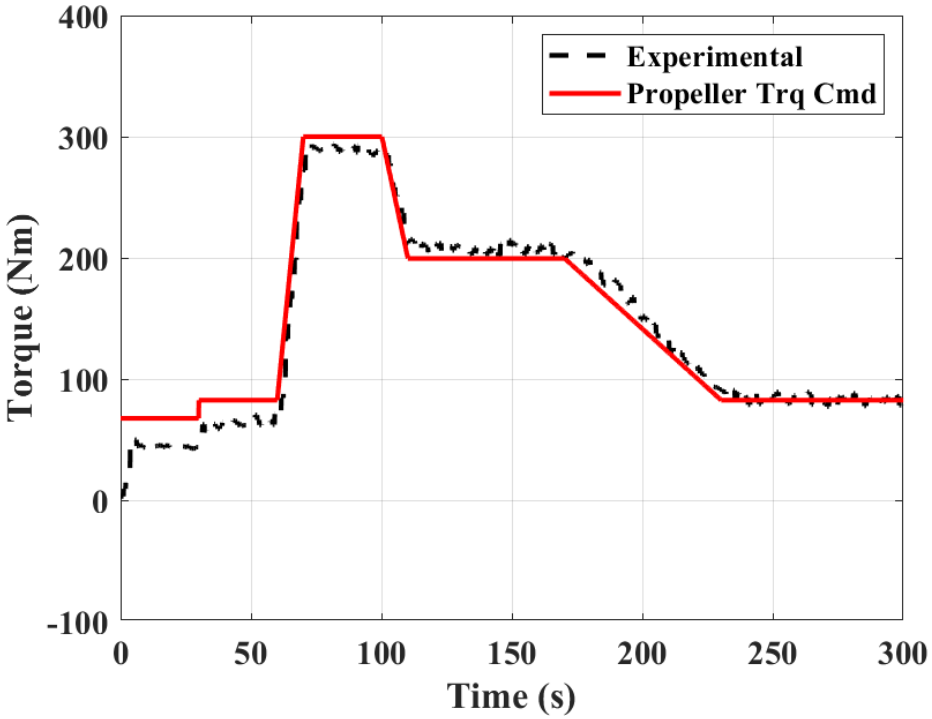

Figure 5.7. Comparison between Propeller Torque Command and Experimental measure.

The rotational speed is measured and plotted in Figure 5.8. In particular, the crankshaft ICE speed assumes double value concerning the EM speed because the CMD22 engine has an internal gear ratio of 2:1. Moreover, the brake speed measured at the eddy-current brake assumes the same value as the EM.

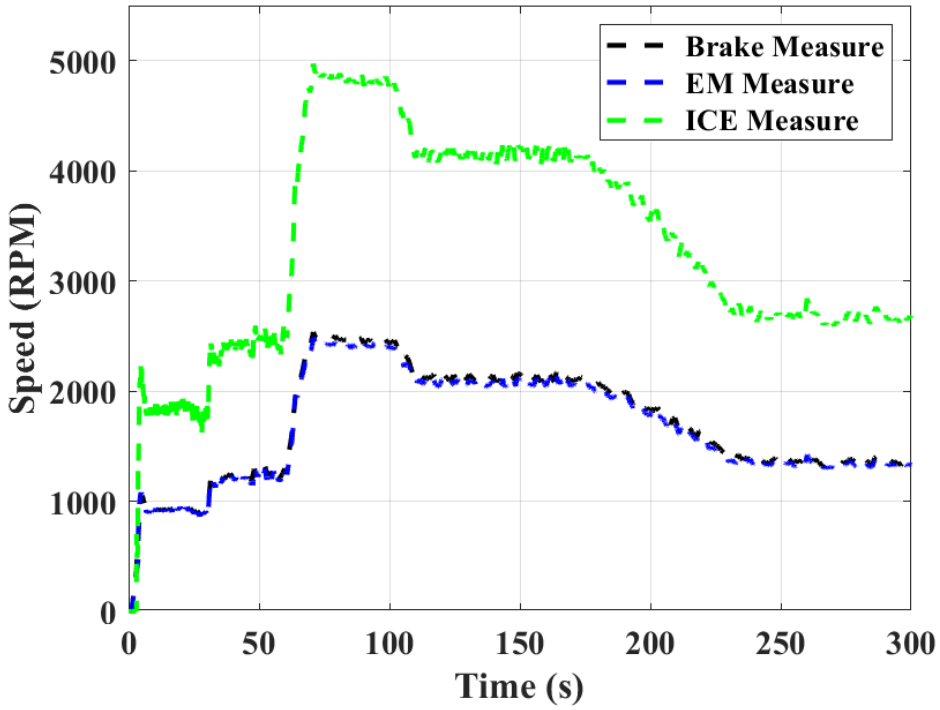

Figure 5.8. Experimental measure of speed: Brake, EM, ICE.

In Figures 5.9 (a-b), torque and power curves are presented in the Speed-Torque and Speed-Power planes, respectively, where you can observe the quadratic relationship of torque with respect to propeller RPM (revolutions per minute), which resembles a real propeller curve.

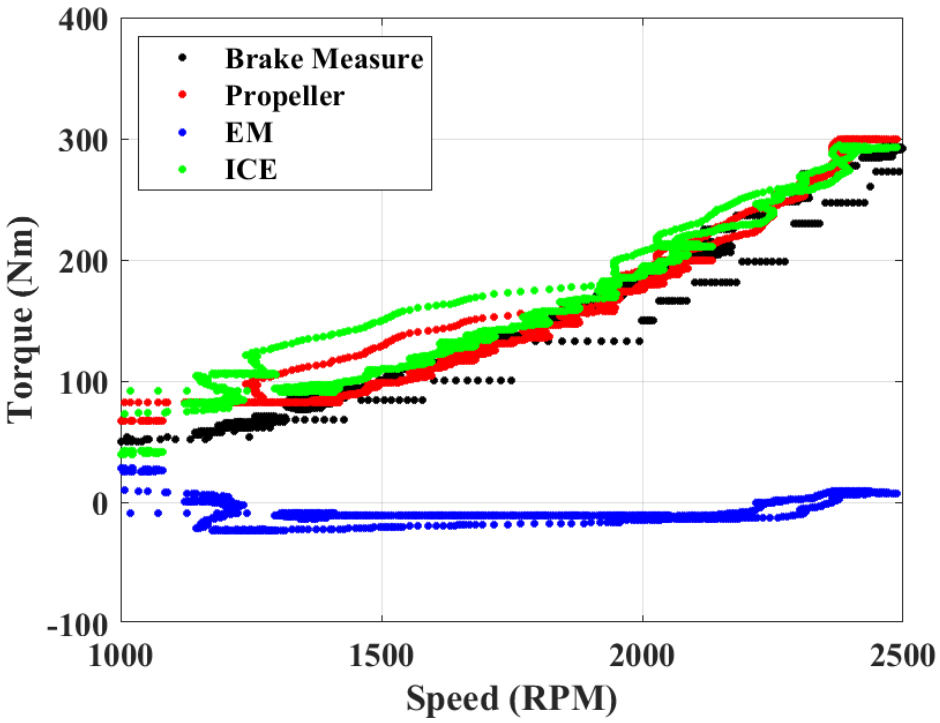

(a)

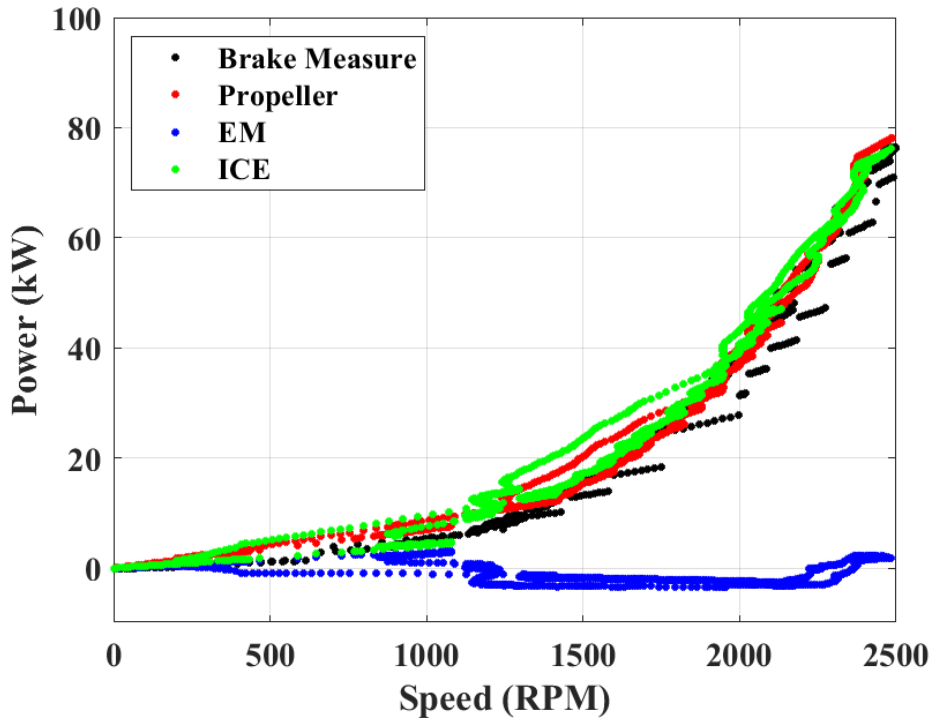

(b)

Figure 5.9. Propeller, EM and ICE: (a) Torque-Speed; (b) Power-Speed.

Figure 5.10 shows the experimental data of Voltage and Current measured on the DC-Link connection between the battery simulator ITECH IT6018C-500-90 and the Inverter GVI-H650. The voltage signal is virtually identical for both measurement systems. However, a different consideration applies to the current values, which vary between DC-Link peaks and valleys. Generally, the electric current variation is often influenced by several factors, such as load dynamics between the source (Motor) and the load (Grid), duty cycles of switching devices in converters that may change to maintain the desired voltage level on the DC-Link, potentially affecting the output current level over time, and passive sink resistors internal to the ITECH power supply, as indicated in Figure 3.13 of Chapter 3. The State of Charge (SoC) is represented by the black curve in Figure 5.10, where the initial level is 90%, while the final value reached 95%, matching the target value.

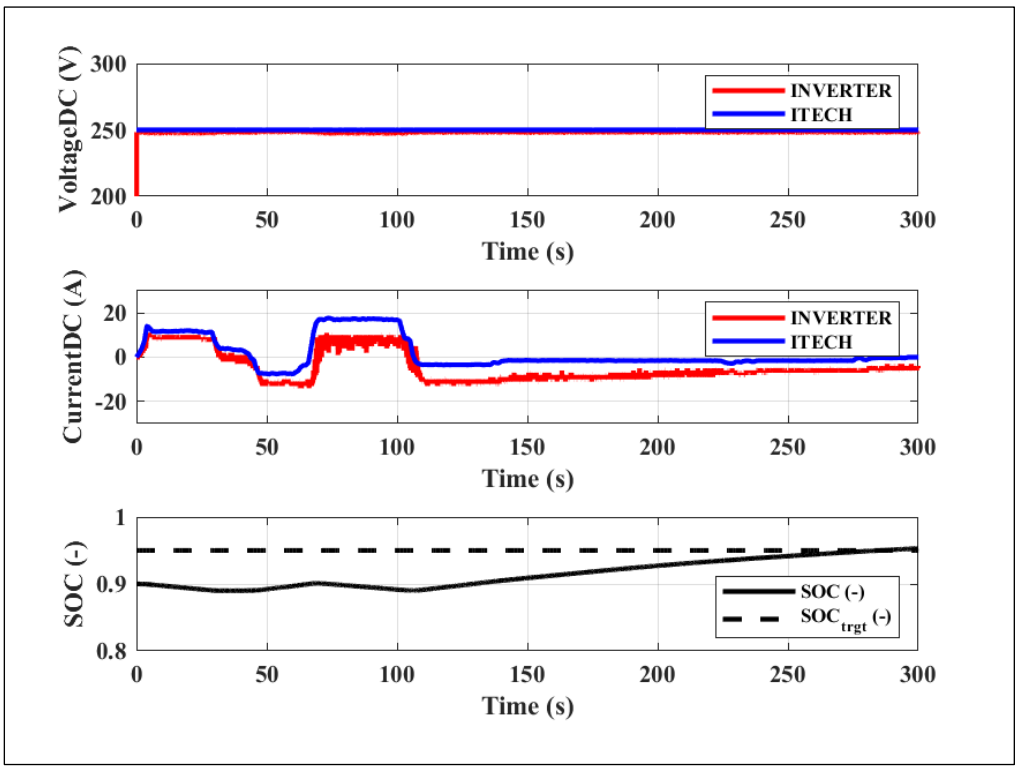

Figure 5.10. Battery Voltage, Current and SOC.

Figure 5.11 shows the graphs related to the adaptive coefficients of the equivalent specific fuel consumption s and the behavior of the Hamiltonian. The initial value of the equivalent specific fuel consumption is $s_0 = 3.385$, and it adapts within the range of $1 < s < 4.6$. The physical meaning of the Hamiltonian is the instantaneous primary power required to carry out the

mission. This value is highest when more power is needed to the HEPS during the take-off and climb phases.

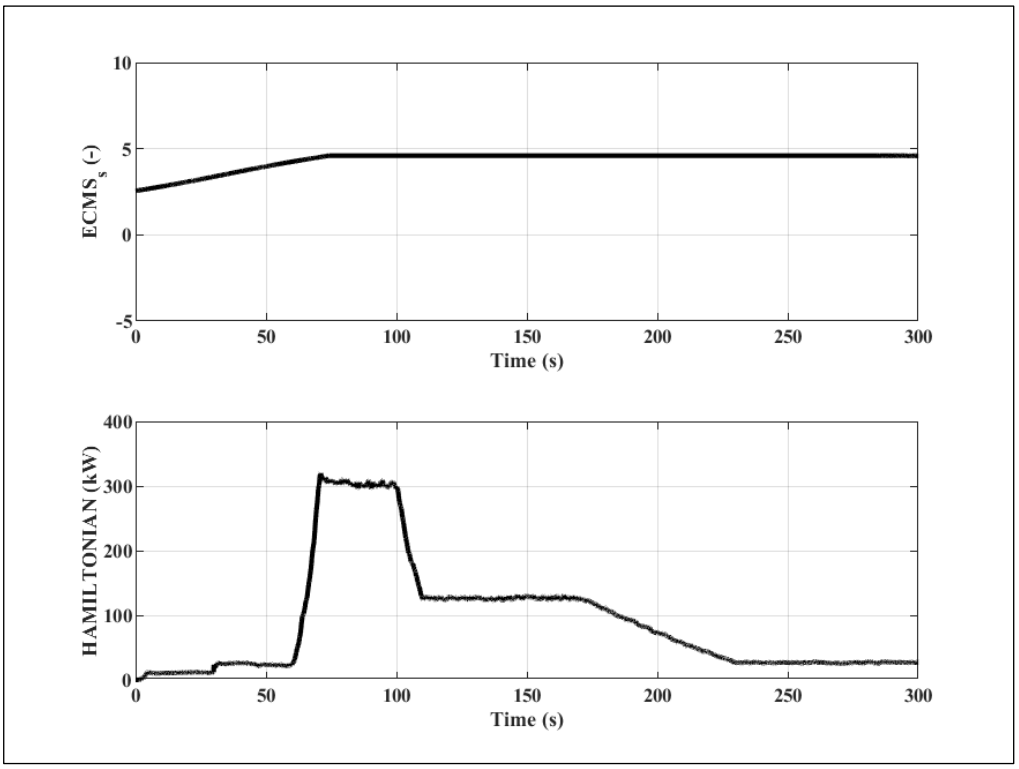

Figure 5.11. Equivalent consumption s and Hamiltonian function.

The objective of the following chapter is closely related to the execution of a Real-Time test for the experimental verification of the A-ECMS control strategy for a hybrid propulsion system. The experimental results obtained in this manner demonstrate the feasibility of implementing the A-ECMS control strategy within a control interval of 0.05 seconds while running an automated and predetermined mission profile.

Chapter 6

6. CONCLUSIONS AND FUTURE DEVELOPMENTS

The Hybrid Electric Propulsion System (HEPS) is a well-established technology to face the global warming and air pollution crisis in the transport sector, especially the automotive field. Other transport sectors, such as aviation, lags behind current hybrid propulsion technology for several reasons, i.e., later emission and efficiency regulations, the heavy certification process for airworthiness, and different mission requirement. These reasons have restricted the HEPS application in the aviation field and, at the same time, have limited technological growth.

In the present Ph.D. thesis, an experimental investigation has been carried out on a hybrid-electric propulsion system for aircraft application. In particular, a hybrid electric propulsion prototype system composed of one internal combustion engine CMD22 and one electric machine EMRAX 268 LV has been designed in parallel configuration adopting a mechanical transmission based on a one-way clutch bearing. The control and data acquisition system has been developed in-house using National Instruments modules and LabView as programming software for the User Guide Interface (GUI).

Preliminary tests have been performed on the hybrid powertrain to verify the operating range of the prototype under examination and evaluate its performance and efficiency under different test conditions. For these purposes, more tests have been carried out, initially on the Electrical Machine and Internal Combustion Engine working alone, subsequently performed considering both engines working together in *hybrid* and *charging* mode. The expected performance in all tests has been confirmed by values obtained through the previous experimental activities. Successively, a short-range mission has been tested experimentally by setting the control of the eddy-current brake, such as a propeller load. In this case, the HEPS demonstrated the feasibility of executing the mission by demonstrating its feasibility to work in *hybrid* and *charging* modes and ensuring battery charging during maneuvers with low torque demand, i.e., runway approach and landing phases.

The experimental data obtained during the mission simulation has been used to validate the HEPS model designed in Matlab/Simulink consisting of a map-based ICE and EM coupled to the dynamical inertia model representing the power transmission, while the EM has been linked to a battery model. The simulated results showed good matching to the experimental ones.

Moreover, the proposed model demonstrates its capability and flexibility to predict the global HEPS dynamical behavior and performance.

The most important object of this dissertation is to provide advanced management control strategies for aeronautical HEPS to minimize the global energy consumption of aircraft according to environmental policies. The presented control strategies, namely the equivalent consumption minimization strategy (ECMS) or adaptive (A-ECMS), lie on the minimization concept of fuel and battery energy consumption, which considers both referring to fuel consumption. This strategy aims to balance the use of the internal combustion engine and the battery efficiently to maximize the overall vehicle efficiency and reduce operating costs.

For these purposes, an A-ECMS control algorithm has been designed and implemented in Matlab/Simulink that makes real-time decisions regarding the power split between the internal combustion engine (ICE) and the electric machine (EM).

The aircraft and propeller dynamical models have been added to the HEPS one for a better and complete analysis of the fuel and energy consumption when a mission profile is considered. For these purposes, two HEPS configurations, having different hybridization factors and both control strategies, ECMS and A-ECMS, are considered.

The energy assessment is compared to the conventional "*Fully-Thermal*" unit consisting of one ICE Continental IO-360.

The main results presented in Table 4.7 demonstrate a consistent enhancement in efficiency across all configurations of Hybrid-Electric Propulsion Systems (HEPS). In fact, it can be observed that compared to the "*Fully-Thermal*" Continental IO-360, the improvements range between 6% to 31.3%, leading to a significant reduction in total primary energy consumption E_p^{tot} and a subsequent decrease in CO_2 emissions $M_{CO_2}^{tot}$ for the considered mission compared to the "*Fully-Thermal*" configuration.

Specifically, the configurations with a higher Degree of Hybridization ($DoH_P = 0.4$) exhibit similar results for both optimization strategies, ECMS and A-ECMS. In these cases, the internal combustion engine, particularly the CMD22 engine, functions as a range extender, extending the hybrid system's range and operation time before battery depletion. However, the CMD22's limited torque contribution prevents effective battery recharge, requiring a "*Plug-In*" charging system post-landing.

Conversely, configurations with a lower Degree of Hybridization ($DoH_P = 0.28$), utilizing the Continental IO-360 engine, allow for successful battery recharge at the end of the mission, especially when employing the A-ECMS control strategy. This adaptive strategy increases the weight of chemical energy stored in the battery, making the Continental engine's higher torque

availability advantageous. This configuration can operate as a "*Full-Hybrid*" when battery recharge is unnecessary after landing.

Comparing control strategies, A-ECMS proves more effective in restoring the initial battery state of charge than ECMS, emphasizing the importance of adaptive management for efficient hybrid-electric propulsion.

Overall, the hybrid-electric configurations, whether "*Plug-In*", "*Full-Hybrid*" or with an adaptive control strategy, offer advantages in terms of reduced fuel consumption and CO_2 emissions compared to conventional setups. These benefits stem from the mechanical coupling of the electric machine, enhancing the thermal engine's efficiency and enabling it to operate in more efficient zones.

While "*Plug-In*" and "*Full-Hybrid*" configurations present efficiency and environmental advantages, they face challenges related to the substantial size and weight of the battery pack, limiting operational range. On the other hand, "*Full-Hybrid*" configurations address the range limitation issue, achieving a modest improvement in overall efficiency (around 6%). Despite the challenges, these findings underscore the potential of hybrid-electric propulsion systems, especially in the context of the general aviation field where cruise phases dominate mission profiles. Future advancements in the National Electric Grid and the renewable energy share may further enhance the appeal of electric configurations.

The Aeronautical improvement efficiency trend is not high because flight missions often involve long periods of steady-state flight with few load variations. This configuration makes life difficult for hybrid-electric propulsion systems, which generally gain efficiency points by assisting the internal combustion engine during recurring transient phases. Moreover, the lower efficiency of the internal combustion engine during fastly transient conditions is typically averaged by EM (e.g., in the automotive field).

Lastly, is carried out an experimental activity on the hybrid-electric propulsion system to test the real-time control A-ECMS strategies. For this purpose, a short-duration mission has been chosen to represent the typical aviation maneuvers generally performed by a pilot (i.e., Take-off, climb, cruise, and landing). The results show the capability of the A-ECMS to control in real-time the hybrid electric system splitting quickly the engine command and at the same time following the pilot imposed required torque.

In addition, the A-ECMS strategy has been shown experimentally the capability to recharge the battery during the assigned mission and restore the final value to the Target value.

Future developments will deal with the following purposes:

- further experimental validations will be performed on the HEPS adopting a real propeller and battery pack. For this purpose, the engine test bed laboratory will need an upgrade with other measuring and security systems;
- possibility of developing embedded solutions for integrating the strategy A-ECMS in hardware units for making real-time torque control of a HEPS. Moreover, will be implemented the closed-loop (feedback) control for the reference torque assigned to controller A-ECMS;
- the possibility of applying the strategy A-ECMS for monitoring purposes to other HEPS (i.e., naval applications).

7. References

[1] IPCC. A. (2013). Climate change 2013: the physical science basis. Contribution of working group I to the fifth assessment report of the intergovernmental panel on climate change. 1535.

[2] Lacis. A. A.. Schmidt. G. A.. Rind. D.. & Ruedy. R. A. (2010). Atmospheric CO_2: Principal control knob governing Earth's temperature. Science. 330(6002). 356-359.

[3] Friedlingstein. P.. O'sullivan. M.. Jones. M. W.. Andrew. R. M.. Gregor. L.. Hauck. J.. & Zheng. B. (2022). Global carbon budget 2022. Earth System Science Data Discussions. 2022. 1-159.

[4] 5th Assessment Report (AR5). the Intergovernmental Panel on Climate Change (IPCC). The World Resources Institute. September 2020.

[5] Un climate change conference COP21 CMP11 – Paris 2015 https://www.mase.gov.it/pagina/cop-21-laccordo-di-parigi

[6] ICAO Environmental Report 2022 - Innovation for a green transition.

[7] National Aeronautics Research and Development Plan -National science and technology council (2010) -Washington. D.C. 20502. February 2.

[8] European Comission. Flightpath 2050 - Europe's vision for aviation. Report of the high level group. Policy. EU directorate-general for research and innovation. Directorate General for Mobility and Transport on Aviation Research. Luxembourg (2011).

[9] Adu-Gyamfi. B. A.. & Good. C. (2022). Electric aviation: A review of concepts and enabling technologies. Transportation Engineering. 100134.

[10] ARTS. A Journey Through the History of Electric Aircraft—It is Almost Half a Century Since the First Manned. Electrically Propelled Flight. Accessed: Nov. 13. 2019. Available: https://www.arts.eu/journey-through-the-historyof-electric-aircraft

[11] Liu. W. (2017). Hybrid electric vehicle system modeling and control. John Wiley & Sons.

[12] Mi. C.. & Masrur. M. A. (2017). Hybrid electric vehicles: principles and applications with practical perspectives. John Wiley & Sons.

[13] Hannan. M. A.. Azidin. F. A.. & Mohamed. A. (2014). Hybrid electric vehicles and their challenges: A review. Renewable and Sustainable Energy Reviews. 29. 135-150.

[14] Singh. K. V.. Bansal. H. O.. & Singh. D. (2019). A comprehensive review on hybrid electric vehicles: architectures and components. Journal of Modern Transportation. 27. 77-107.

[15] MacCready. P. (1999). Regenerative battery-augmented soaring. Technical Soaring. 23(1). 28-32.

[16] Bowman. C. L.. Felder. J. L.. & Marien. T. V. (2018. July). Turbo-and hybrid-electrified aircraft propulsion concepts for commercial transport. In 2018 AIAA/IEEE Electric Aircraft Technologies Symposium (EATS) (pp. 1-8). IEEE.

[17] Lorenz. L.. Seitz. A.. Kuhn. H.. & Sizmann. A. (2014). Hybrid power trains for future mobility. Bonn. Germany: Deutsche Gesellschaft für Luft-und Raumfahrt-Lilienthal-Oberth eV.

[18] Vidyanandan. K. V. (2018). Overview of electric and hybrid vehicles. Energy Scan. 3. 7-14.

[19] Ragone. D. V. (1968). Review of battery systems for electrically powered vehicles (No. 680453). SAE Technical Paper.

[20] Tariq. M.. Maswood. A. I.. Gajanayake. C. J.. & Gupta. A. K. (2017). Aircraft batteries: current trend towards more electric aircraft. IET Electrical Systems in Transportation. 7(2). 93-103.

[21] Uber-Elevate. "Fast-forwarding to a future of on-demand urban air transportation." Uber 2016. Accessed: 16th April 2021. Available: https ://evtol.news/__media/PDFs/UberElevateWhitePaperOct2016.pdf.

[22] Armand. M.. & Tarascon. J. M. (2008). Building better batteries. Nature. 451(7179). 652-657.

[23] Cerdas. F.. Titscher. P.. Bognar. N.. Schmuch. R.. Winter. M.. Kwade. A.. & Herrmann. C. (2018). Exploring the effect of increased energy density on the environmental impacts of traction batteries: A comparison of energy optimized lithium-ion and lithium-sulfur batteries for mobility applications. Energies. 11(1). 150.

[24] Shahjalal. M.. Shams. T.. Islam. M. E.. Alam. W.. Modak. M.. Hossain. S. B.. ... & Iqbal. A. (2021). A review of thermal management for Li-ion batteries: Prospects. challenges. and issues. Journal of energy storage. 39. 102518.

[25] Airbus. (2021). Electric Flight—Laying the Groundwork for Zero-Emission Aviation.

[26] Bradley. M. (2022. June). Identification and descriptions of fuel cell architectures for aircraft applications. In 2022 IEEE Transportation Electrification Conference & Expo (ITEC) (pp. 1047-1050). IEEE.

[27] Santin. M.. Traverso. A.. & Massardo. A. (2008). Technological aspects of gas turbine and fuel cell hybrid systems for aircraft: a review. The Aeronautical Journal. 112(1134). 459-467.

[28] Larminie. J.. Dicks. A.. & McDonald. M. S. (2003). Fuel cell systems explained (Vol. 2. pp. 207-225). Chichester. UK: J. Wiley.

[29] Massaro. M. C.. Biga. R.. Kolisnichenko. A.. Marocco. P.. Monteverde. A. H. A.. & Santarelli. M. (2023). Potential and technical challenges of on-board hydrogen storage technologies coupled with fuel cell systems for aircraft electrification. Journal of Power Sources. 555. 232397.

[30] Agamloh. E.. Von Jouanne. A.. & Yokochi. A. (2020). An overview of electric machine trends in modern electric vehicles. Machines. 8(2). 20.

[31] Vukosavic. S. N. (2012). Electrical machines. Springer Science & Business Media.

[32] Melkebeek. A. J. (2018). Electrical machines and drives: fundamentals and advanced modelling. Springer International Publishing.

[33] Dorn-Gomba. L.. Ramoul. J.. Reimers. J.. & Emadi. A. (2020). Power electronic converters in electric aircraft: Current status. challenges. and emerging technologies. IEEE Transactions on Transportation Electrification. 6(4). 1648-1664.

[34] De Doncker. R. W.. Pulle. D. W.. & Veltman. A. (2020). Advanced electrical drives: analysis. modeling. control. Springer Nature.

[35] CMD s.p.a. a Loncin Company Via Pacinotti 2. San Nicola la Strada CE. Italy. https://www.cmdengine.com/divisioni/avio/

[36] EMRAX d.o.o. Molkova pot 5 SI-1241 Kamnik Slovenia. EU https://www.cmdengine.com/divisioni/avio/

[37] PARKER Hannifin Italy s.r.l. https://ph.parker.com/it/it/product-list/gvi-global-vehicle-inverter-for-mobile-applications

[38] TAMAGAWA SEIKI Co.. Ltd. Japan. https://www.tamagawa-seiki.com/

[39] Liu. H.. & Wu. Z. (2018). Demodulation of angular position and velocity from resolver signals via Chebyshev filter-based type III phase locked loop. Electronics. 7(12). 354.

[40] Guo. M.. & Wu. Z. (2019). Noise reduction for high-accuracy automatic calibration of resolver signals via DWT-SVD based filter. Electronics. 8(5). 516.

[41] ITECH Electronic Co.. Ltd. China. https://www.itechate.com/en/download.html

[42] C.T.S. via Peregallo 16. 20836. Briosco (MB) Italy. https://www.ctsitaly.it/

[43] LabVIEW. F. P. G. A. (2009). National Instruments. Austin. Texas. 78730-5039.

[44] Cardone, M., Gargiulo, B., & Fornaro, E. (2021, July). Development of a flexible test bench for a Hybrid Electric Propulsion System. In 2021 IEEE International Workshop on Metrology for Automotive (MetroAutomotive) (pp. 221-225). IEEE.

[45] Zulkifli. S. A.. Asirvadam. V. S.. Saad. N.. Aziz. A. R. A.. & Mohideen. A. A. M. (2014. June). Implementation of electronic throttle-by-wire for a hybrid electric vehicle using National Instruments' CompactRIO and LabVIEW Real-Time. In 2014 5th International Conference on Intelligent and Advanced Systems (ICIAS) (pp. 1-6). IEEE.

[46] Padmanaban. V. (2016). Investigation of Combustion Phenomena in a Single-Cylinder Spark-Ignited Natural Gas Engine with Optical Access. West Virginia University.

[47] Parreiras. T. M.. Brandao. D. A. D. L.. Ramos. M. D. F.. Maia. T. A.. Corrêa. T. P.. Pires. I. A.. ... & de JC Filho. B. (2023. June). Permanent Magnet Synchronous Motor Drive Control for Hybrid Construction Machinery-Revisited. In 2023 IEEE Transportation Electrification Conference & Expo (ITEC) (pp. 1-6). IEEE.

[48] Pira. C.. Chyhyrynets. E.. Stivanello. F.. & Caforio. R. (2021. March). Plasma Electrolytic Polishing as a promising treatment replacement of electropolishing in the copper and Niobium substrate preparation for SRF. In Proceedings of the 9th International Workshop on Thin Films and New Ideas for Pushing the Limits of RF Superconductivity. Online (pp. 15-18).

[49] Yang. G.. Zhang. S.. & Zhang. C. (2020). Analysis of Core Loss of Permanent Magnet Synchronous Machine for Vehicle Applications under Different Operating Conditions. Applied Sciences. 10(20). 7232.

[50] P. M. Sforza. ``Propellers." in Theory of Aerospace Propulsion. P. M. Sforza. Ed. Oxford. U.K.: Butterworth-Heinemann. 2017. pp. 487_524. doi: 10.1016/B978-0-12- 809326-9.00010-5.

[51] B. W. McCormick. Aerodynamics. Aeronautics. and Flight Mechanics. Hoboken. NJ. USA: Wiley. 1994. [Online]. Available: https://books.google.it/books?id=ALRkQgAACAAJ

[52] Energy, S. (2012). Panasonic NCR18650B.

[53] Fornaro. E.. Cardone. M.. & Dannier. A. (2022). A Comparative Assessment of Hybrid Parallel. Series. and Full-Electric Propulsion Systems for Aircraft Application. IEEE Access. 10. 28808-28820.

[54] (May 2020). ExxonMobil Aviation Gasolines. https://www.exxonmobil.com/en-us/commercial-fuel/pds/gl-xx-avgasseries

[55] ISPRA. (2020). Fattori di Emissione Atmosferica di Gas a Effetto Serra Nel Settore Elettrico Nazionale e Nei Principali Paesi Europei. https://www.isprambiente.gov.it

[56] Cardone. M.. Gargiulo. B.. & Fornaro. E. (2021). Modelling and experimental validation of a hybrid electric propulsion system for light aircraft and unmanned aerial vehicles. Energies. 14(13). 3969.

[57] Mathworks: MATLAB. Mapped SI Engine. Natick. Massachusetts: The MathWorks Inc. (2023). https://it.mathworks.com/help/autoblks/ref/mappedsiengine.html

[58] Mathworks: MATLAB. Mapped Motor. Natick. Massachusetts: The MathWorks Inc. (2023). https://it.mathworks.com/help/autoblks/ref/mappedmotor.html

[59] Mathworks: MATLAB. Generic Battery Model. Natick. Massachusetts: The MathWorks Inc. (2023). https://it.mathworks.com/help/sps/powersys/ref/battery.html

[60] Iodice. P.. Fornaro. E.. & Cardone. M. (2022). Hybrid Propulsion in SI Engines for New Generation Motorcycles: A Numerical-Experimental Approach to Assess Power Requirements and Emission Performance. Energies. 15(17). 6312.

[61] Onori. S.. Serrao. L.. & Rizzoni. G. (2016). Hybrid electric vehicles: Energy management strategies.

[62] Paganelli. G.. Guerra. T. M.. Delprat. S.. Santin. J. J.. Delhom. M.. & Combes. E. (2000). Simulation and assessment of power control strategies for a parallel hybrid car. Proceedings of the Institution of Mechanical Engineers. Part D: Journal of Automobile Engineering. 214(7). 705-717.

[63] Paganelli. G. (2000). A general formulation for the instantaneous control of the power split in charge-sustaining hybrid electric vehicles. In Proc. AVEC 2000. 5th Int. Symp. on Advanced Vehicle Control.

[64] Serrao. L.. Onori. S.. & Rizzoni. G. (2009. June). ECMS as a realization of Pontryagin's minimum principle for HEV control. In 2009 American control conference (pp. 3964-3969). IEEE.

[65] Fornaro. E.. Cardone. M.. & Dannier. A. (2022. June). Hybrid Electric Aircraft Model Based on ECMS Control. In 2022 International Symposium on Power Electronics. Electrical Drives. Automation and Motion (SPEEDAM) (pp. 865-870). IEEE.

[66] Dannier. A.. Ferraro. L.. Miceli. R.. Piegari. L. U. I. G. I.. & Rizzo. R. (2013. March). Numerical and experimental validation of a LiFePO 4 battery model at steady state and transient operations. In 2013 Eighth International Conference and Exhibition on Ecological Vehicles and Renewable Energies (EVER) (pp. 1-6). IEEE.

[67] Rezaei. A.. Burl. J. B.. & Zhou. B. (2017). Estimation of the ECMS equivalent factor bounds for hybrid electric vehicles. IEEE Transactions on Control Systems Technology. 26(6). 2198-2205.

[68] Kessels. J. T.. Koot. M. W.. Van Den Bosch. P. P.. & Kok. D. B. (2008). Online energy management for hybrid electric vehicles. IEEE Transactions on vehicular technology. 57(6). 3428-3440.

[69] Chasse. A.. Sciarretta. A.. & Chauvin. J. (2010). Online optimal control of a parallel hybrid with costate adaptation rule. IFAC proceedings volumes. 43(7). 99-104.

[70] Onori. S.. Serrao. L.. & Rizzoni. G. (2010. January). Adaptive equivalent consumption minimization strategy for hybrid electric vehicles. In Dynamic systems and control conference (Vol. 44175. pp. 499-505).

[71] McCormick, B. W. (1994). Aerodynamics, aeronautics, and flight mechanics. John Wiley & Sons.

[72] Kimberlin, R. (1998, April). Certification flight test for an extended range modification for the Cessna 337 aircraft. In 2000 World Aviation Conference (p. 5501).

[73] Saxena, E. S., & Kumar, M. R. (2015). Design of NACA 2412 and its Analysis at Different Angle of Attacks, Reynolds Numbers, and a wind tunnel test. International Journal of Engineering Research and General Science, 3(2), 193-200.

[74] Sforza, P. M. (2016). Theory of aerospace propulsion. Butterworth-Heinemann.

[75] Kimberlin, R. (2002). Certification Flight Tests of 3-bladed MT Propellers on the Cessna 337 Aircraft. In AIAA's Aircraft Technology, Integration, and Operations (ATIO) 2002 Technical Forum (p. 5808).

[76] Doff-Sotta, M., Cannon, M., & Bacic, M. (2020). Optimal energy management for hybrid electric aircraft. IFAC-PapersOnLine, 53(2), 6043-6049.

[77] Fornaro, E., & Tordela, C. (2023). An Energy Management Strategy for Aeronautical Hybrid Propulsion Systems Based on an MPC Supervisor (No. 2023-24-0026). SAE Technical Paper.

[78] Friedrich, C., & Robertson, P. A. (2015). Hybrid-electric propulsion for automotive and aviation applications. CEAS Aeronautical Journal, 6, 279-290.

[79] Peerzada, P., Larik, W. H., & Mahar, A. A. (2021). DC motor speed control through arduino and L298N motor driver using PID controller. International Journal of Electrical Engineering & Emerging Technology, 4(2), 21-24.

[80] Mathworks: MATLAB. Communicate with Hardware Using Connected IO: Arduino Boards. (2023) https://it.mathworks.com/help/supportpkg/arduino/ug/connected-io.html#mw_3c4745a2-f09e-4c87-83ca-6577d9b1288c_sep_mw_94c0ac9a-2e51-411e-b6ab-8a57df012050

[81] Mathworks: MATLAB. Get Started with J1939 Communication in Simulink. (2023) https://it.mathworks.com/help/vnt/ug/basic-j1939-communication-over-can.html

Appendix A

Design and structural check

1.Verifica albero EMRAX 268 ESO

I componenti meccanici progettati sono rappresentati con i numeri 1 e 2 in Figura A.1 e sono rispettivamente :

1. l'albero di accoppiamento tra Propeller shaft (CMD22) e l'innesto interno al cuscinetto unidirezionale (one-way bearing);
2. flangia di accoppiamento tra cuscinetto unidirezionale (one-way bearing) e flangia FSI EMRAX 268.

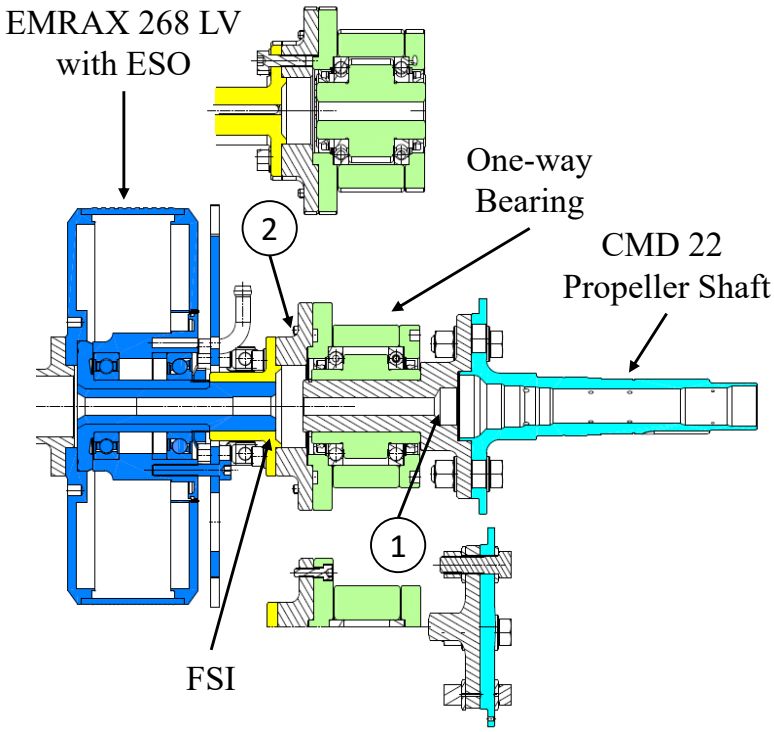

Figura A.1. Sezione 2D dell'accoppiamento meccanico tra CMD22 ed EMRAX 268.

La coppia del motore CMD22 viene trasferita all'elica attraverso una linea d'asse progettata per l'applicazione ibrida elettrica aeronautica. Essa è costituita dai seguenti componenti meccanici (da *dx* verso *sx*): Propeller shaft CMD22, l'albero (1), il cuscinetto unidirezionale (one-way bearing), la flangia (2), la flangia FSI e l'albero EMRAX with ESO.

Tutti i componenti meccanici che costituiscono la linea d'asse sono sollecitati dalla coppia del motore termico CMD22, mentre l'albero EMRAX with ESO è sollecitato, oltre che dalla coppia del motore termico, anche dalla coppia del motore elettrico. A valle di questa considerazione, è stata condotta una verifica a fatica sull'albero EMRAX 268 LV denominato Extended Shaft with Outer Splines (ESO).

Definizione del carico:

Possiamo assumere che il momento torcente totale sia somma di due componenti una legata al motore termico CMD22 e l'altra al motore elettrico EMRAX 268 come indicato in Tabella A.1 e mostrato in Figure A.2.

Table A.1.Definizione dei carichi.

Signals	Torque (Nm)	Speed (rpm)	Power (kW)
ICE	330	2750	95
EM	215	2750	62
TOT.	545	2750	157

Si trascura in questa analisi il carico di trazione dell'elica, e la forza peso dell'elica.

La verifica strutturale viene condotta in due punti specifici dell'albero EMRAX ESO, rispettivamente punto A in corrispondenza di una sede per chiavette e B riguardo alla variazione di portata (come mostrato in Figura A.2). Inoltre, in questi punti si esplicano due coppie differenti: in A solo la coppia del motore ICE, in B la somma della coppia ICE più EMRAX.

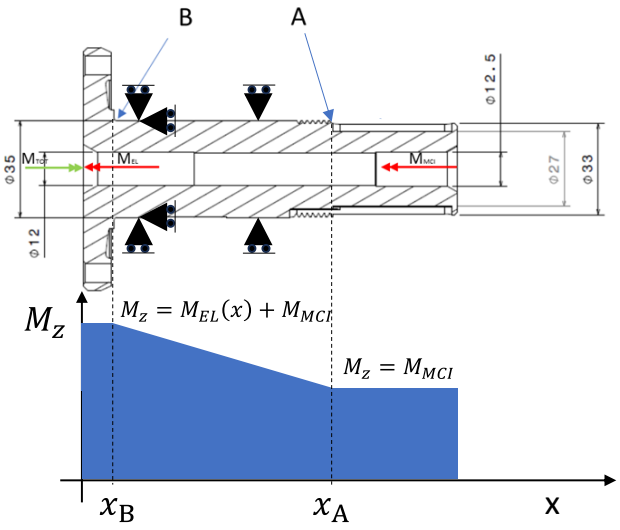

Figure A.2.Carichi e vincoli applicati all'albero EMRAX 268 (ESO).

Definizione del materiale:

Nella Tabella A.2 sono riportate le proprietà meccaniche del materiale di cui è composto l'albero EMRAX ESO (acciaio legato 42CrMo4QT).

Table A.2. Proprietà Meccaniche 42CrMo4QT (EN 10083-3 : 2006).

Diameter Ø (mm)	Tensile Strength Rm (N/mm2)	Yeld Point Rp02 (N/mm2)	Elongation A5 (%)	Hardness Brinell HB
<Ø≤16	1100-1200	Min. 750	Min.8	298-359
16<Ø≤40	1000-1200	Min. 750	Min.11	298-359
40<Ø≤100	900-1100	Min. 700	Min.12	271-331
100<Ø≤160	800-950	Min. 550	Min.13	240-286
160<Ø≤250	750-900	Min. 500	Min.14	225-271
250<Ø≤500	Min. 600	Min. 390	Min.16	178 min

Definizione della geometria:

Si definiscono le geometrie dell'albero EMRAX ESO nei punti A e B oggetto di analisi:

A) Diametro della cava interna è pari a $\mathrm{d} = 12.5$ mm diametro esterno $\mathrm{D_e} = 33$ mm a vantaggio di sicurezza si considera $\mathrm{D_e} = 27$ mm (diametro esterno riferito alla base interna della cava della linguetta). Dalle tabelle dei coeff. di intaglio si ottiene con raccordo $\mathrm{r} = 1$ mm ed $r/d = 0.03$ mm e $D_e/\mathrm{d} = 1.22$ pari a $K_{ts} = 1.8$.

B) Diametro della cava interna è pari $\mathrm{d} = 12$ mm, diametro esterno $\mathrm{D_e} = 35$ mm e l'interasse dei fori è pari a $\mathrm{D_{fori}} = 75$ mm. Dalle tabelle dei coeff. di intaglio con raccordo $\mathrm{r} = 1$ mm ed $r/D_e = 0.028$ mm e $\mathrm{D_{fori}/D_e} = 2.1$ pari a $K_{ts} = 2.2$

Verifica Statica:

La sollecitazione di torsione in una corona circolare risulta: $\tau_{max} = \frac{M_t}{W_t} = \frac{M_t}{\frac{D^4 - d^4}{32 \cdot D} \cdot \pi}$

Assumiamo un coeff. di incertezza del carico $\mathrm{i} = 1.2$.

A)

$$\tau = \frac{{M_t}^{\mathrm{ICE}} \cdot i}{W_t} = \frac{330 \cdot 1.2}{1843.6} \cdot 10^3 = 214.8\ (MPa)$$

Considerando il coefficiente di intaglio $K_{ts} = 1.8$ per la cava linguetta, abbiamo:

$$\tau_{max} = \tau \cdot K_{ts} = 386.6\ (MPa)$$

Confrontando con la τ_{amm} del materiale riteniamo superata la verifica nel punto A.

$$\tau_{amm} = \frac{\sigma_y}{\sqrt{3}} = 433\ (MPa)$$

$$\tau_{max} \leq \tau_{amm}$$

Valutiamo un Margine di Sicurezza pari a M.S =1.12.

B)

$$\tau = \frac{{M_t}^{\mathrm{TOT}} \cdot i}{W_t} = \frac{545 \cdot 1.2}{4151.1} \cdot 10^3 = 157.5\ (MPa)$$

Considerando il coefficiente di intaglio $K_{ts} = 2.2$ per la variazione di portata dell'albero. Abbiamo

$$\tau_{max} = \tau \cdot K_{ts} = 346.5\ (MPa)$$

Confrontando con la τ_{amm} del materiale riteniamo superata la verifica nel punto B.

$$\tau_{amm} = \frac{\sigma_y}{\sqrt{3}} = 433\ (MPa)$$

$$\tau_{max} \leq \tau_{amm}$$

Valutiamo un Margine di Sicurezza pari a M.S =1.25.

Verifica a Fatica nel punto A maggiormente sollecitato:

Conduciamo l'analisi a fatica solo per il punto A (maggiormente sollecitato).

Consideriamo a tal proposito un ciclo a fatica pulsante dallo zero avente valore medio della tensione pari a $S_m = 180\ (MPa)$ ottenuto dal valore medio di coppia motore pari a ${M_t}^{\mathrm{ICE}} = 330\ Nm$ nel punto A.

La scelta di considerare un ciclo a fatica pulsante dallo zero e non pulsante generico (come solitamente si considera in campo motoristico) è legato alla presenza del cuscinetto unidirezionale che assolve le funzioni di vincolo torsionale solo in un verso di rotazione (quella del moto). Nel verso opposto infatti risulta libero e quindi il carico risulta nullo. Pertanto le variazioni torsionali possono essere considerate dirette solo in un verso di rotazione, ovvero quella del moto.

$$\tau = \frac{M_t}{W_t} = \frac{330}{1843.6} \cdot 10^3 = 180\ (MPa)$$

Pertanto, le sollecitazioni a fatica assumono i valori: componente alterna $S_a = 180\ (MPa)$, $S_{max} = 330\ (MPa)$, $S_{min} = 0\ (MPa)$, come mostrato in Figura A.3 (a).

Dall'equazione di Marin è stato corretto il limite di fatica:

$$S_e = k_a \cdot k_b \cdot k_c \cdot k_d \cdot k_e \cdot k_{fs} \cdot {S'}_e$$

k_a fattore di modifica per la condizione superficiale dove $k_a = aS_{ut}^b$ (lavorazioni alle macchine utensili $a = 4.51$, b $= -0.265$;

k_b fattore di modifica per la dimensione dove $k_b = 1.24d^{-0.107}$;

k_c fattore di modifica per il tipo di carico dove $k_c = 0.59$;

k_d fattore di modifica per la temperatura con T=50°C;

k_e coefficiente di sicurezza dove l'affidabilità richiesta è pari al 99% $k_e = 0.814$;

k_{fs} fattore di modifica per effetto di intaglio $k_{fs} = 1 + q_t(k_{ts} - 1) = 1.78$;

S'_e limite di fatica a flessione rotante.

Dal grafico di Figura A.3 (c) del Goodman si evince che il ciclo a fatica compreso tra i due punti in rosso (valori max e min del ciclo pulsante), sono compresi nell'area di torsione. Questo significa che l'albero è in grado di resistere a fatica ad alto numero di cicli. In Figura A.3 (d) sono riportati limiti a fatica valutati secondo diversi autori (Sodeberg, Goodman modificato, Gerber ed ASME). Considerando il limite più severo quello di Sodeberg, si può notare come il carico (punto rosso) sia compreso all'interno dell'area del limite. Pertanto, dalla seguente verifica a fatica semplificata si evince che l'albero dalla casa EMRAX (ESO), sollecitato dai carichi ipotizzati è in grado di resistere al fatica ad alto numero di cicli.

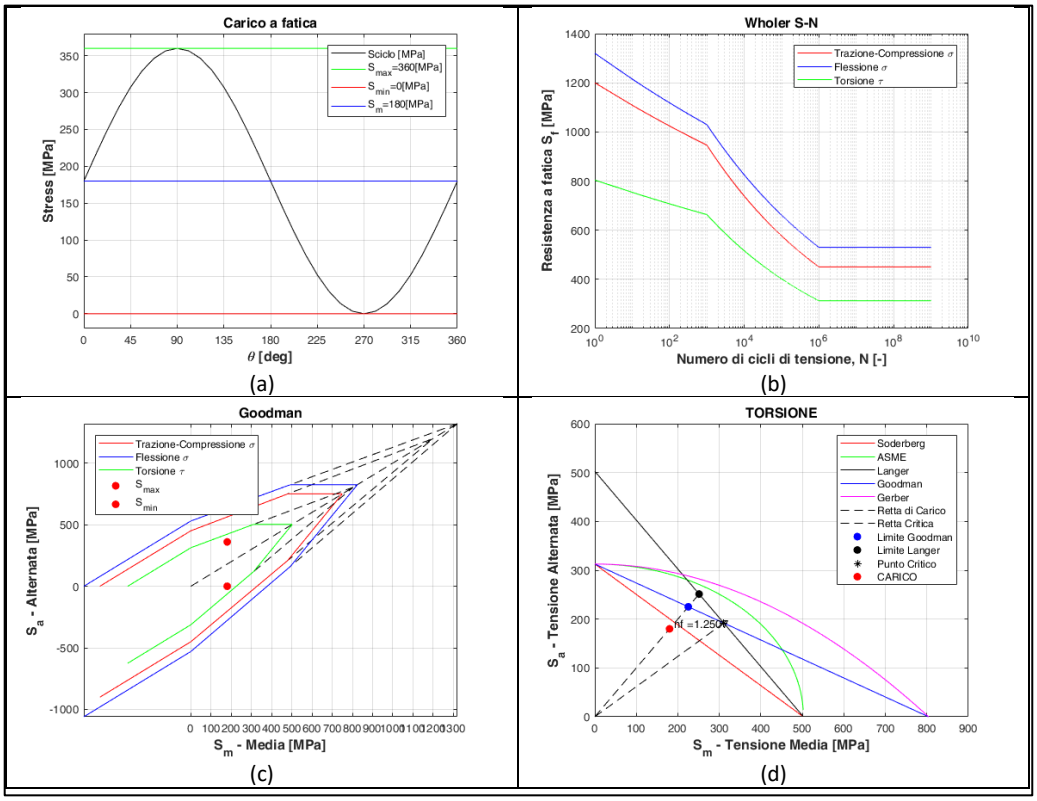

Figure A.3. Analisi della fatica: (a) Curva del carico pulsante; (b) Diagramma del Woolher; (c) Diagramma di Goodman; (d) High-Sodembreg, Gerber, Goodman Mod., ASME.

2.Dimensionamento Linguetta

Linguetta per accoppiamento meccanico tra cuscinetto unidirezionale (one-way bearing) e albero (1) di Figura A.1.

Geometria cava one-way bearing:

Diametro interno $d = 35\ mm$.

Secondo la norma DIN 6885/1 considerato il diametro dell'albero compreso tra 30<d<38 e con una larghezza di cava $b = 10\ mm$ P9/N9 risulta:

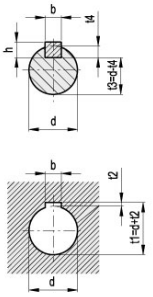

CAVE PER LINGUETTE DIN 6885/1

d	b P9/JS9 foro	b P9/N9 albero	h	t2	t4
da 6 fino a 8	2	2	2	1 +0.1	1.2 +0.1
oltre 8 fino a 10	3	3	3	1.4 +0.1	1.8 +0.1
oltre 10 fino a 12	4	4	4	1.8 +0.1	2.5 +0.1
oltre 12 fino a 17	5	5	5	2.3 +0.1	3 +0.1
oltre 17 fino a 22	6	6	6	2.8 +0.1	3.5 +0.1
oltre 22 fino a 30	8	8	7	3.3 +0.2	4 +0.2
oltre 30 fino a 38	10	10	8	3.3 +0.2	5 +0.2
oltre 38 fino a 44	12	12	8	3.3 +0.2	5 +0.2
oltre 44 fino a 50	14	14	9	3.8 +0.2	5.5 +0.2

CAVE PER LINGUETTE DIN 6885/2

d	b P9/JS9 foro	b P9/N9 albero	h	t2	t4
da 10 fino a 12	4	4	4	1.1 +0.1	3 +0.1
oltre 12 fino a 17	5	5	5	1.3 +0.1	3.8 +0.1
oltre 17 fino a 22	6	6	6	1.7 +0.1	4.4 +0.1
oltre 22 fino a 30	8	8	7	1.7 +0.2	5.4 +0.2
oltre 30 fino a 38	10	10	8	2.1 +0.2	6 +0.2
oltre 38 fino a 44	12	12	8	2.1 +0.2	6 +0.2
oltre 44 fino a 50	14	14	9	2.6 +0.2	6.5 +0.2

Posizionamento standard delle cave per linguetta

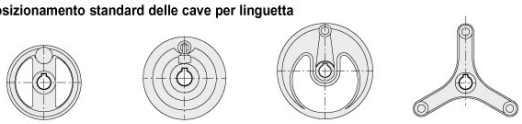

Figure A.4. Linguette a norma DIN 6885/1

Geometria della Cava su albero per linguetta DIN 6885/1:

Larghezza $b = 10\ mm$, profondità $t_4 = 5\ mm$, raggio $r = 0.25 - 0.40\ mm$, lunghezza $L = 50\ mm$.

Geometria Linguetta UNI 6604:

Larghezza $b = 10\ mm$, altezza $h = 8\ mm$, lunghezza $L = 50\ mm$.

Carico:

Coppia solo motore termico $M_t{}^{\mathrm{ICE}} = 330\ Nm$ si considera un coeff. di sicurezza $s = 1.2$

$$M_t{}^{\mathrm{ICE}} = 330\ \cdot 1.2 \approx 400\ Nm$$

Calcoliamo la forza tangente genera il momento torcente sul diametro interno della cava per la linguetta $d = 29mm$

$$F = \frac{M_t{}^{\mathrm{ICE}}}{\left(\frac{d}{2}\right)} = \frac{400}{\left(\frac{0.029}{2}\right)} = 27.6\ kN$$

Questa forza impone sui fianchi della linguetta una pressione p pari a circa

$$p = \frac{2F}{Lh} = \frac{2 \cdot 27.6 \cdot 10^3}{0.05 \cdot 0.008} = 135\ MPa$$

mentre all'interno della linguetta si genera una sollecitazione di taglio media pari a

$$\tau_{max} = \frac{3}{2}\left(\frac{F}{bL}\right) = \frac{3}{2}\left(\frac{27.6 \cdot 10^3}{0.010 \cdot 0.05}\right) = 82.8\ MPa$$

Per un corretto dimensionamento si possono seguire due strade:

a) Deve risultare che: $\tau_{max} \leq \tau_{amm}$ l'acciaio normalmente usato per la realizzazione delle linguette è il C45 $\sigma_{UTS} = 590\ MPa.\ \sigma_Y = 310\ MPa$ dove $\tau_{amm} = \frac{\sigma_Y}{\sqrt{3}} = 178\ MPa.$ condizione ampiamente verificata per il nostro caso.

b) Può essere imposto un limite sulla pressione di contatto $p_{max} \leq p_{amm}$ che per gli acciai $p_{amm} = 90 \div 250\ MPa$ anche in questo caso condizione risulta verificata.

3.Verifica cuscinetto unidirezionale

Il cuscinetto unidirezionale (one-way bearing) scelto per la trasmissione è il GL35 F2D2 Figura A.5.

Sono state effettuate due verifiche: una sulla coppia massima e l'altra sulla velocità di rotazione relativa tra l'anello interno e quello esterno.

Tipo Type Modele	d^{H7} mm	D_{h6} mm	L mm	L_2 mm	L_3 mm	s mm	D_4 mm	D_5 mm	o mm	z	n_{MAX} (min^{-1})1) Anello interno Inner race Bague intèrne	n_{MAX} (min^{-1})2) Anello esterno Outer race Bague extèrne	T_N Nm	Peso Weight Masse Kg
GL 12 F2-D2 (D3)	12	62	42	20	64	10	85	72	5,5	3	4000	5600	55	0,9
GL 15 F2-D2 (D3)	15	68	52	28	78	11	92	78	5,5	3	3700	5300	125	1,3
GL 20 F2-D2 (D3)	20	75	57	34	82	10,5	98	85	5,5	4	2700	4600	181	1,7
GL 25 F2-D2 (D3)	25	90	60	35	85	11	118	104	6,6	4	2200	3600	288	2,6
GL 30 F2-D2 (D3)	30	100	68	43	95	11,5	128	114	6,6	6	1800	3300	500	3,5
GL 35 F2-D2 (D3)	35	110	74	45	102	13,5	140	124	6,6	6	1500	3000	735	4,5
GL 40 F2-D2 (D3)	40	125	86	53	115	15,5	160	142	9	6	1200	2600	1040	6,9
GL 45 F2-D2 (D3)	45	130	86	53	115	15,5	165	146	9	8	1000	2400	1125	7,1
GL 50 F2-D2 (D3)	50	150	94	64	123	14	185	166	9	8	850	2200	2125	10,1
GL 55 F2-D2 (D3)	55	160	104	66	138	18	204	182	11	8	750	2000	2625	13,1
GL 60 F2-D2 (D3)	60	170	114	78	147	17	214	192	11	10	650	1900	3500	15,6
GL 70 F2-D2 (D3)	70	190	134	95	168	18,5	234	212	11	10	550	1700	5750	20,4
GL 80 F2-D2 (D3)	80	210	144	100	178	21	254	232	11	10	500	1600	8500	26,7
GL 90 F2-D2 (D3)	90	230	158	115	192	20,5	278	254	14	10	450	1500	14500	39,0
GL 100 F2-D2 (D3)	100	270	182	120	217	30	335	305	17	10	350	1250	20000	66,0
GL 120 F2-D2 (D3)	120	310	202	140	239	30	375	345	17	12	300	1100	25000	91,0
GL 130 F2-D2 (D3)	130	310	212	152	250	29	375	345	17	12	250	1000	31250	91,0
GL 150 F2-D2 (D3)	150	400	246	180	286	32	485	445	22	12	200	800	70000	200,0

Figura A.5. Dati cuscinetto unidirezionale.

- La coppia massima ammissibile $T_N = 735\ Nm$ è superiore alla coppia trasmessa dal motore termico $M_t{}^{ICE} = 330\ Nm$. Condizione verificata;
- La verifica della velocità limite di rotazione compete solo nel caso di *full-electric* ovvero quando il motore termico è spento. In questo caso l'anello interno è fermo e l'anello esterno è libero di muoversi in quanto viene trascinato dal motore elettrico. La velocità limite ammissibile è pari a $n_{max} = 3000\ rpm$ che risulta appena superiore alla massima velocità di rotazione dell'elica fissata a $n_{elica} = 2750\ rpm$. Anche questa condizione è verificata.